

Transparent structured conductive coating for applications in smart windows.

Présentée le 31 mars 2023

Faculté de l'environnement naturel, architectural et construit
Laboratoire d'énergie solaire et physique du bâtiment
Programme doctoral en énergie

pour l'obtention du grade de Docteur ès Sciences

par

Jérémy Jacques Antonin FLEURY

Acceptée sur proposition du jury

Dr J. Van Herle, président du jury
Prof. J.-L. Scartezzini, Dr A. Schueler, directeurs de thèse
Dr J. Heier, rapporteur
Prof. E. Panda, rapporteuse
Prof. P. Hoffmann, rapporteur

Dans la vie, rien n'est à craindre,
tout est à comprendre.
— Marie Curie

ACKNOWLEDGEMENTS

The past four years have been a time of extensive learning and growth for me both professionally and personally. I would not have been able to complete this work without the support and guidance of my advisors, colleagues, friends and family.

First, I would like to express my deepest gratitude to Dr. Andreas Schüler, for the continuous support of my PhD study and related research, for his patience, motivation, and immense knowledge. His guidance helped me in all the time of research and writing of this thesis. As well, I would like to express my sincere thanks Prof. Jean-Louis Scartezzini, for his consistent support, and encouragement throughout my PhD.

Furthermore, I would like to thank Prof. E. Panda, Prof. P. Hoffmann, Dr. J. Heier, and Dr. J. Van Herle for accepting to be member of the Jury of my doctoral exam.

I thank Luc Burnier for his help in the ESCA characterization and measurement campaign at NEST. Matteo Lanini for his support and great knowledge regarding mobile communication and microwave simulations. Léo Ferrand for his support and great work on FDTD simulations and Tina Mitterramskogler for the fabrication of samples by nanoimprint lithography. I would like to gratefully acknowledge the continued financial support of the Swiss Federal Office of Energy over the years. I especially thank Nadège Vetterli and Andreas Eckmanns for their support.

I thank my colleagues at LESO-PB, all the "lézards": my office and lab-mates with whom I worked over the years, especially, Anna, Olivia, Alina, Marta, Chiara, Maxime and Krishna. It has been a true pleasure working with them. I also thank Shivam for his friendship and guidance during my exchange to IIT Gandhinagar, India and the team at CMi for their great help with clean-room facilities and nano-fabrications.

A special thank you goes to my mountains buddies, who gave me tremendous support and helped me empty my mind during the adventurous weekends, especially Alex (mountain & proof-reading), Loïc, Romain, Nicolas, Simon and all the members of the Club Montagne comité.

Last but not the least, I would like to especially thank Julie for her love, support, and constant encouragement during all these years. ♡

Lausanne, February 22, 2023

J. E.

ABSTRACT

Solar radiation reaching the surface of the earth for a period of one hour contains more energy than that consumed by mankind over an entire year. Some of this solar energy is already collected by photovoltaic cells to cover the electricity needs of buildings but the most dominant part of the total energy consumption is space heating. This thesis explores ways of efficiently using solar radiation that penetrates buildings' windows to intelligently manage indoor temperatures and reduce the need for indoor heating.

Energy-efficient windows are already being used to increase the thermal insulation of a façade. Such insulating windows contain an ultra-thin, multilayered, transparent silver coating that acts as an infrared mirror which significantly reduces thermal losses that occur through radiation from inside the building. These so-called low-emissivity coatings revolutionized the field of building insulation since the early '80s, but also come with some drawbacks, such as (i) decreased solar heat gain coefficient which reduces the potential for energy savings during winter; (ii) lack of adjustability in reflectivity/heat retention during different seasons; and (iii) the metallic nature of the coating negatively affects signal transmission of modern telecommunication.

The purpose of this work is to explore what properties can be achieved by laterally structuring a coating or multilayer and investigate how these novel properties can be exploited in various applications for window glazing in buildings. It is shown that structuring the coating into a patch array acts as a high-pass filter and makes a window more transparent to microwaves. In contrast, a wire mesh behaves as a low-pass filter, creating a glazing that selectively lets in solar radiation. Finally, the ability of modulating the transparency of window glazing according to seasonal variations in solar radiation is demonstrated using large-band electrochromic windows that can adapt the color of the glazing depending on the situation.

These technologies are expected to contribute to the development of optimized electrochromic window that modulates solar heat gains and daylight inside buildings, enabling also to reduce indoor space heating energy needs.

RÉSUMÉ

Le rayonnement solaire qui atteint la surface de la terre durant une heure fournit plus d'énergie que toute l'énergie consommée par l'humanité pendant une année entière. Une partie de cette énergie solaire est déjà collectée par des cellules photovoltaïques pour couvrir les besoins en électricité des bâtiments mais la partie la plus importante de la consommation totale d'énergie est le chauffage des locaux. Cette thèse explore les moyens d'utiliser efficacement le rayonnement solaire passant par les fenêtres des bâtiments pour gérer intelligemment les températures intérieures et réduire le besoin de chauffage.

De nos jours, les fenêtres modernes sont utilisées pour augmenter l'isolation thermique d'une façade. Ces fenêtres isolantes comprennent un revêtement transparent multicouche composé de plusieurs films d'argent ultrafins agissant comme un miroir infrarouge qui réduit considérablement les pertes thermiques par rayonnement provenant de l'intérieur du bâtiment. Ces revêtements dits à faible émissivité ont révolutionné le domaine de l'isolation des bâtiments depuis le début des années 80, mais présentent également certains inconvénients, tels que (i) ils réduisent le gain de chaleur solaire, ce qui réduit le potentiel d'économies d'énergie en hiver; (ii) le manque d'ajustement de la réflectivité de chaleur au cours des différentes saisons; et (iii) la nature métallique du revêtement qui affecte négativement la transmission des signaux des télécommunications modernes.

L'objectif de ce travail est d'explorer les propriétés qui peuvent être obtenues en structurant latéralement un revêtement ou une multicouche et d'étudier comment ces nouvelles propriétés peuvent être exploitées dans diverses applications pour les vitrages des bâtiments. Il est démontré qu'en structurant le revêtement en un réseau de patches, il agit comme un filtre passe-haut et rend une fenêtre plus transparente aux micro-ondes. À l'inverse, un treillis métallique se comporte comme un filtre passe-bas, créant un vitrage qui laisse sélectivement entrer le rayonnement solaire. Enfin, la capacité de moduler la transparence des vitrages en fonction des variations saisonnières du rayonnement solaire est démontrée à l'aide de fenêtres électrochromiques à large bande qui peuvent adapter la couleur du vitrage en fonction de la situation.

Ces technologies devraient contribuer au développement de fenêtres électrochromes optimisées qui modulent les gains de chaleur solaire et la lumière du jour à l'intérieur des bâtiments, permettant ainsi de réduire les besoins en énergie pour le chauffage des espaces intérieurs.

CONTENTS

Acknowledgements	i
Abstract	iii
List of Figures	xi
List of Tables	xix
Nomenclature	xxi
1 Introduction	1
1.1 Motivation	1
1.2 Mobile communication through energy-efficient windows	2
1.3 Low-e coating with enhanced selectivity	4
1.4 Smart windows with adaptable selectivity	7
1.5 Research aims and objectives	11
1.6 Structure of the thesis	11
I Microwave transparent windows	13
2 Wide band-pass Frequency Selective Surfaces	15
2.1 Introduction	16
2.2 Methodology	18
2.2.1 Equivalent circuit theory	18
2.2.2 Simulation	19
2.2.3 Manufacture of the windows	19
2.2.4 Experimental setup	20
2.3 Results	21
2.3.1 Computer simulation	21
2.3.2 Experiments	24
2.3.3 Comparison between simulated and experimental data	24
2.4 Discussion	28
2.4.1 Group delay	28
2.4.2 Resonance cavities	29

Contents

2.4.3	Angular dependency	31
2.5	Conclusion	31
3	Combining thermal insulation and mobile communication in buildings	33
3.1	Introduction	33
3.2	Methodology	34
3.3	Results & Discussion	35
3.4	Conclusion	38
II	Highly selective low-e coating	39
4	Theoretical understanding of metal meshes	41
4.1	Introduction	41
4.2	Materials and Methods	44
4.2.1	Numerical simulation	44
4.2.2	Nano-imprint fabrication	46
4.3	Results & Discussion	47
4.3.1	Validation numerical model	47
4.3.2	Optimization solar radiation vs emissivity	48
4.4	Conclusion	54
III	EC windows with adaptable selectivity	55
5	Electrochromic device with hierarchical metal mesh electrodes	57
5.1	Introduction	57
5.2	Methodology	59
5.2.1	Manufacturing of transparent mesh electrodes	59
5.2.2	Electrical and optical characterization	61
5.2.3	Preparation electrochromic layers	61
5.2.4	Electrochemical experiments	62
5.3	Results & Discussion	64
5.3.1	Transparent conductive film	64
5.3.2	Cathode & anode characterization	69
5.3.3	Electrochromic device	74
5.4	Conclusion	77
6	Electronic properties and ion migration of WO₃:Mo thin films	79
6.1	Introduction	79
6.2	Methodology	80
6.2.1	Film Preparation	80
6.2.2	X-ray and Ultraviolet Photoelectron Spectroscopy (XPS, UPS)	81
6.2.3	Optical Characterization	82

6.2.4	Determination of optical band gap	82
6.3	Results & Discussion	82
6.3.1	XPS	82
6.3.2	UPS and optical spectrometry	86
6.3.3	Lithiation bilayers	90
6.4	Conclusion	91
7	Conclusion	93
7.1	Outlook	95
	Bibliography	97
	Curriculum Vitae	107

LIST OF FIGURES

1.1	Overall energy consumption in Switzerland in 2021. ^[1]	2
1.2	(a) Schematic representation of the strong signal attenuation in buildings with standard energy efficient windows; (b) Drawing showing the ablation principle of the insulating transparent low-e coating; (c) Schematic representation of a building with laser-treated energy-efficient windows.	3
1.3	Two-dimensional sketch of non-resonant (a) capacitive and (b) inductive FSS filters with equivalent circuit and spectral properties ^[10]	4
1.4	Transmission and reflexion spectra of an ideal solar gain coating. The solar irradiance is transmitted to the building and the radiation from a blackbody at room temperature is reflected to keep the heat inside the room. Both, the global solar irradiance at 1.5 AM and the blackbody radiation are normalized between 0 and 1 and expressed in arbitrary unit (a.u.) as reference.	5
1.5	Wavelength selectivity achieved by a metal mesh structure. (a) Short-wavelength radiation are transmitted and (b) long-wavelength radiation are reflected. Image taken from M. Meier's thesis ^[15]	6
1.6	FDTD simulations of a plane wave traveling through metallic pillars with a periodicity $P = 1'875$ nm and a width $w = 1'000$ nm. The colors indicate the E-field (in V/m) distribution of a perpendicular (z-direction) polarized electromagnetic wave at a wavelength of (a) $0.55 \mu\text{m}$ and (b) $15 \mu\text{m}$. (c) presents a top view of the design with xyz-axis.	7
1.7	Performance requirements for various climates and performance of thermochromic, electrochromic, suspended particles (SP), and gasochromic (GC) windows. Figure taken from Daqiqeh Rezaei's journal article ^[17]	8
1.8	Schematic illustration of an electrochromic window.	9
1.9	ITO replacement comparison chart, metal mesh is a promising candidate for high conductivity and low cost transparent conductive films. Figure taken from ITO-Replacement Report 2016 ^[24]	10
2.1	(a) IGU model used in this study, D describes the cell periodicity of the FSS and w the engraving width. (b) Microscope image of the laser structure coating with a engraving width of $w = 25 \pm 5 \mu\text{m}$	17
2.2	Possible equivalent circuits for the IGU. (a) no coating, (b) full coating, (c) FSS surface.	18

List of Figures

2.3	Experimental setup for assessing the properties of the IGUs.	20
2.4	Simulation of the transmission loss (S21) for varying engraving width w and fixed periodicity $D = 2\text{mm}$. Clear transmission bands due to the resonance cavity created by the air gap can be seen at 12, 24.5 and 37 GHz. Two secondary peaks around 15 and 30 GHz are due most likely to the finite thickness of the glass panes.	21
2.5	Simulation presenting the transmission loss (S21) for varying cell periodicity D and fixed engraving width $w = 35\ \mu\text{m}$. For narrower D , the transmission increases which leads to broader band-pass.	22
2.6	Simulation presenting the reflection respond (S11) for varying cell periodicity D and fixed engraving width $w = 35\ \mu\text{m}$. Very sharp reflection minima are obtained at well defined frequencies.	23
2.7	Simulation showing the transmission loss (S21) for a constant D/w factor at 95.06 %. For smaller D and w factors, the transmission is improved.	23
2.8	Simulation presenting the transmission phase variation at different cell periodicity.	24
2.9	Experimental measurements for IGU with structured low-e coating and varying cell periodicity D . The solid lines show the smoothed measurements, while the dashed lines represent the envelope of the raw data. The resonance peak for each IGU moves between 35.5 and 37.5 GHz due to a small different in air gap distances. Generally, the transmission increases for narrower cell periodicity.	25
2.10	Comparison between the measured and simulated signal attenuation. The solid lines show the smoothed measurements, while the dashed lines represent the envelope of the raw data.	26
2.11	Comparison between the measured and simulated signal attenuation for an IGU with a full coating. The fitted air gap parameter is 12.4 mm. The experimental transmission shows a large envelope due to the strong attenuation of the IGU.	27
2.12	Simulated group delay for varying cell periodicity D . The group delay remains below 350 ps for all samples at frequencies from 1 to 40 GHz.	28
2.13	Simulation of the resonance frequencies due to glass cavities (without coating) where the air gap is varied. Specific frequencies at 14.86 and 29.81 GHz show excellent transmission for every air gap distance.	29
2.14	Simulated transmission loss at 14.86 and 29.81 GHz from normal (0°) to near-grazing ($\sim 90^\circ$) angles of incidence. The results are plotted for TM (a) and TE (b) polarization. The straight lines represent an IGU without any coating (only float glass) and the dashed lines an IGU with a 1 mm cell periodicity FSS.	30
3.1	(a) Architectural plan of the south-west façade and (b) Top view of the SolAce unit where each dot represents one measurement. In both Figures, the two windows that were replaced with microwaves transparent windows are shown in blue.	34

3.2	(a) Schematic design of a triple glazing window installed in the SolAce unit. The window consists of one 4 mm standard soda-lime (float) pane combined with two thicker (5 and 6 mm) ESG (tempered glass) panes with two air-gaps of 16 mm. Two structured low-e insulating coatings can be found on surfaces 3 and 5 (1 being the outer and 6 the inner surface). (b) Drawing showing the ablation principle of the insulating transparent coating. (c) Microscope image of the low-e coating after the ablation process. The width of each line is approximately 25 μm	36
3.3	Simulation of EM waves propagating perpendicularly through a triple glazing unit based on the configuration shown in Figure 3.1a at frequency ranging from 0.5 to 5 GHz. The behavior of laser-treated window is comparable to an IGU without low-e coating, while the low-e coated glazing strongly attenuates the signal.	37
3.4	Contour plot presenting the change in RSRP values with a precision of ± 1.5 dB between the inside and outside of the unit where (a) shows the first configuration with standard IGU (triple glazing with two low-e coatings) and (b) two hinged windows on the bottom right were replaced with laser-treated glazing. This modification resulted in a highly directional increase of the signal strength. . .	37
4.1	Illustration of Maxwell's equation in differential form: (1) Gauss' Law, (2) Gauss' Magnetism Law, (3) Faraday's Law and (4) Ampere's Law.	42
4.2	Visualization of the Yee cell and leapfrog time-stepping for (a) TM_z and (b) TE_z -mode. An unit cell of Δx by Δy is called a Yee cell. The E_z components are calculated at a distance Δx and Δy , the H components are located in the middle of the cell (in between the E components). Illustrations are taken from M. Meier thesis ^[15]	42
4.3	(a) Schematic cross-section and (b) top view of a structured coating with w being the width of one line, t the thickness and p the periodicity of one unit cell. . . .	44
4.4	Layout Lumerical Software where the large blue rectangle represents a glass substrate of $4 \times 4 \mu\text{m}$ covered by a thin metal coating. The orange box describes the FDTD simulation region where the purple arrow is the incoming EM wave. To extend the model to an infinite array, periodic boundary conditions are used on the side of the model.	45
4.5	Schematics of nanoimprint fabrication process. Figure taken from Mitteramskogler et al. journal paper ^[63]	46
4.6	SEM images showing the micro-holes array achieved by nanoimprint lithography. (a) top-down view of the structures and (b) 10.5° tilted of a cross-section. The dashed rectangle describes the unit cell chosen for the FDTD simulation, it has a size of $3 \times 5.2 \mu\text{m}$	46
4.7	Simulated transmission spectra of Au nano-holes array as a function of nano-hole diameter. Where (a) describes the results from this work and (b) simulations based on article by Q. Tong et al. ^[64] . The periodicity of the structure is 1000 nm.	47

List of Figures

4.8	Transmittance spectra of measured and simulated 32 nm silver thin film coating compared to a micro-hole array structured film. The simulated model fits closely the measured data in the visible range and has a slightly higher transmittance in the NIR.	48
4.9	Transmittance spectra of a structured PEC mesh with a square geometry and a constant periodicity $p = 2000$ nm. (a) the linewidth w is varied from 100 to 1500 nm ($t = 35$ nm) and (b) the thickness t is swept between 10 and 500 nm ($w = 500$ nm).	49
4.10	Transmittance spectra of a structured PEC mesh with a ratio $p/w = 2.5$ kept constant and a thickness of 35 nm. p is varied and w is adapted accordingly to keep the fixed ratio. The transmission peak moves according to the periodicity.	50
4.11	Transmittance, reflectance and absorptance spectra of a 10 nm Ag coating.	51
4.12	The skin depth of bulk Ag for varying wavelengths of incident light.	51
4.13	Transmittance spectra of two Ag coatings with thicknesses of 10 and 50 nm and a nanomesh structured Ag film with $p = 350$ nm, $w = 50$ nm and $t = 50$ nm. The structured coating shows high transmittance in the visible range and decreases significantly in the MIR region. Both, the global solar irradiance at 1.5 AM and the blackbody radiation are normalized between 0 and 1 and expressed in arbitrary unit (a.u.) as reference.	52
4.14	(a,b) Top-view and (c,d) cross-section of the electric field distribution in V/m through the mesh at a wavelength of 363 and 540 nm. The edges of the Ag structure are drawn in white lines. The white crosses indicates the location of the monitor compared to each other.	53
5.1	(a) Schematic cross-section and (b) top view of a metal mesh with w being the width of each deposited line, t the thickness and p the periodicity of one unit cell.	59
5.2	Step-by-step outline of the process to produce transparent mesh electrodes using UV-photolithography. The substrate (a) , consisting of soda-lime glass, and is spin-coated with a negative photoresist (b) . The sample is locally exposed to a UV-laser to harden the photoresist. This is followed by the removal of non-exposed resist (c) . A thin metal film is then evaporated over the sample (d) and, finally, the remaining photoresist is lifted-off in a chemical bath to produce the mesh structure (e)	60
5.3	Electrochemical setup designed for optical characterization of EC half devices. The experiment consists of three electrodes: a platinum mesh counter electrode (CE), a non-aqueous Ag/Ag ⁺ reference electrode (RE) and a glass coated with a transparent conductive film and WO ₃ or Ta:NiO as a working electrode (WE). The electrolyte is kept under an inert environment during the characterization through a constant flow of nitrogen within the cell.	62
5.4	Electrochemical setup designed for optical characterization of full devices. The cathode and the anode are glue together with a pre-cut, squared, 0.25 mm thick double sided tape.	63

5.5	(a) Microscope and (b, c) SEM images of a metal mesh with a periodicity (p) of 100 μm , a line width (w) of 2 μm and a thickness (t) of 300 nm	64
5.6	Total transmittance spectra comparing various transparent conductive films. All metal meshes have the same aperture parameter of $\tau = 0.98$ and are grouped under the blue line. The solar radiation on the ground is plotted in arbitrary units as reference. The metal meshes produce a spectrally flat transmittance in the full spectral range of solar radiation.	65
5.8	Cross-section SEM images of (a,c) WO_3 and (b) Ta:NiO on silicon displaying a thickness of, respectively, 200 and 175 nm. (c) Pt-2-100 metal mesh with WO_3 layer focusing on the metal/semiconductor interface.	67
5.7	Haze factor compared for various sizes of the metal mesh in the visible spectral range: the smaller the structure, the more it diffracts light and thus haze is produced.	67
5.9	Electrochromic properties of the WO_3 cathode in Li-PC measured at -1.25/+0.25 V (vs Ag/Ag ⁺) comparing ITO and the metal mesh: (a) Transmittance spectra in colored and bleached taken from CA measurements. (b) Cyclic voltammograms at a scan rate of 10 mV/s where the vertical arrows give the open circuit voltage at which the scan started/ended. (c) Chronoamperometry curves for 8 cycles of 30 s and (d) its resulting in situ visible transmittance. Pt-2-100 achieves outstanding transmittance modulation in the NIR spectrum.	68
5.10	Electrochromic properties of the Ta:NiO anode in Li-PC measured at -1.5/+1 V (vs Ag/Ag ⁺) comparing ITO and the metal mesh: (a) Transmittance spectra in colored and bleached taken from CA measurements. (b) Cyclic voltammograms at a scan rate of 10 mV/s at which the vertical arrows give the open circuit voltage where the scan started/ended. (c) Chronoamperometry curves for 8 cycles of 30 s and (d) the resulting in situ visible transmittance.	71
5.11	UV-Vis-NIR transmittance spectra of the full-device taken from the CA experiment comparing the metal mesh and ITO10 in the bleached and colored states. The modulation in solar transmittance is significantly larger for Pt-2-100 (36.1 %) compared to ITO (24.3 %).	73
5.12	Electrochromic properties of full devices in Li-PC measured at -2.5/+4 V for the metal mesh, (a,c), and at -2.5/+2.5 V for ITO, (b,d): (a,b) Cyclic voltammograms at a scan rate of 10, 20, 50 and 100 mV/s where the vertical arrows give the open circuit voltage at which the scan started/ended. (c) Chronoamperometry curves for 5 cycles and (d) the resulting in situ visible and solar transmittance.	75
5.13	Photos of the Pt-2-100 metal mesh ECD during coloration/bleaching process. First a -2.5 V potential is applied for 30 s leading the coloration. Then it is switched to 4 V for the bleaching phase. The black circle behind the device is the diaphragm opening to the spectrometer.	76
5.14	CIE 1931 color diagram with the x, y color coordinates of full devices in colored and bleached states. Pt-2-100 shows a slightly more pronounced blue tint in the colored state.	76

List of Figures

- 6.1 XPS Core-level spectra of W 4f doublet. The curves compare the different nominal concentrations of lithium ions over tungsten content ($c_{Li/W}$). For higher concentration, the peaks are shifting to higher BE and the doublet is broadened, the latter indicating the formation of W^{5+} oxidation states. 83
- 6.2 XPS Core-level spectra of Mo 3d doublet. The shape of the spectrum at $c_{Li/W} = 0.07$ has changed considerably, suggesting a higher concentration of Mo^{5+} oxidation states. This phenomenon is further accentuated with increasing lithium concentration and a new peak appears at lower BE. 83
- 6.3 XPS Core-level spectra of O 1s peak. A shift towards higher BE can be seen as the lithium concentration increases. 84
- 6.4 Deconvolution of (a) W 4f and (b) Mo 3d doublet at different nominal lithium concentration $c_{Li/W} = 0, 0.07$ and 0.38 . Experimental data are displayed in blue dots, contributions of W 4f and Mo 3d peaks in dark and W 5p in light grey. Both non-lithiated spectra ($c_{Li/W} = 0$) reveal a well-resolved doublet, attributed to the 6+ oxidation states. As the lithium concentration increases, the core levels change in line shape caused by the occurrence of 5+ oxidation states. 85
- 6.5 Relative number of tungsten and molybdenum atoms in 5+ state (W^{5+}/W_{tot} , Mo^{5+}/Mo_{tot}) vs. the bulk nominal concentration of lithium ions. The ratio of W^{5+} oxidation states increases slowly at $c_{Li/W} = 0.07$ and more significantly at the end of the lithiation process. In contrast, the number of Mo^{5+} oxidation states increase rapidly at the beginning of the lithiation and slower towards the end. 86
- 6.6 UPS photoemission spectra of $Mo_{0.1}W_{0.9}O_3$ with varying concentration of lithium ions $c_{Li/W}$ switching from as-deposited transparent to colored state with (a) being the secondary-electron cut-off region, (b) the entire view of the valence band spectra and (c) the near Fermi level region. 87
- 6.7 Plot of the work function at different nominal Li concentration. The work function declines rapidly with few intercalated lithium ions and then decreases linearly at higher ions content. 87
- 6.8 Schematic diagram of the energy levels in the valence and conduction band with increasing ion intercalation. The red and blue stripes describe partially localized states near the valence band and conduction band edge. The values in orange give the energy of VBE and in black the optical band gap. The dotted arrows represent the work function (Φ). The Fermi level (E_F) was set to a fix value of 0 eV. 88
- 6.9 Energy level schematic of lithiated $Mo_{0.1}W_{0.9}O_3$ with O 2p, Mo 4d and W 5d bands. First the Mo^{5+} gap states are preferentially filled with the electrons from the lithium ions. In a second phase, the W^{5+} gap states are filled. 89
- 6.10 Cross-section schematic of the four combinations chosen to study the propagation of lithium in the material. The two configurations on the upper half are used as reference and the two at the bottom are the investigated bilayers. 90

6.11 Spectral transmittance of the four investigated samples in bleached and colored states, where the right side shows a magnification of the curves in colored state. Bleached samples show oscillations due to interference fringes. Upon lithiation, all samples show similar transmittance with the exception of pure WO ₃ which strongly transmits in the blue and absorbs in the NIR range. Bilayer 2 (with pure WO ₃ on top) shows a VIS absorption in the blue range, which is characteristic to the WO ₃ :Mo layer.	91
7.1 2D cross-section combining multiple hierarchical structured layers for multi-functional electrochromic application.	95

LIST OF TABLES

1.1	Optical properties of single, double and triple glazing taken from AGC online configurator ^[11] . For each glazing the panes consist of a clear-white 4 mm thick float glass and the air gap distance is always 14 mm filled with air or argon (Ar). It is compared to the insulated glazing unite with one (or two for triple glazing) iplus 1.0 low-e coating.	5
1.2	Advantages and disadvantages of ITO as a transparent conductive oxide	9
2.1	Literature review about bandpass FSS on insulating glass unit.	16
2.2	Range of fit parameters	25
4.1	Visible, solar transmittance and emissivity. The value for single glazing are taken from AGC ^[11]	53
5.1	Literature review of transparent conductive films and their physical properties.	59
5.2	Deposition parameters plasma sputtering: the working pressure in the range of 10^{-2} mbar allowed for the growth of a nanoporous coating which is beneficial for ions permeability in ECDs.	61
5.3	Optical and electrical properties of transparent conductive films. All metal meshes have an identical aperture parameter τ of 0.98.	65
5.4	Electrochromic properties for the cathode, anode and fully functional ECD. t_c and t_b give the switching time needed to reach 95 % and D_c^+ , D_b^+ the diffusion coefficient for, respectively, the coloration and bleaching state.	73
6.1	Deposition parameters. The working pressure in the range of 10^{-2} mbar allowed for the growth of a nanoporous coating which is beneficial for ions permeability in EC devices.	81

NOMENCLATURE

Acronyms

CA	Chronoamperometry	SNR	Signal to noise ratio
CBE	Conduction band edge	TBAP	Tetrabutyl ammonium perchlorate
CNC	Computer numerical control	TCF	Transparent conductive film
CV	Cyclic voltammetry	TCO	Transparent conductive oxide
DC	Direct-current	TE	Transverse electric
DCS	Digital cellular system	TF	Telecommunication frequencies
EC	Electrochromic	TM	Transverse magnetic
ECD	Electrochromic device	TPS	Thin-plate spline
EM	Electromagnetic	UPS	Ultraviolet photoelectron spectroscopy
EMA	Effective medium approximation	VBE	Valence band edge
EMPA	Swiss Federal Laboratories for Materials Science and Technology	VIS	Visible
FDD	frequency-division duplexing	XPS	X-rays photoelectron spectroscopy
FDTD	Finite-Difference Time-Domain	Variables	
FSS	Frequency selective surface	ϵ	Emissivity coefficient [-]
FWHM	Full width at half-maximum	ϕ_H	Haacke figure of merit [$10^{-3}\Omega^{-1}$]
HFSS	High-frequency structure simulator	Φ	Work function [eV]
IGU	Insulated glass unit	τ_e	Solar transmittance [%]
IR	Infrared	τ_v	Visible transmittance [%]
ITO	Indium tin oxide	D^+	Diffusion coefficient [cm^2/s]
Low-e	Low emissivity	i	Current [A]
LTE	Long term evolution	p	Porosity [%]
MIR	Mid-Infrared	Q	Inserted charge [C]
NHE	Normal hydrogen electrode	R_s	Sheet resistance [Ω/\square]
NIR	Near-infrared	x	Intercalation level [%]
NTO	Niobium-doped TiO	BE	Binding energy [eV]
OFDM	Orthogonal frequency-division multiplex- ing	CE	Coloration efficiency [cm^2/C]
PEC	Perfect electric conductor	E_F	Fermi level [eV]
RSF	Relative sensitivity factors	E_g	Optical band gap [eV]
SEM	Scanning electron microscopy	OD	Optical density [-]
		RSRP	Reference Signal Received Power [dB]
		SHGC	Solar Heat Gain Coefficient [%]
		U-value	Thermal transmittance [$\text{W}/(\text{m}^2\text{K})$]

1 INTRODUCTION

This thesis is based on a compilation of articles published (or submitted) in scientific refereed journals and is structured as follow:

- an introduction that puts the project into context, giving the motivation and global objectives of the research
- each chapter is presented with a short description of its purpose within the project, a literature review, a complete list of authors, a detailed description of the doctoral candidate's contribution and a full bibliographic reference.
- a general conclusion chapter, summarizing the main contributions of the thesis
- a section presenting possibilities for future development of the work

1.1 Motivation

In 2021, space heating was the dominant part of Swiss final energy consumption (256.4 PJ), corresponding to a share of 33.8 % of the total energy consumption (758.6 PJ) (see Fig. 1.1). 166.2 PJ (22 %) are consumed for space heating in private households. In comparison, the energy for lighting and air conditioning, ventilation and cooling in the households contributed to, respectively, 4.6 PJ (0.6 %) and 4.5 PJ (0.6 %). The heating energy is issued at 34.9 % from fuel oil and 27.4 % from natural gas which is directly related to our dependency on fossil fuels and produces important emission of greenhouse gases.

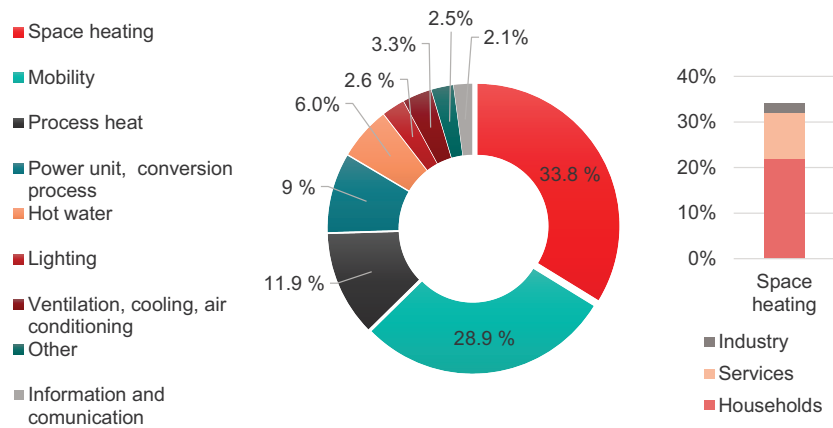


Figure 1.1: Overall energy consumption in Switzerland in 2021. ^[1]

Nowadays, the use of insulating glazing belongs to the state of the art in modern buildings as well as in building retrofit. Transparent low-emissivity (low-e) metallic coatings are used in combination with argon filling, decreasing the energy loss through the glazing and improving the overall energy balance compared to standard glazing (e.g. non e-coated). Low-e coatings are transparent in the visible (VIS) range and act as mirrors in the mid-infrared (MIR) which reduces the energy loss through thermal radiation. However, these coatings lead to a few disadvantages:

- Because of the metallic nature of the coating, it attenuates drastically (around 30 dB) the signal transmission of modern telecommunication frequencies (TF) from 0.3 up to 30 GHz.
- It decreases the solar heat gain coefficient (SHGC, also known as g-value) which hinders the potential of energy saving during winter ^[2]
- The coating has a fixed transmittance value and is not adjustable during the course of different seasons (warm/cold climates)

These shortcomings are explained more in details in the following sections and practical solutions such as micro-nanostructured low-e coatings and metal mesh electrode are presented throughout the thesis.

1.2 Mobile communication through energy-efficient windows

The demand for mobile communication between persons and more recently between objects (Internet of Things) is continuously and rapidly increasing. As mentioned above, modern

1.2 Mobile communication through energy-efficient windows

energy-efficient windows (double or triple glazing) have become a standard in the building sector. The combination of modern glazing and the large use of reinforced concrete leads to buildings which act as a Faraday cage and are signal-proof to microwave transmission^[3-7]. This signal attenuation is due to the conductive silver or tin oxide layer found in the (low-e) coatings which reduces the reference signal received power (RSRP) by up to 1000 times (30 dB). As depicted in Figure 1.2a, this leads to lower throughput and poor internet / phone call signal. One approach to improve the radio signal transmission consists of structuring the metallic coating to create a wide band-pass Frequency Selective Surface (FSS). As shown in Figure 1.2b, a laser ablation method is used to scribe a line pattern on the coating which greatly increases the signal strength inside the building (see Fig. 1.2c). This innovative approach was first implemented for application in trains where the envelope comprised of metal which accentuates even more the effect of the Faraday cage^[8,9]. In Part I, this method is further investigated with the fabrication of new glazing with various line pattern dimensions and post-treatment processing (laser-process on double glazing windows after assembly). The signal attenuation is then measured at low and high (5G) microwave frequency range and the propagation of microwaves in buildings is quantified.

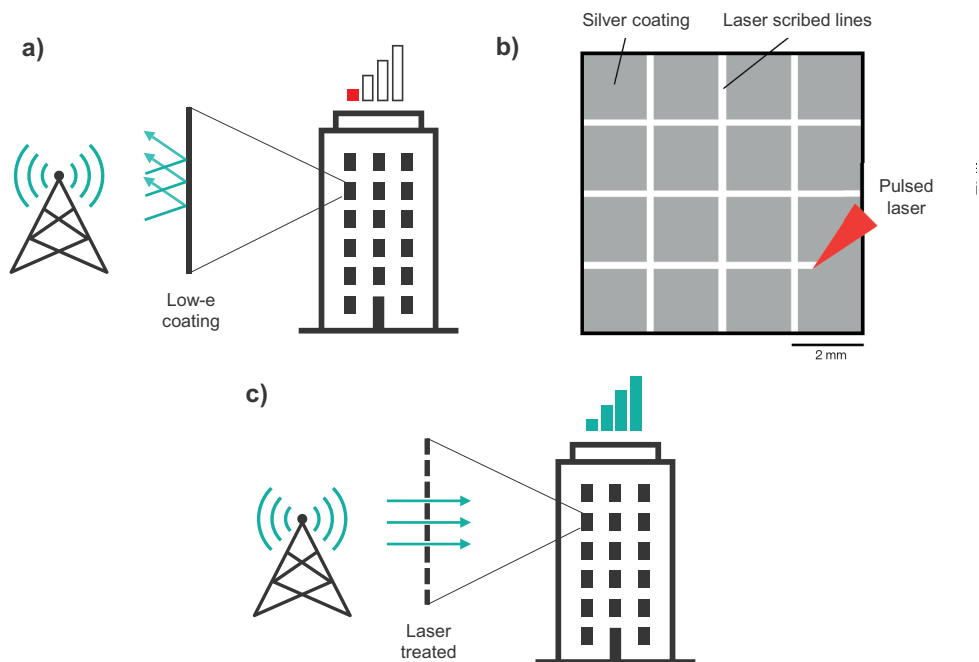


Figure 1.2: (a) Schematic representation of the strong signal attenuation in buildings with standard energy efficient windows; (b) Drawing showing the ablation principle of the insulating transparent low-e coating; (c) Schematic representation of a building with laser-treated energy-efficient windows.

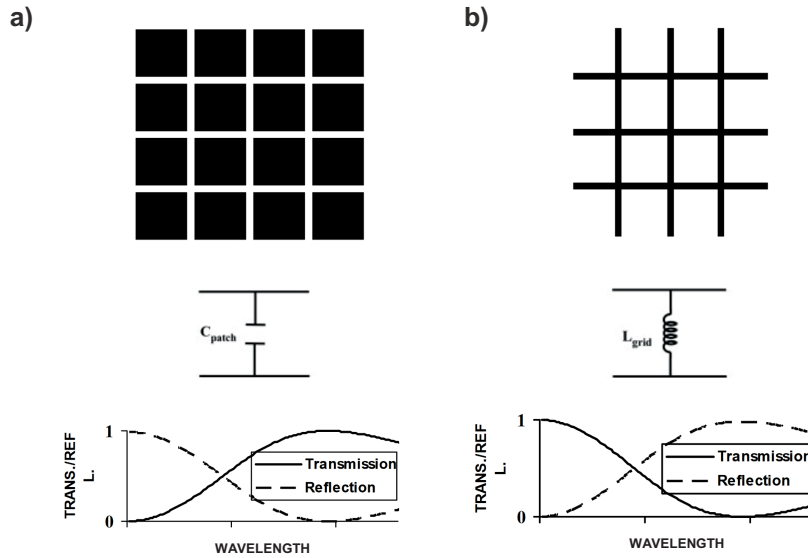


Figure 1.3: Two-dimensional sketch of non-resonant (a) capacitive and (b) inductive FSS filters with equivalent circuit and spectral properties^[10].

1.3 Low-e coating with enhanced selectivity

Double-pane windows with low emissivity coating was developed shortly after the first oil crisis in the early 1970s. It was introduced to the market with the aim of reducing the energy loss by space heating. Compared to traditional simple glazing, Insulated glass units (IGU) provide for a 4x reduction in heat loss, resulting in significant savings. These new windows had an considerable economic impact and has become the industry standard for glazing in industrialized nations. Nowadays, IGUs consist of a triple glazing with two low-e coatings. According to the simulation tool provided by the glass company AGC^[11], this type of windows achieve a thermal transmittance, also known as U-value, as low as $0.6 \text{ W}/(\text{m}^2 \text{K})$. The increase in thermal insulation of the glazing is generally accompanied by a decrease in the total energy transmission of the same glazing. For highly glazed buildings and warm climate, this reduction of solar gains is desired and can be useful to reduce the risk of overheating. A previous study^[12] showed that, for buildings without adaptive solar shading, a lower SHGC value is to some extent favorable: it tends to strongly reduce temperature variations inside the room, which increases thermal comfort and limits heat rejection due to overheating. In countries with cold climate, the additional solar gains in households could lead to energy savings in space heating. The implementation of a selective coating could potentially increase the SHGC back to the original value of 73 % (without low-e coating). Therefore it is interesting to investigate new approaches which allow an increase in solar transmittance (τ_e) and SHGC while maintaining a low thermal emissivity ϵ . Table 1.1 presents typical values of SHGC and U-values for single, double and triple glazing, with or without low-e coating.

1.3 Low-e coating with enhanced selectivity

Table 1.1: Optical properties of single, double and triple glazing taken from AGC online configurator^[11]. For each glazing the panes consist of a clear-white 4 mm thick float glass and the air gap distance is always 14 mm filled with air or argon (Ar). It is compared to the insulated glazing unite with one (or two for triple glazing) plus 1.0 low-e coating.

	Single		Double		Triple glazing	
	-	Low-e	-	Low-e	-	Low-e
T_v	0.9	0.84	0.82	0.77	0.75	0.65
SHGC	0.88	0.56	0.8	0.51	0.73	0.41
U-Value (air) [$W/(m^2K)$]	5.8	3.2	2.8	1.4	1.8	0.8
U-Value (Ar) [$W/(m^2K)$]	-	-	2.6	1.1	1.7	0.6

As mentioned in section 1.2, the FSS structure for microwave transparent windows transmits the electromagnetic waves in the centimeter range (mobile communication) and reflects the shorter micrometric IR waves (heat radiation of a black body at 300 K). In the case of a selective low-e coating for high solar heat gains, the opposite effect is desired: a high transmittance at low wavelength (VIS and NIR) and a strong reflection at higher wavelength. In fact, the selectivity aspect of these two applications shares the same physical fundamental theory.

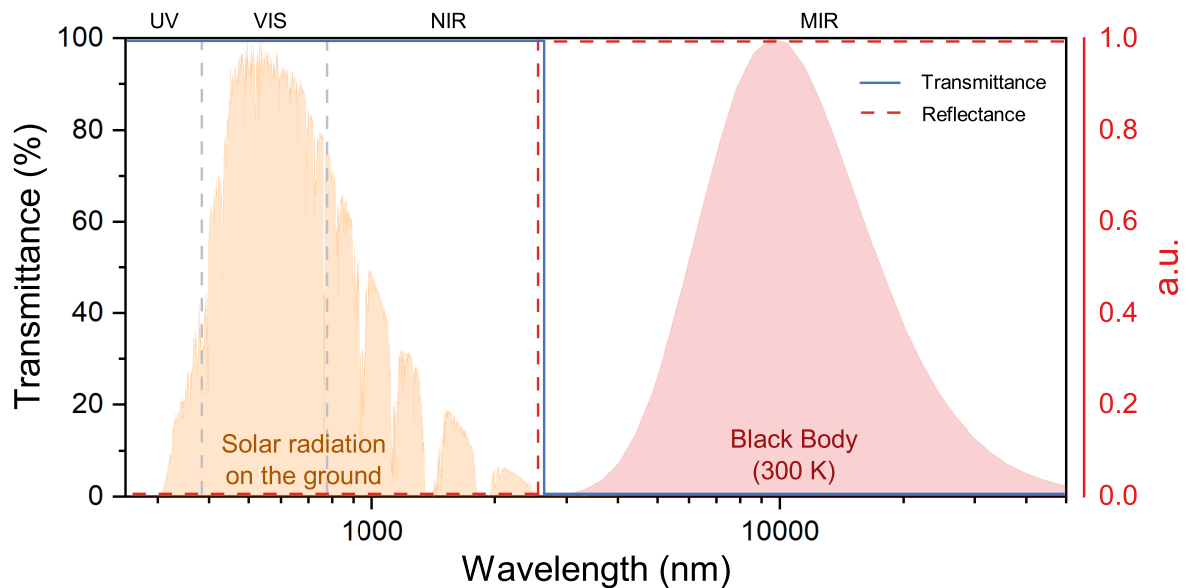


Figure 1.4: Transmission and reflexion spectra of an ideal solar gain coating. The solar irradiance is transmitted to the building and the radiation from a blackbody at room temperature is reflected to keep the heat inside the room. Both, the global solar irradiance at 1.5 AM and the blackbody radiation are normalized between 0 and 1 and expressed in arbitrary unit (a.u.) as reference.

Introduction

As shown in Figure 1.3a, the patch array can be described (using Equivalent Circuit Modeling Technique^[13,14]) as a capacitive filter which acts as high-pass filter (letting through signal with higher wavelength, i.e. lower frequencies). This is the case for the microwaves transparent glazing. In contrast, the mesh structure (Fig. 1.3b) is described as an inductive filter and acts as a low-pass filter (letting through signal with lower wavelength, i.e. higher frequencies). The ideal selectivity of a insulating windows for cold climate (reflexion and transmission spectra) is illustrated in Figure 1.4. The red and blue lines give the theoretical most effective coating that optimizes the transmission of solar heat gain while minimizing the radiation losses in the mid-IR. This specific selectivity can be enhanced by structuring the low-e coating on the windows into a metal mesh (inductive-type FSS filter). The principle of selective wave propagation through this filter is explained in Figure 1.5 and simulated in Figure 1.6:

- For short-wavelength radiation in the spectral range of solar radiation (VIS-NIR), the openings are comparatively large to the wavelength, and the electromagnetic wave is transmitted. Therefore the metal mesh is transparent (see Fig. 1.5a and 1.6a).
- For long-wavelength radiation in the spectral range of thermal radiation (mid-IR), the dimensions of the openings are comparable to the wavelength, and the electromagnetic wave is reflected. Therefore the metal mesh has a low thermal emissivity meaning that it is a good infrared-reflector (see Fig. 1.5b and 1.6b).

The dimension of the structures is a crucial parameter to achieve optimal selectivity. Part II of this thesis will present a finite-difference time-domain (FDTD) simulation combined with nano-imprint lithography process to investigate the dimensions of the FSS structure and their application as selective coatings in buildings.

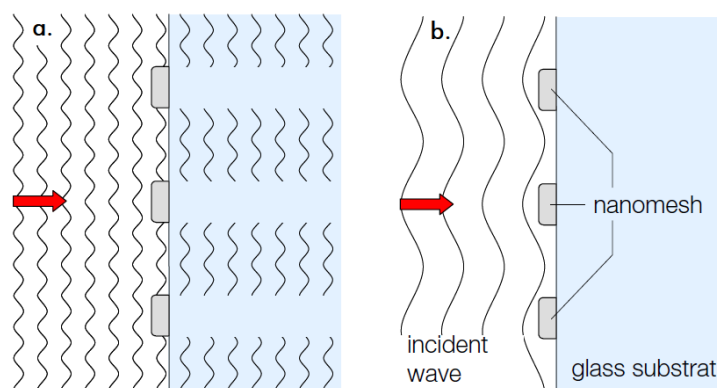


Figure 1.5: Wavelength selectivity achieved by a metal mesh structure. **(a)** Short-wavelength radiation are transmitted and **(b)** long-wavelength radiation are reflected. Image taken from M. Meier's thesis^[15].

1.4 Smart windows with adaptable selectivity

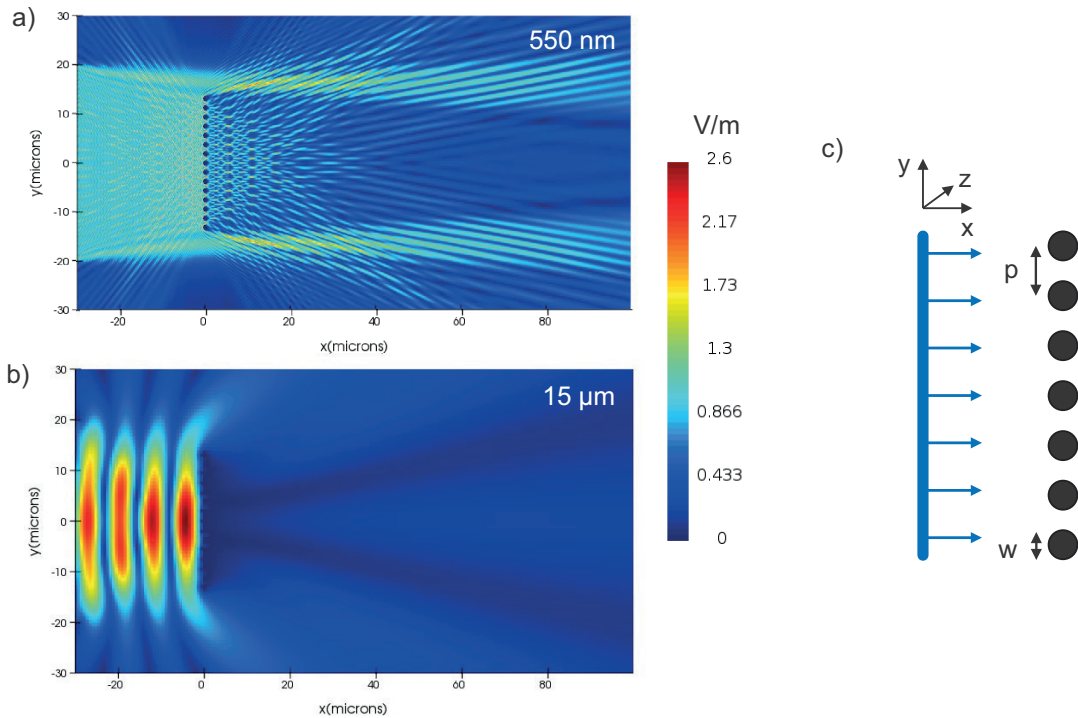


Figure 1.6: FDTD simulations of a plane wave traveling through metallic pillars with a periodicity $P = 1'875$ nm and a width $w = 1'000$ nm. The colors indicate the E-field (in V/m) distribution of a perpendicular (z-direction) polarized electromagnetic wave at a wavelength of (a) $0.55 \mu\text{m}$ and (b) $15 \mu\text{m}$. (c) presents a top view of the design with xyz-axis.

1.4 Smart windows with adaptable selectivity

For highly glazed office buildings and modern houses, even in Switzerland a form of solar protection is needed in order to avoid excessive cooling needs in summer and to provide thermal as well as visual comfort. External blinds are susceptible to mechanical failure, and cannot be used in high-rise buildings. Internal blinds are much less efficient, because the solar energy enters the building and has to be later extracted. In many cases, sun protection coatings have to be used. However, those greatly limit solar heat gains in winter. Indeed, the type of glazing required in a building for minimal energy consumption depends greatly on the climate. The diagram shown in Figure 1.7 depicts the performance requirement in building glazing for various climate. On one hand, in the case of hot climate, SHGC should be kept to a minimum in order to avoid overheating and the transmittance in the visible spectrum (T_v) should ideally stay high enough to allow for adequate visual comfort. On the other hand, for cold climate, SHGC should be kept as high as possible to increase the solar energy gain, leading to energy savings in space heating. It is important to keep in mind that the U-value also plays an important role in the design of insulated glazing and is closely related to the SHGC. In general, the thermal coefficient should be kept as low as possible to reduce energy

Introduction

loss in heating and cooling.

Electrochromic (EC) windows are good candidates to save energy by adapting the transmittance of the glass to the seasonal change^[16]. Current EC windows can be used in the hot and tempered climate but they fail to satisfy cool climate requirements because of their low SHGC and T_v values. Part III of this thesis will focus on finding solutions to improve electrochromic devices (ECDs) by increasing the solar heat gain in cool climate.

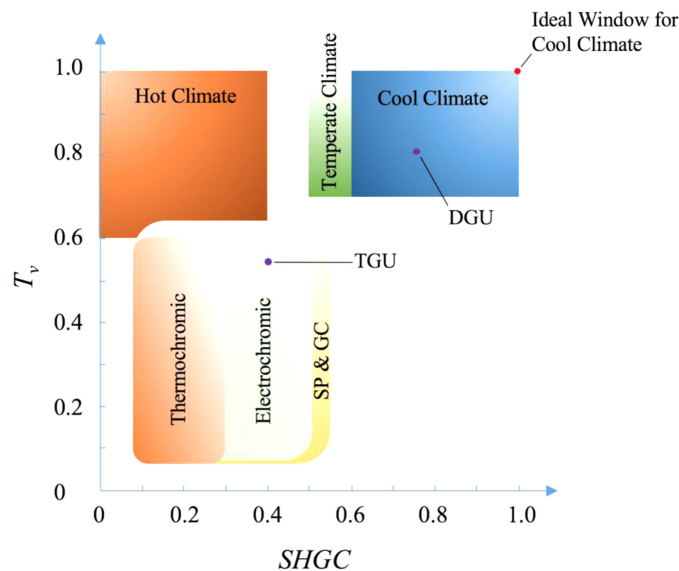


Figure 1.7: Performance requirements for various climates and performance of thermochromic, electrochromic, suspended particles (SP), and gasochromic (GC) windows. Figure taken from Daqiqeh Rezaei's journal article^[17].

As shown in Figure 1.8, ECDs consist of two electrodes, an electrochromic material as cathode, an ion storage as anode and ion conductor (electrolyte) in between. A voltage can be applied between the two electrodes and the ions migrate between the cathode and the anode, leading to coloration or bleaching. This electrochemical process is similar to an electric battery. In present-day electrochromic windows, the time that EC windows take to reach 90% of the minimum or maximum value of its visible solar transmittance can range between 7 - 20 minutes^[18]. It is not homogenous (starting from the edges of the panes) and lead to an unnatural dark-blue tint on the colored state. The color neutrality of the device could be improved by changing the electronic properties of the EC material and will be explored more in details in Chapter 6. The switching speed and homogeneity depends on two parameters: the ion diffusion in the multi-layered device perpendicular to the substrate and on the lateral charge transport parallel to the substrate plane. The first limitation was solved by increasing the porosity of the EC film which improves the ion diffusion^[19]. The lateral transport depends mostly on the conductive electrode used in the ECD.

1.4 Smart windows with adaptable selectivity

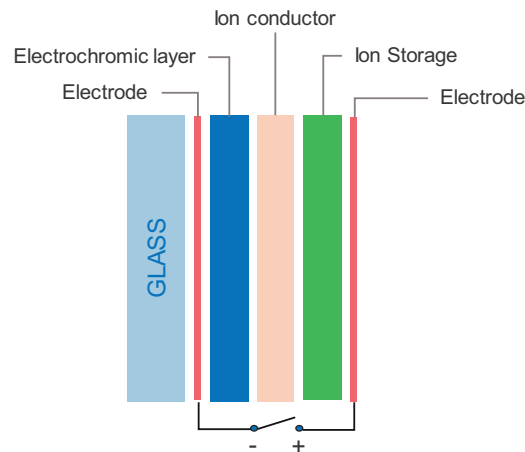


Figure 1.8: Schematic illustration of an electrochromic window.

Nowadays, most switchable window technologies are based on transparent conductive oxides (TCOs). Indium tin oxide (ITO) belongs to TCOs with excellent performance regarding the trade-off between transparency and electrical conductivity. However, its scarcity^[20] and high demand are making it increasingly more expensive^[21] Moreover, because of its plasma frequency located around 1300 nm, ITO coatings reduces the transmittance in the NIR spectrum^[22]. Knowing that 50% of the solar heat radiation is delivered in the NIR spectrum^[23], the ITO coating greatly reduces the potential of energy saving in the winter period. Additional considerations about ITO used as TCOs are listed in table 1.2.

Table 1.2: Advantages and disadvantages of ITO as a transparent conductive oxide

Advantages	Disadvantages
- High optical transparency ($T = 85 - 95 \%$)	- Rare metal with rising cost
- Low sheet resistance ($R_s = 10 \text{ Ohm/sq}$)	- Limited supply and high demand
- Tunable work function (4.2 to 5.3 eV)	- Low transmittance in NIR
	- Brittle material (not suitable for flexible devices)
	- High temperature annealing
	- DC magnetron sputtering (vacuum)
	- Low stability during electrochemical processes

As presented in Figure 1.9, metal meshes have a superior potential regarding the cost/conductivity ratio. The metal mesh usually covers a small fraction of the surface and stays transparent in the NIR spectrum. Therefore, metal meshes are especially well suited for window applications where large solar heat gains are desired. This specific application is further investigated in Chapter 5 with the introduction of a hierarchical metal mesh based ECDs.

Introduction

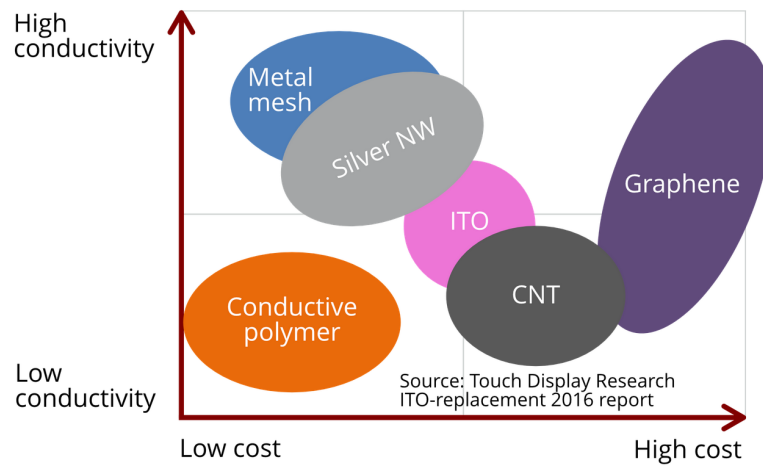


Figure 1.9: ITO replacement comparison chart, metal mesh is a promising candidate for high conductivity and low cost transparent conductive films. Figure taken from ITO-Replacement Report 2016^[24].

1.5 Research aims and objectives

This doctoral thesis is aiming at the development of low-e coatings and metal meshes for optoelectronic applications. Each part of the project aim to achieve a specific objective and is guided along research questions about light interaction and electronic transport properties listed below:

How do EM waves interact with different designs of laterally structured conductive coatings and what are potential applications?

Part I: How much are centimetric waves attenuated by a window with a structured coating and how do these waves propagate inside a building?

Method: Laser post-treatment processing of energy-efficient windows in buildings and high signal transmission for mobile communication frequency up to 40 GHz.

Part II: How does the transmittance of a light depends on the dimensions of the structure?

Method: Use of specific FSS to enhanced the selectivity of insulating glazing and find the ideal dimensions of structures to achieve optimal selectivity in the electromagnetic (EM) spectrum.

Part III: How can electrochromic devices be improved to be used as adaptive solar protection?

Method: Increase solar transmittance by incorporation of nano/micro meshes and doping of electrochromic material to improve the selectivity and color neutrality.

1.6 Structure of the thesis

To address the above research aims and objectives, this document is structured as follows:

Part I presents new research of an innovative laser treatment for high transmission of modern telecommunication frequencies through energy-efficient windows.

Chapter 2 introduces a post-treatment laser processing of double glazing windows after assembly. The linewidth of the laser-ablated pattern is reduced and their performances in the 5G high frequency range (26 - 40 GHz) is characterized.

Chapter 3 provides a quantification of the propagation of microwaves in buildings through laser-treated energy-efficient windows. The signal attenuation of a mobile phone is measured

Introduction

in an office room and compared between windows with and without laser treatment.

Part II

Chapter 4 explores the light/matter interaction through finite-difference time-domain (FDTD) simulation with the aim of achieving highly selective low-e coatings. The theory behind the method is first explained and then the model is validated by experimental characterization.

Part III introduces the concept of electrochromic devices for seasonal adaptive solar heat gains.

Chapter 5 present a hierarchical metal mesh based ECD with a transmittance switching in the full spectral range of solar radiation.

Chapter 6 investigate the use of molybdenum doping in tungsten trioxide coating to improve the color neutrality and spectral selectivity of ECDs.

Chapter 7 concludes with the main findings and summarizes the scientific questions presented above. Finally, it gives an outlook including the the design of a multifunctional smart window for countries with varying warm/cold climate.

MICROWAVE TRANSPARENT WINDOWS **PART I**

2 WIDE BAND-PASS FREQUENCY SELECTIVE SURFACES

This chapter is based on the published journal paper^[25]:

Fleury, J., Lanini, M., Pose, C., Burnier, L., Salvadè, A., Zimmermann, E., Genoud, C. and Schüller, A., 2020. Wide band-pass FSS with reduced periodicity for energy efficient windows at higher frequencies. *Applied Physics A*, 126, pp.1-11.

Author contribution for the journal paper:

In this article, JF designed the research with the support of all co-authors. JF conducted the laser treatment of the samples and the analysis of the results. JF carried out the simulations based HFSS Designer and was responsible for the submission process. ML conducted the simulations based on the Equivalent circuit theory and prepared a first draft of the paper. JF wrote the final version of the manuscript and carried out the submission and review process. All co-authors supported in revising and finalizing the manuscript.

In this chapter, a computer simulation model and an experimental characterization of energy saving glazing transparent to mobile communication frequency up to 40 GHz is presented. A previous study done in our group showed that laser structured energy efficient windows with a frequency selective surface greatly reduces the microwave attenuation for frequencies below 5 GHz, while preserving the thermal insulation properties of the window. Here, the focus is laid upon higher frequency range (26 - 40 GHz), considering the rapid evolution of the carrier frequencies. Several energy efficient windows were built and laser scribed with a cell periodicity varying between 2 to 0.5 mm. A computational model based on electric equivalent circuit behavior and transfer matrix representation is shown, and compared to a real set of measurements taken from manufactured glazing.

2.1 Introduction

The demand for mobile communication between persons and between objects (Internet of Things, IoT) is continuously and rapidly increasing. In order to satisfy these needs, higher frequency range in the order of 3.5 to 40 GHz are being allocated for new telecommunication technologies such as 5G^[26]. It allows for larger bandwidth, higher data rates, lower latency and increased capacity on the network^[27]. At the same time, the standards for energy efficient buildings require the use of double or triple glazing (being the norm) with one or two low emissivity (low-e) coatings which allows for better thermal insulation. Low-e coatings are composed of multiple oxides and silver thin films. While being highly transparent in the visible light, these insulated glass units (IGU) induce a strong reflectivity for shorter wavelength in the middle and near infrared spectrum. On the one hand, this coating greatly reduces the thermal losses due to infrared (IR) - radiation of objects at room temperature, but on the other hand, because of the metallic nature of silver, it also attenuate drastically (around 30 dB) the signal transmission of modern telecommunication frequencies (TF)^[28].

In order to solve this issue, signal repeaters are installed in new buildings and trains to increase the signal strength indoors. This solution reveals several drawbacks such as, the cost, the electricity consumption and the dependency on only one technology. Furthermore, the repeaters will have to be replaced every 5 to 8 years for each new telecommunication technology^[29].

Table 2.1: Literature review about bandpass FSS on insulating glass unit.

Reference	FSS design	Unit cell dimension (mm)	Unit cell periodicity (mm)	Engraving width (mm)	Ablated area (%)	Frequency range (GHz)	Transmission loss (-dB)
[28]	2 x 2 Cross-dipole	64	100	4 ; 8	2.4 ; 7.7	0.8 - 6	10 - 25
[30]	2 x 2 Square ring	37.5	40	0.5	7.1	0.1 - 3	1 - 54
[31]	Ring	60	65	2	9	0.57 - 4.5	5 - 30
[32]	Rings	21, 40	100	8	6.4	0.9, 1.8	5 - 20
[33]	Slit	150	172.5	1	~ 4.6	0.1 - 2	2 - 16
[34]	Hexagons	16.5	60	0.82	10	0.1 - 6	7 - 35
[35]	Square patch	19	20	1	9.75	0.62 - 2.02	0 - 20
[36]	Square patch	39.965	40	0.035	0.2	0.85 - 5	15 - 33
[36]	Square patch	1.965	2	0.035	<4	0.85 - 5	1 - 10

Another approach consists in using the physical properties of a frequency selective surface (FSS). FSS are repetitive patterns designed on a thin film coating with the aim to reflect, trans-

mit of absorb electromagnetic waves based on their frequency.^[4,35,37] By etching the coating of an energy efficient window with a repetitive pattern, the attenuation in the TF domain can be greatly reduced. There have been several examples of the application of this technique to decrease the attenuation of the low-e coating, mostly by removing great part of the coated surface, degrading thermal isolation^[31,38,39]. A literature review on existing designs are shown in Table 2.1. Most studies focused on FSS with a unit cell dimension from 20 to 100 mm and engraving width from 1 to 8 mm resulting in ablation surface of 5 to 10% of the coating. In a recent work^[36], a novel design for a FSS was proposed in order to reduce the attenuation in the TF domain from its usual 30 dB to merely 1 to 3 dB. This was achieved using a laser-scribed grid with a cell periodicity of 2 mm and an engraving width of 35 μm , thus ablating only a small percentage of the coating and preserving the thermal isolation properties of the window. This solution was analyzed for frequencies up to 5 GHz, yielding satisfactory results and good agreement with the simulation model.

As the evolution in the communication advances at a rapid pace, it should be asked if the proposed solution will still be valid as time goes by. In the case of telecommunication technologies, the carrier frequencies increase throughout the years. The objective of this work is to analyze the behavior of our novel design at higher frequencies, namely in the 26 - 40 GHz band. The report is organized as follows; first, the materials and methods used for the simulation and the experiments are thoroughly described. Then, the results are presented. Finally, a discussion is carried out on the comparison between the experimental and simulated data.

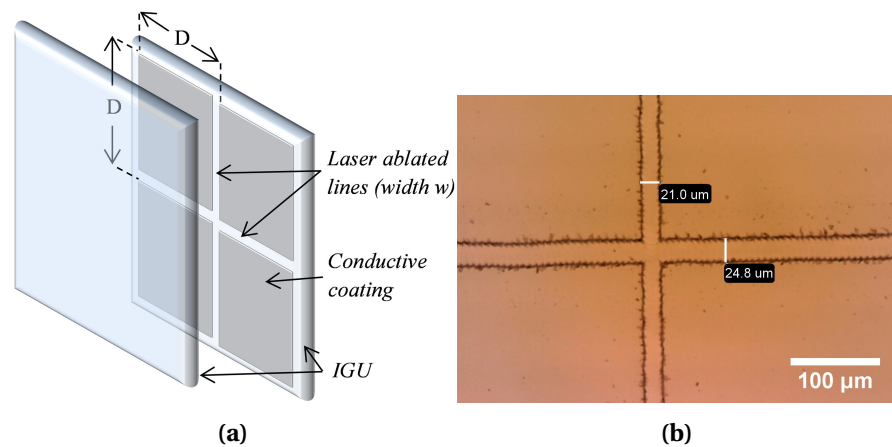


Figure 2.1: (a) IGU model used in this study, D describes the cell periodicity of the FSS and w the engraving width. (b) Microscope image of the laser structure coating with a engraving width of $w = 25 \pm 5 \mu\text{m}$.

2.2 Methodology

2.2.1 Equivalent circuit theory

The proposed FSS design, a $D \times D$ mm square patch grating, is described as a non-resonant structure with capacitive behavior. Figure 2.1a illustrates the configuration of the IGU which is composed by two 4 mm glass panes and a 12 mm air gap. One of the glass surface facing the air gap is coated with a low emissivity transparent layer and laser-scribed.

The simulation method used in this study to analyze the frequency response of the FSS follows the analytic averaged approach developed by Costa et al. [13]. This method consists of an electric circuit equivalence model, where three transmission lines, $TRL_{1,2,3}$, are used to simulate the glass-air-glass dielectric composition of the IGU. Between the first glass and the air gap, a parallel circuit represents the equivalent behavior of the coating. If the coating is non-existent, the equivalent parallel circuit is an open wire (Fig. 2.2a); if there is a full coating, the circuit consists only of a resistor R_{coat} (Fig. 2.2b); and if the coating is etched with the squared pattern, it is represented as a resistor R_{fss} and a capacitor C_{fss} in series (Fig. 2.2c).

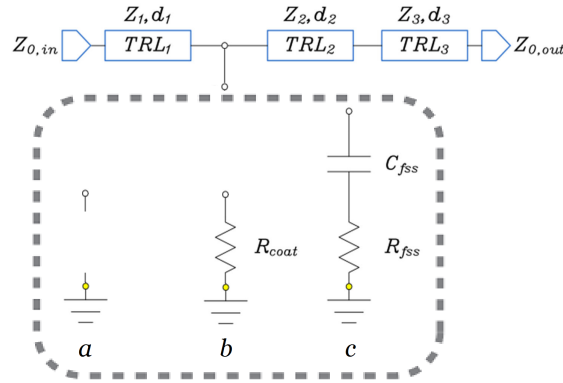


Figure 2.2: Possible equivalent circuits for the IGU. (a) no coating, (b) full coating, (c) FSS surface.

Considering an incident sinusoidal-type wave normal to the IGU with structured coating, the values of the equivalent circuit can be calculated as follows [13,40]:

$$C_{fss} = \frac{D\epsilon_0(\epsilon_{r1} + \epsilon_{r2})}{\pi} \ln\left(\frac{1}{\sin(\pi w/2D)}\right) \quad (2.1)$$

$$R_{fss} = R_{coat} \frac{D^2}{(D-w)^2} \quad (2.2)$$

where D is the cell periodicity of the FSS, w the engraving width, R_{coat} the surface resistivity of

the coating and ϵ_{r1} , ϵ_{r2} the relative dielectric permittivities of air and glass. For the impedance of the transmission lines, the formula for a dielectric slab is applied:

$$Z = \sqrt{\frac{\mu_0}{\epsilon_0 \epsilon_r}} \quad (2.3)$$

which yields $Z_{0,in} = Z_{0,out} = Z_2 = 376.7 \Omega$ for the free space and the air gap between the glass panes.

2.2.2 Simulation

To simulate different IGUs, a model consisting of four stacked slabs (glass - FSS coating - air - glass) has been run using Matlab. Each slab is represented through a 2-by-2, frequency-dependent transmission matrix, and the overall behavior is obtained by chain-multiplying the matrices respecting the order of the slabs. The FSS coating is modeled as a capacitor in series with a resistor according to Figure 2.2c and Eqs. 2.1 and 2.2, using $R_{coat} = 4.1 \Omega$, a standard value for the windows used. Both the glass and the air gap are modeled as a low loss dielectric, the first one using values of $\epsilon_{r2} = 7$ and $\tan\delta = 0.008$ (an initial approximation for the dielectric loss for the glass^[41]), and the second one with $\epsilon_{r1} = 1$ and $\tan\delta = 0$. Additionally, the angle dependency of the IGU is modeled using a full-wave simulation (ANSYS electronic desktop HFSS Designer). The dielectric constant of glass is the same as the one mentioned before. HFSS simulations is also used to validate the equivalent circuit model.

2.2.3 Manufacture of the windows

IGUs with a size of 500 x 500 mm and a precision in the construction around 1 mm were used. A laser-scribing process was performed as post-treatment where the laser beam was focused on the surface #3 (the internal face of the second glass) of the IGU in order to ablate the low-e coating (soft double silver coating: iplus top N+T from AGC Group). This process was performed using a 1064-nm nanosecond-pulsed Ytterbium fiber laser. The patterns were drawn using a CNC-machine (at a speed of 6 m/min) guiding the movement of the laser head, while the sample stayed motionless. The coating was ablated by laser pulses at a frequency of 10 kHz and a power of 5 W. Figure 2.1b presents a microscope image of the ablated coating. A more detailed explanation about this method can be found in previous works^[9,36].

Seven energy efficient windows were produced. The size and configuration of all IGUs were the same and the engraving width for the samples with a laser structure coating was $25 \pm 5 \mu\text{m}$. The periodicity of the grid was varied between 0.5 mm, 1.0 mm, 1.3 mm, 1.6 mm and 2.0 mm. Finally two windows were tested as reference: one without coating and one with a full low-e coating.

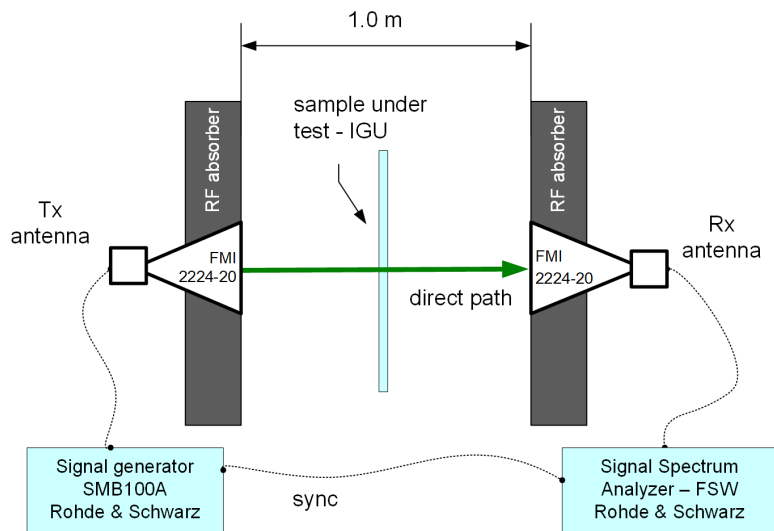


Figure 2.3: Experimental setup for assessing the properties of the IGUs.

2.2.4 Experimental setup

The measurements were performed in a free space setup, as the wavelengths are really short at these high frequencies. Using a pair of highly directional antennas, the multi-path effect may be disregarded, as the signals that are not in the direct path arrive at the receiver with high attenuation. A similar statement can be made regarding the edge effect.

The following equipment has been used:

- The IGUs were fixed to a wooden holder mounted on wheels in order to easily adjust the incidence angle.
- Signal generator SMB100A Rohde&Schwarz, 0.1 to 40 GHz.
- Signal and Spectrum Analyzer FSW Rohde&Schwarz.
- BNC cable for 10 MHz reference signal.
- Ethernet cable for communication between the instruments.
- 2x Horn antennas FMI 2224-20. The antennas were mounted on a tripod and surrounded with absorbers. The distance between the emitter and receiver was 1 meter.
- Low noise amplifier PE15A 4050.
- 2 wave-guide coax transmission.
- 2 microwave coax cables.

The tracking signal generator and the spectrum analyzer have been synchronized. An initial calibration of the system was performed with every instrument on site, without any window. A representation of the setup is depicted in Figure 2.3.

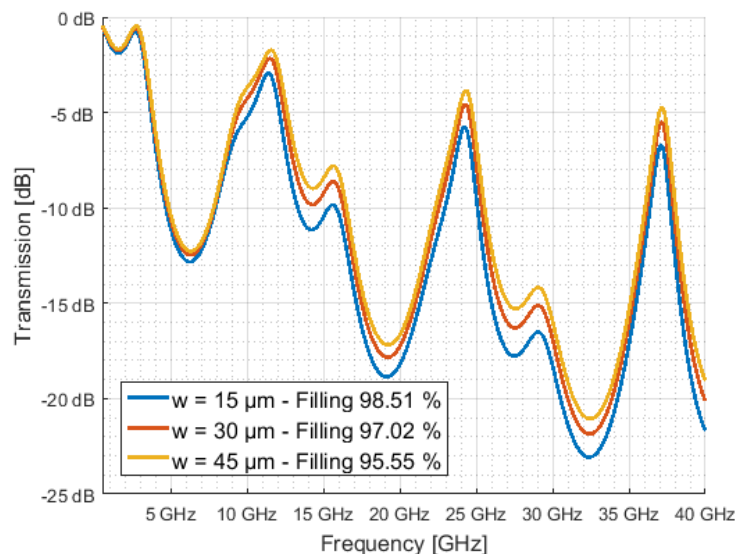


Figure 2.4: Simulation of the transmission loss (S_{21}) for varying engraving width w and fixed periodicity $D = 2$ mm. Clear transmission bands due to the resonance cavity created by the air gap can be seen at 12, 24.5 and 37 GHz. Two secondary peaks around 15 and 30 GHz are due most likely to the finite thickness of the glass panes.

2.3 Results

2.3.1 Computer simulation

Several parametric simulations using the first method described in section 2.2 were carried out. The most representative are shown below. All simulations consider a normal incident wave. Regarding the FSS grid, different periodicities and scribing widths were simulated in order to analyze how much does the frequency response change with this parameters.

Figure 2.4 presents the results of the simulation for a wide frequency range up to 40 GHz. The simulated curves illustrate the influence of the scribing width, for a fixed 2 mm periodicity, 4 mm-wide glass panes, and an air gap of 12 mm. It can be seen that in the whole frequency range the attenuation decreases as the engraving width increases.

The reflection respond of the FSS strucutre for varying cell periodicity is illustrated in Figure 2.6. The simulation shows a bandpass filter behavior at specific frequencies similar to the one of a Fabry-Pérot interferometer which will be explained more in details in the discussion section. Additionally, considering a simplified two-port lossless network, the relation between the reflection (S_{11}) and the transmission (S_{21}) can be described as:

$$|S_{11}|^2 + |S_{21}|^2 = 1$$

Chapter 2. Wide band-pass Frequency Selective Surfaces

In our case, the structure can reasonable be considered lossless as the reflected signal is dispersed outside.

In Figure 2.5, a simulation is done for a variation in cell periodicity, while maintaining the engraving width constant at $35 \mu\text{m}$. For decreasing cell periodicity, the secondary peak increases and finally a broad transmission band is formed. The effect can be explained by the fact that the laser scribed coating become more and more transparent to the microwaves. The thermal losses due to laser scribing depend on the surface fraction of the ablated area. In the case of 0.5 mm periodicity, 13.5 % of the coating is removed which will likely reduce the thermal performance of the glazing. Figure 2.7 presents a comparison between IGUs where the remaining thermal coating is kept constant at 95.06 %, i.e. the relation $\frac{D}{w}$ is the same. A 100 % filling corresponds to a full coating, without etching.

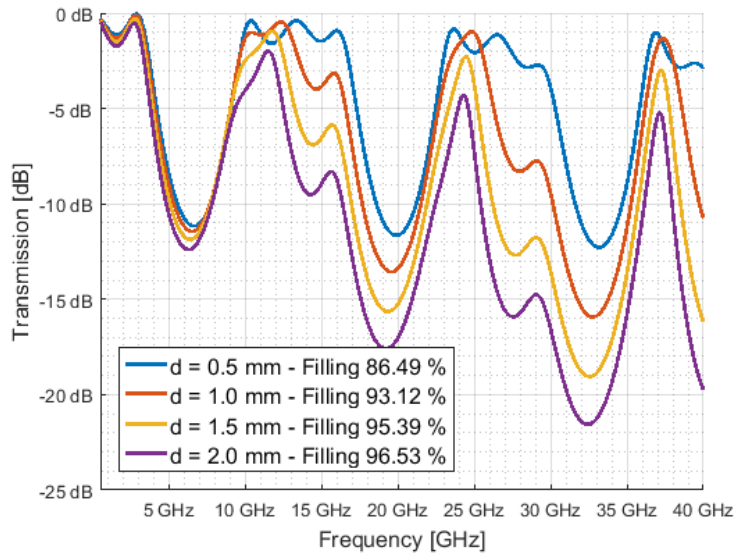


Figure 2.5: Simulation presenting the transmission loss (S21) for varying cell periodicity D and fixed engraving width $w = 35 \mu\text{m}$. For narrower D , the transmission increases which leads to broader band-pass.

For a constant $\frac{D}{w}$ relation, the transmission improves for smaller cell periodicity. Hereby the R_{fss} maintains its value. At the same time, C_{fss} decreases and the total impedance with respect to ground of the FSS increases. Varying the width of the glass and air gap corresponds to modifying the length of the transmission line in the equivalent electric circuit, thus producing a shift of the response in the frequency domain. The overall attenuation can be reduced either by increasing the engraving width or by decreasing the cell periodicity. The latter is preferred, as it renders a lower attenuation in all the frequency range, while maintaining a higher thermal isolation (by having less coating removed). The glass and the air gap widths do not affect the attenuation evenly in all the frequency range. This may be critical when working at frequencies

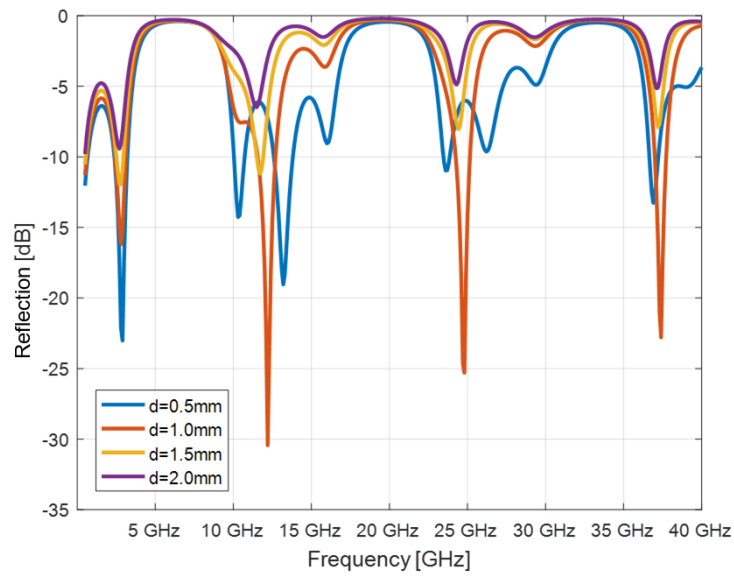


Figure 2.6: Simulation presenting the reflection respond (S11) for varying cell periodicity D and fixed engraving width $w = 35 \mu\text{m}$. Very sharp reflection minima are obtained at well defined frequencies.

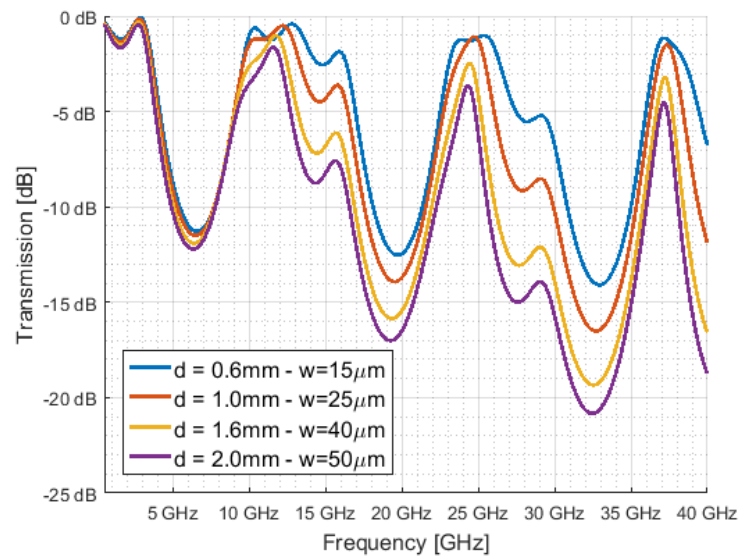


Figure 2.7: Simulation showing the transmission loss (S21) for a constant D/w factor at 95.06%. For smaller D and w factors, the transmission is improved.

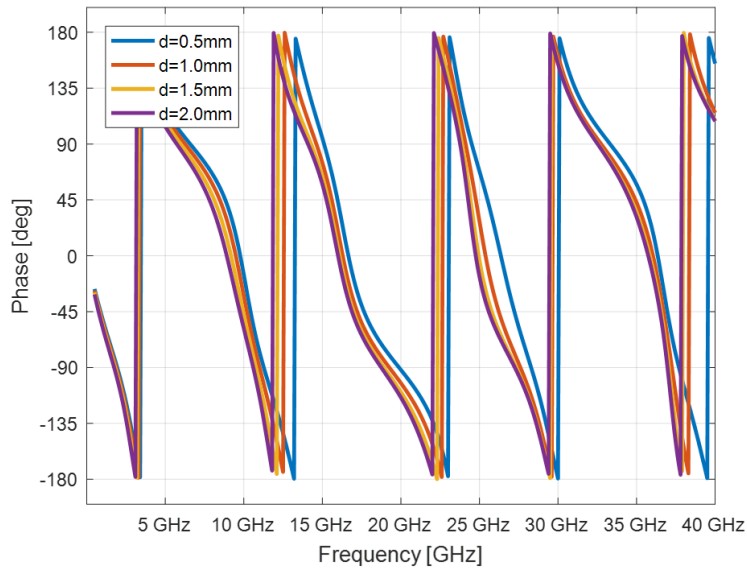


Figure 2.8: Simulation presenting the transmission phase variation at different cell periodicity.

near the zones where the response changes abruptly.

The phase characteristics of the FSS structures are illustrated in Figure 2.8. The phase rotates gradually through the full range from -180° to $+180^\circ$. The phase is moved by 1° for a change of approximately 28 MHz.

2.3.2 Experiments

The experimental measurements are presented in Figure 2.9. Each set of measurements consists in 1001 points spaced evenly in the 26 - 40 GHz range. As the measurements taken were relatively noisy, and for the sake of comprehension, all the curves were smoothed using robust local regression with weighted linear squares and the dashed lines represent the envelope of the raw data.

2.3.3 Comparison between simulated and experimental data

To compare the experimental data sets to a simulated frequency response, some special considerations were made. For one sample to another and at different atmospheric pressure, the air gap may vary up to 1 mm. Small variations in this parameters would yield very different results in the frequency domain. Additionally, the $\tan\delta$ coefficient was not properly measured, so the initial guess $\tan\delta = 0.008$ should be checked. The cell periodicity and the engraving width are supposed to be more precise, as the first one is a result of a pattern generated by a CNC machine, and the second one depends also on the scribing laser.

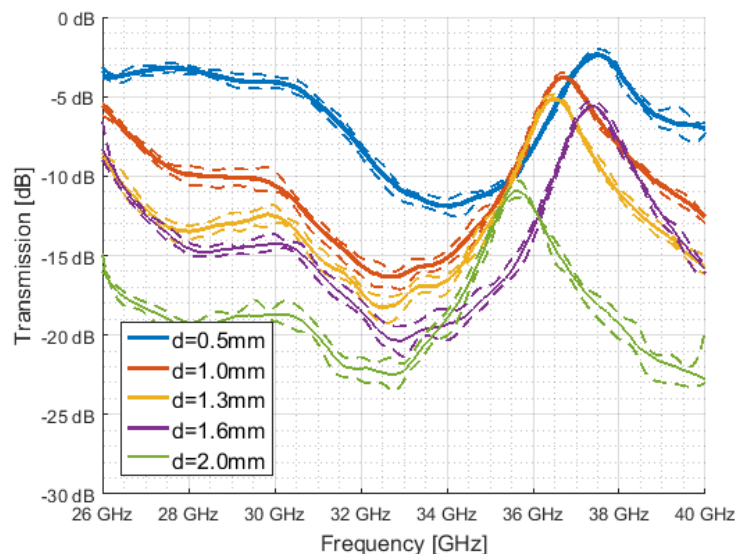


Figure 2.9: Experimental measurements for IGU with structured low-e coating and varying cell periodicity D . The solid lines show the smoothed measurements, while the dashed lines represent the envelope of the raw data. The resonance peak for each IGU moves between 35.5 and 37.5 GHz due to a small different in air gap distances. Generally, the transmission increases for narrower cell periodicity.

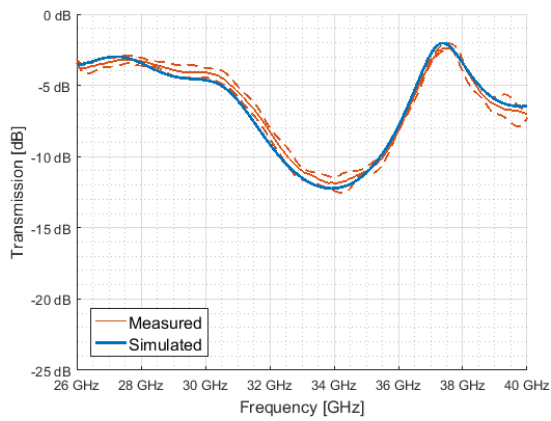
Table 2.2: Range of fit parameters

Parameter (unit)	Min	Max	Step
Cell size (mm)	0.5	2.0	0.1
Engraving width (μm)	15	35	10
Glass thickness (mm)	3.7	4.3	0.1
Air gap (mm)	11.8	13	0.1
$\tan\delta$	0.005	0.04	0.005

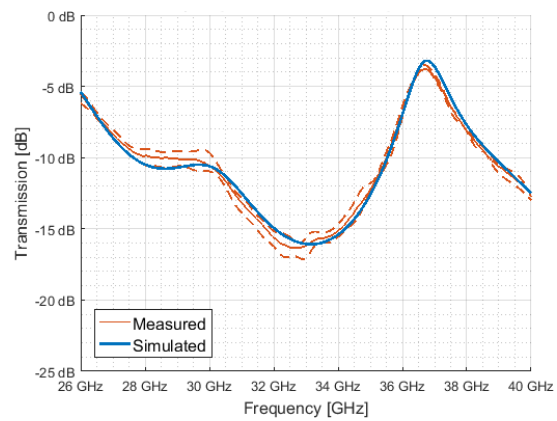
Then, instead of checking against one simulation model, the solution was to generate a dataset for a great number of possible setups, doing a parametric sweep over the cell periodicity, engraving width, glass thickness, air gap distance, and dielectric loss coefficient. The range of each parameter is depicted table 2.2. As a result, a workspace with the frequency response of 34944 different setups was obtained. To find the best fitting curve for each experimental setup, a comparison was performed using the squared difference sum. It is expected that, for all the setups, the best fitting curves have all the same characteristics.

For every measurement, the best simulations shared a glass thickness of 3.8 mm, an engraving width of 25 μm and a $\tan\delta$ value of 0.02. As all the glass panes came from the same patch, it was expected for them to share this values. A measurement of the glass thickness after

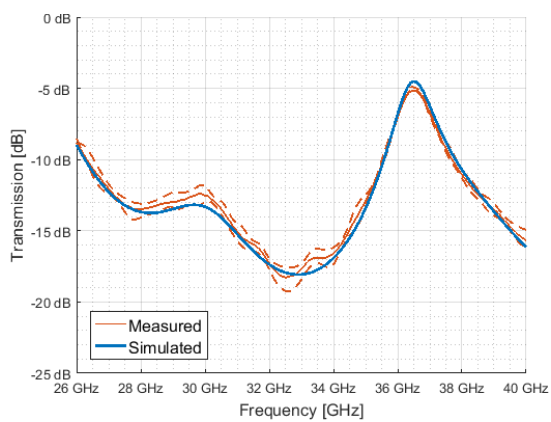
Chapter 2. Wide band-pass Frequency Selective Surfaces



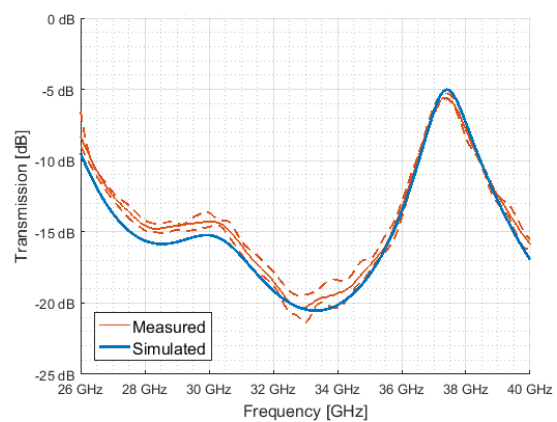
(a) $D = 0.5$ mm, fitted air gap = 12.1 mm



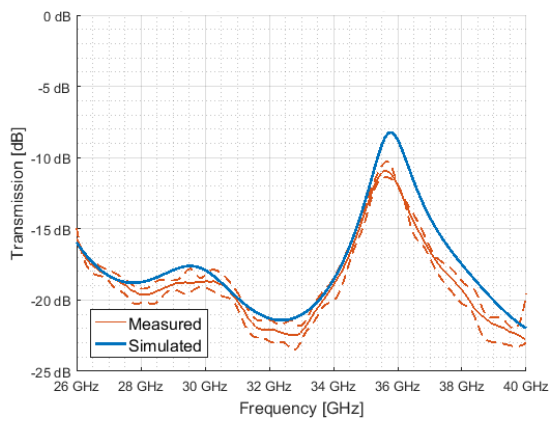
(b) $D = 1.0$ mm, fitted air gap = 12.4 mm



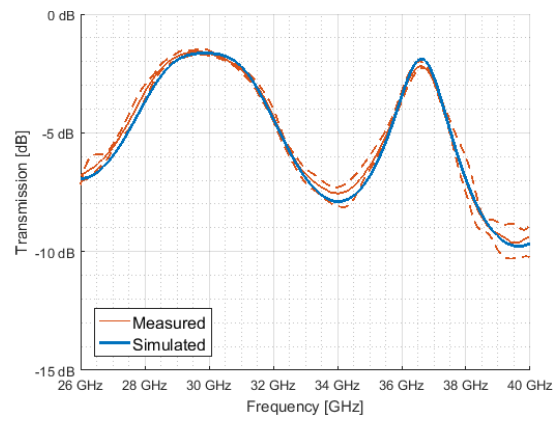
(c) $D = 1.3$ mm, fitted air gap = 12.5 mm



(d) $D = 1.6$ mm, fitted air gap = 12.1 mm



(e) $D = 2.0$ mm, fitted air gap = 12.8 mm



(f) no coating, fitted air gap = 12.4 mm

Figure 2.10: Comparison between the measured and simulated signal attenuation. The solid lines show the smoothed measurements, while the dashed lines represent the envelope of the raw data.

performing the experiments confirmed that the glass was indeed 3.8 mm thick and not 4 mm, as initially designed.

The comparisons are presented in Figures 2.10a to 2.10e where the best-fitting curve for each case is represented by the blue line. The optimal simulation for the air gap parameter is, respectively, 12.1 mm, 12.4 mm, 12.5 mm, 12.1 mm and 12.8 mm, with a span of 0.7 mm.

$\tan\delta$ value was higher than expected, but it was constant for all the best fits, it is believed to be the correct value. The simulations also let us know the width of the air gap; these parameters would not be easy to measure with precision on a finished IGU, and may be used to check the quality of the finished window without using an invasive method.

To show the limitations of the IGUs used on trains and buildings, and the improvements obtained with the proposed method, two additional figures are presented. In Figure 2.10f the frequency response of an IGU without coating is shown. This means that the IGU is composed only of two glass panes separated by an air gap, with the same characteristics as other configurations. The best fitting curve in this case is also for a 3.8 mm thick glass, and a $\tan\delta$ value of 0.02; this time with an air gap of 12.4 mm. The transmission factor can never reach 0 dB, due to a non-zero value of $\tan\delta$ in the glass, and because of the occurrence of peaks due to the resonance of both, the air gap and the glass.

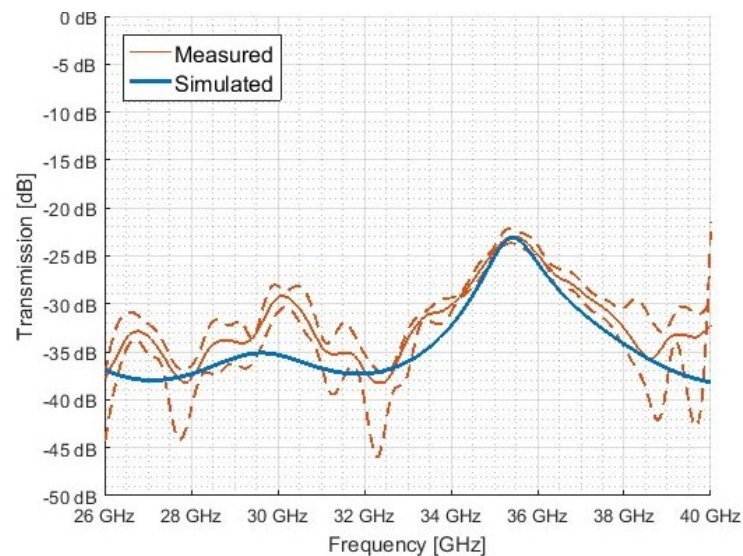


Figure 2.11: Comparison between the measured and simulated signal attenuation for an IGU with a full coating. The fitted air gap parameter is 12.4 mm. The experimental transmission shows a large envelope due to the strong attenuation of the IGU.

Figure 2.11 shows the same IGU with a full coating, but without any laser scribing. This is currently the state of the art for train windows. It shows a strong attenuation in all the measured frequency range (note that this figure has a different vertical scale). In this case,

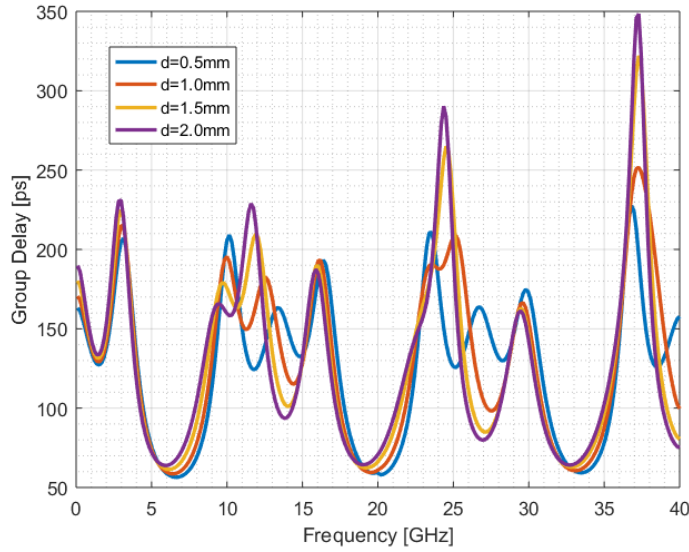


Figure 2.12: Simulated group delay for varying cell periodicity D . The group delay remains below 350 ps for all samples at frequencies from 1 to 40 GHz.

it can be noticed that the fit between the theoretical and experimental response is not as precise as for the previous cases. The reason seems to be because of a noisy measurement, due mainly to a low level signal at the receiver, as the attenuation is over 30 dB. The experimental measurement is evidently noisier than those for the scribed IGUs. This time, the envelope of the smoothed measurement is around 7 dB wide when the signal decreases below 30 dB, while in the previous measurements it was no more than 2 dB wide in the worst case. For example, the peak at 35.5 GHz, has an attenuation of 25 dB and shows less noise and a better agreement with the theoretical response.

2.4 Discussion

2.4.1 Group delay

As shown in Figure 2.12, the group delay for each periodicity lies between 50 and 350 ps. The variation in group delay is a result of the dispersion of the signal components when passing through the device under test. As a comparison, modern mobile networks (i.e. 5G NR), which uses Orthogonal Frequency-Division Multiplexing (OFDM) ^[42], can effectively compensate signal delays up to 300 ns ^[43]. This technology employs large number of narrowband sub-carriers and equalization techniques to minimize multi-path propagation effects ^[44]. The group delay calculated in this study are three order of magnitude below the admissible value and consequently will not degrade the rate of transmission.

2.4.2 Resonance cavities

As shown for example in Figures 2.4, 2.5 and 2.7, three sharp transmission peaks can be observed at repetitive frequencies. The occurrence of these pass bands is due to the resonant cavity between the two glass panes which induces a constructive interference in a manner being analogous to an optical Fabry-Pérot interferometer^[8]. A resonance occurs when the size of the cavity g_{th} is equal to half of the wavelength of the incident wave. It can be calculated using equation 2.4.

$$f_{res} = i \cdot \frac{c}{2g_{th}n} \approx i \cdot \frac{c}{2g_{th}\sqrt{\epsilon_r}} \quad (2.4)$$

with ϵ_r being the relative permittivity of the material, c the speed of light and i a natural number.

The quality of these resonators is given by its finesse, which is defined as its free spectral range divided by the bandwidth at full width at half-maximum (FWHM) of the resonance^[45]. For a plasmonic resonance, the observed bandwidth would correspond to dephasing times between 100 and 300 ps^[46,47]. In the case of the IGU showed in Figure 2.4, the resulting finesse of the Fabry-Pérot interferometer is 9.3. Similarly, the quality of each resonance peaks is described by the Q-factor, which is defined as frequency-to-bandwidth ratio. The three resonances at 12, 24.5 and 37 GHz lead to Q-factors of, respectively, 3.7, 13.1 and 29.6. In the case of the comparisons showed in Figures 2.10a to 2.10e, the quality-factor for the resonance between 35 and 38 GHz (depending on the air gap) is calculated for each graph and gives following results: 21.2, 25.5, 27.4, 28.0, 32.2, 27.5 and 31.9.

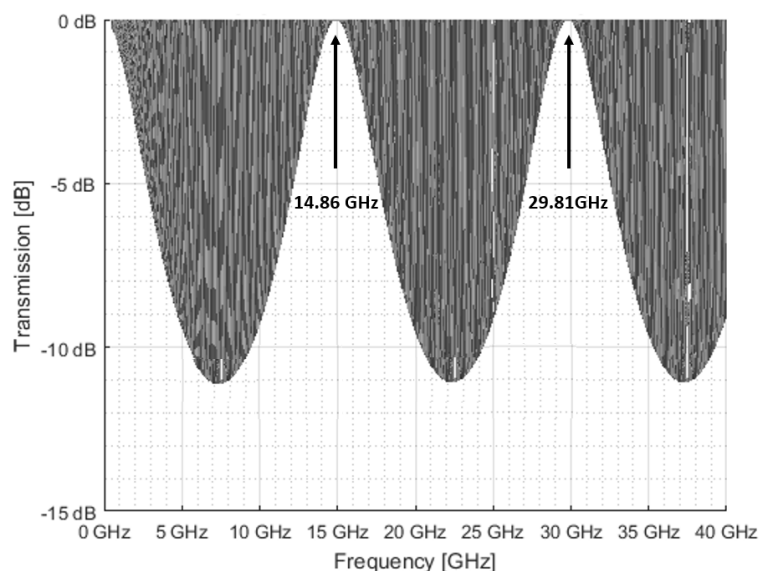


Figure 2.13: Simulation of the resonance frequencies due to glass cavities (without coating) where the air gap is varied. Specific frequencies at 14.86 and 29.81 GHz show excellent transmission for every air gap distance.

Chapter 2. Wide band-pass Frequency Selective Surfaces

Equation 2.4 can be used to determine the resonance frequency due to the air gap cavity between the two glass panes. In that case, one should use the relative permittivity of air ($\epsilon_r = 1$) and the glass-to-glass distance of $g_{th} = 12$ mm. The result gives a resonance frequency of $f_{res} = i \cdot 12.5$ GHz which is similar to the large transmission peaks observed in all measurements and simulations.

It can also be noticed that all graphs present smaller "shoulder" peaks at repetitive frequencies (approx. 15 and 30 GHz), which is especially pronounced in Figures 2.4 and 2.10f. In order to investigate this effect further, a large number of simulated curves are plotted in Figure 2.13 where the air gap is varying and the glass thickness is kept at 3.8 mm. This time, $\tan\delta = 0$ is assumed in order to keep the figure understandable. Whichever the value of the air gap, the response is contained within an envelope determined by the resonance induced by the glass cavities. The maximum and minimum peaks are spaced equally, and the resonance frequency can be calculated using equation 2.4. In the case of the glass cavity, $g_{th} = 3.8$ mm and $\epsilon_r = 7$ resulting in a resonance frequency of $f_{res} = i \cdot 14.9$ GHz which corresponds to the simulated values.

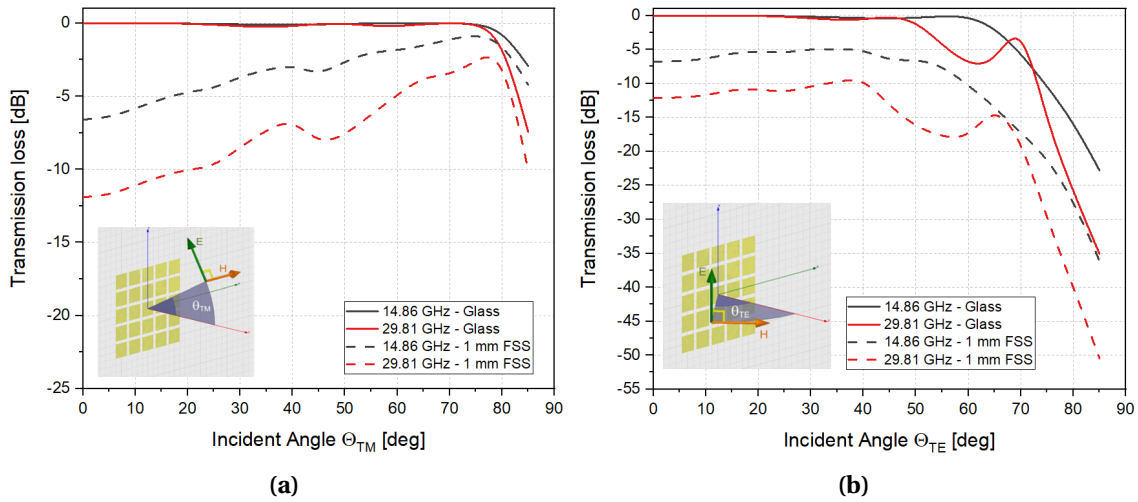


Figure 2.14: Simulated transmission loss at 14.86 and 29.81 GHz from normal (0°) to near-grazing ($\sim 90^\circ$) angles of incidence. The results are plotted for TM (a) and TE (b) polarization. The straight lines represent an IGU without any coating (only float glass) and the dashed lines an IGU with a 1 mm cell periodicity FSS.

This knowledge is useful for future design of IGU. The position and the width of the transmission bands depend on both the width of the air gap and the thicknesses of the glass panes. While the thickness of the glass can be controlled by the homogeneity and reproducibility of the fabrication process and remain therefore rather constant, the width of the air gap may vary to some extent due to variation in atmospheric pressure or temperature with a maximum deviation in the center of the IGU^[48]. According to equation 2.4, this would lead to a frequency shift of the FSS on the some area of the window.

Regarding the application of the novel glazing in trains and buildings, certain glass-to-glass distances and glass pane thicknesses appear frequently. These dimensions will define the positions and widths of the resulting pass bands. Therefore, specific frequency bands are advantageous for good coverage in mobile communication.

2.4.3 Angular dependency

As illustrated in Figure 2.3, the IGU is placed perpendicular to the plane of incident. In realistic applications, the incoming wave may reach the FSS at different angles and thus influencing the transmission loss. A full-wave simulation on angular stability of the FSS is carried out and illustrated in Figure 2.14. Electromagnetic-waves at frequencies of 14.86 and 29.81 GHz are simulated for a glass pane with and without low-e coating. For transverse magnetic (TM) mode (Fig. 2.14a) the transmission loss for a standard double glazing is especially transparent at these specific frequencies. By adding a 1x1 mm FSS coating on the glazing, the attenuation at incident angle is decreased to -7 and -12 dB for, respectively, 14.86 and 29.81 GHz. For angles up to 75°, the transmission loss increases to a value of -1 and -2.5 dB and then decreases rapidly. In regard to transverse electric (TE) mode (Fig. 2.14b), the standard glass pane shows similar behaviour than TM-mode excepting a noticeable decrease in transmission from 50°. The attenuation for the FSS-structured coating starts at the same value than the one for TM-mode at incident angle. It remains stable up to 40° and then decreases significantly. In the case of a cell periodicity of 0.5 mm, an improved transmission can be expected.

As wavelengths become smaller for higher frequencies (7.5 mm at 40 GHz), constructive interference may appear when interacting with a similar size FSS structure. This effect, called grating or Bragg lobes, creates secondary peaks in the signal and should be avoided. Generally, this phenomenon only occurs when the cell periodicity is greater than one wavelength at normal incident angle. In the case of a squared lattice type, the following grating lobe criteria can be approximated^[49]:

$$\frac{D}{\lambda_0} < \frac{1}{1 + \sin\theta_0}$$

D being the cell periodicity, λ_0 the wavelength and θ_0 the incident angle. Looking at the most critical case analyzed in this study, where $D = 2$ mm, $\lambda_0 = 7.5$ mm and theoretical grazing angle of $\theta_0 = 90^\circ$, the above mentioned criteria is still validated ($0.27 < 0.50$). No grating lobes should therefore occur at these frequencies.

2.5 Conclusion

The proposed square-FSS with narrower periodicity for energy efficient windows shows an improvement of microwave transmission in the 26 - 40 GHz band. Laser scribed low-e coatings were prepared, with a cell periodicity down to 0.5 mm and an engraving width of 25 ± 5 μm .

Chapter 2. Wide band-pass Frequency Selective Surfaces

The microwave transmittance of the double-glazing was measured and simulated in the high frequency range from 26 to 40 GHz. Excellent agreement between experiment and theory has been obtained. In experiment and simulation, we observe high microwave transmission at well-defined pass bands allowing good coverage in mobile communication inside trains and buildings.

In general, laser scribing patterns with small cell periodicity and narrow engraving width are preferable for high microwave transmission and high thermal insulation. The position and bandwidth of the pass bands depend on the glass-to-glass distance and the glass pane thickness.

3 COMBINING THERMAL INSULATION AND MOBILE COMMUNICATION IN BUILDINGS

This chapter is based on the published conference paper^[50]:

Fleury, J., Burnier, L., Delaporte, H., and Schüler, A. (2021, November). Combining thermal insulation and mobile communication in buildings: influence of laser-treated glazing on microwave propagation. *In Journal of Physics: Conference Series* (Vol. 2042, No. 1, p. 012181). IOP Publishing.

Author contribution for the paper:

In this article, JF designed the research with the support of all co-authors. JF and LB conducted the measurement campaign and JF analysed the results prepared the figures. JF wrote the manuscript and carried out the submission and review process. The topic was presented by JF as a talk during the 2021 CISBAT conference at EPFL, Lausanne.

In this chapter, the attenuation of microwave signal through laser-treated IGUs is analyzed inside the SolAce unit in the "NEST" research building at the Swiss Federal Laboratories for Materials Science and Technology (EMPA) in Dübendorf. Two configurations (with and without laser-treated glazing) were carried out by interchanging two hinged windows. The novel patterned coating can help increase the microwave signal for mobile communication in buildings. To the best of our knowledge, this is the first implementation and testing of laser-treated coating for energy-efficient glazing in the building sector.

3.1 Introduction

The demand for mobile communication between persons and more recently between objects (Internet of Things or IoT) is continuously and rapidly increasing. Simultaneously, modern energy-efficient windows (double and triple glazing) have become a standard in the building sector. The combination of modern insulating glass unit (IGU) and the large use of reinforced

Chapter 3. Combining thermal insulation and mobile communication in buildings

concrete leads to bunker-like buildings which are signal-proof to microwave transmission (acting like a Faraday cage). The signal attenuation is due to the low-e silver coating found in IGU which improves the thermal insulation but also reduces the microwave transmission by up to 30 dB^[8,9,36]. Several studies have been carried out to effectively measure the signal loss caused by IGUs in buildings^[5-7]. This attenuation reduces the throughput which in turn leads to poor internet and phone call quality inside modern buildings. At the same time, the ever-increasing use of IoT in households and offices leads to higher demand for reliable network throughout the buildings^[51]. As the 5G mobile technology is rolling out, IoT will increasingly rely on the 5G network which improves the response time and extends the number of connected devices. The influence of IGU on 5G mmWave bands has already been investigated in different studies, especially for double glazing windows^[25,52,53].

The aim of this study is to show that a specific laser treatment carried out on the selective low-e coating can strongly improve the transmission of microwaves in buildings. The focus is laid upon further investigating the influence of triple glazing and examining the spatial propagation of microwaves inside a room.

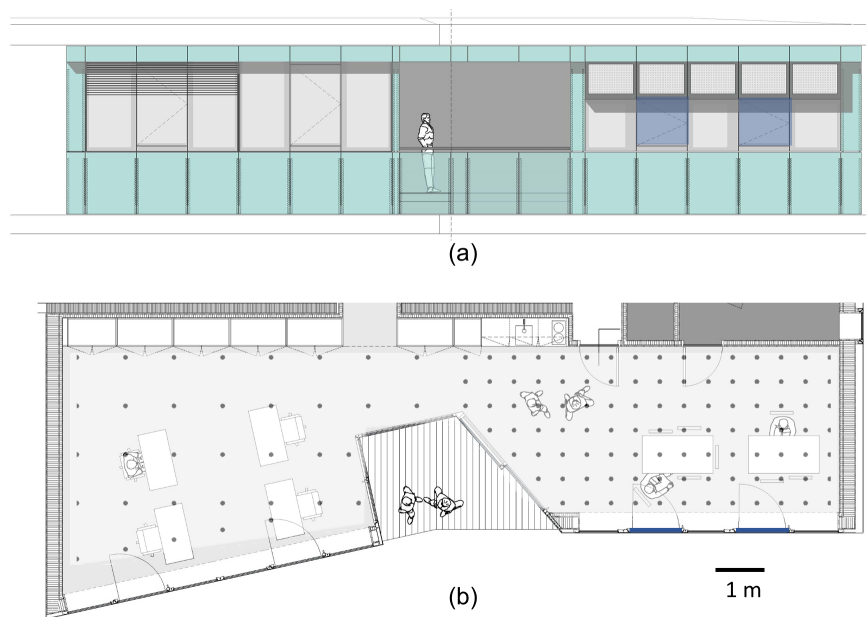


Figure 3.1: (a) Architectural plan of the south-west façade and (b) Top view of the SolAce unit where each dot represents one measurement. In both Figures, the two windows that were replaced with microwaves transparent windows are shown in blue.

3.2 Methodology

The study was carried out in November 2018 in the SolAce unit which is part of "NEST": a modular research and innovation building at EMPA in Dübendorf^[54]. SolAce focuses on two main

goals: maximum energy generation on the façade and optimum comfort for residents inside the unit. The energy production is achieved by solar photovoltaic (PV) cells and solar thermal collectors with colored glazing which are built into the façade (as shown by the turquoise panels in figure 3.1a). In order to understand how the EM waves for mobile communication are propagating inside a building, a series of twin measurements were performed. In the first configuration, standard IGUs with triple glazing and two low-e coatings were used. For the second part, two hinged windows (as shown in blue in figure 3.1a) were interchanged with laser-treated glazings. The layout of the triple glazing window which has a U-value of $0.5 \text{ W/m}^2\text{K}$ and g-value of 59 %, can be seen in figure 3.2a. Figure 3.2b and 3.2c show, respectively the laser scribing process used to treat the low-e coating and a microscope image of the resulting coating after ablation. This treatment does not affect the energy performance of the windows, g-value measurements and more information regarding the laser process is provided in previous works^[9,25,36].

A measurement device based on Nemo Handy software (developed by Keysight) was used to record the reference signal received power (RSRP) for the 4G Long Term Evolution (LTE) network over the entire surface of the unit. The receiver antenna was placed on a tripod at a height of 1.30 m above the ground. The pattern that was followed for the measurement is shown in figure 3.1b. It consisted of a 0.5 m square grid pattern on the right side of the unit (where the windows were changed) and 1 m grid on the left side where no modification was done between the two configurations. The study was carried out at a frequency of 1.8 GHz using LTE frequency-division duplexing (FDD) band 3 (also known as DCS: Digital Cellular System). The nearest cellular antenna (PCI 131) operated by Swisscom was situated on the top of the nearest building and 140 meters from the façade. Each measurement was done by averaging RSRP values over 30 seconds to reduce the possible fluctuation of the signal. Furthermore, a reference RSRP was taken every 15 minutes outside the unit (0.4 m away from the façade) and was used to calculate the attenuation caused by the walls and windows. In addition to the measurement done at NEST, a simulation was carried out on Ansys HFSS based on the same parameters presented by Burnier et al.^[9]. The HFSS-model was first validated with the simulation of a double glazing unit with low-e coating based on the measurements presented by Bouvard et al.^[36].

3.3 Results & Discussion

Figure 3.3 presents a full-wave 3D EM simulation of three different types of triple glazing windows: with two full low-e coatings, with two laser-treated low-e coatings and without any coating. It can be seen that the IGU with two silver coatings shows a significantly higher attenuation compared to the glazing without coating and with laser-treated coatings. At the frequency examined in this study (1.8 GHz) the signal strength was improved by 65 dB for an incoming wave normal to the surface of the glazing. Ångskog et al.^[5] measured the signal attenuation of triple glazing in a semi-anechoic chamber and found values between -30 and

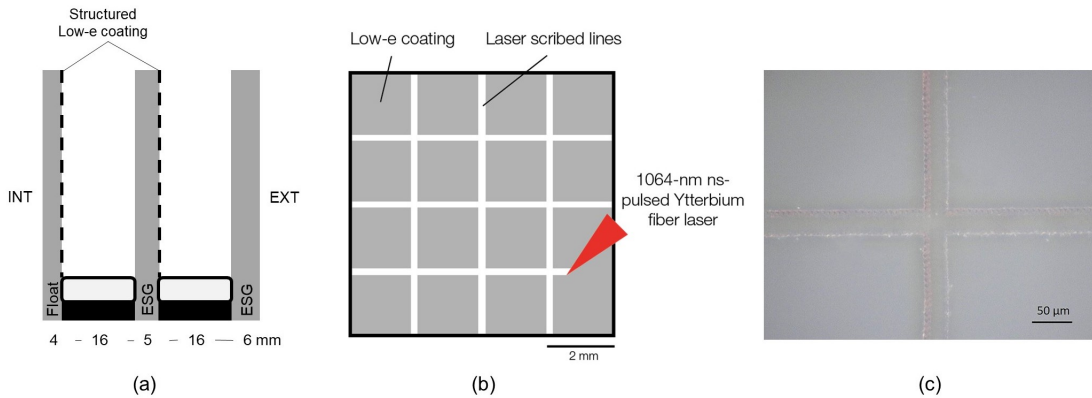


Figure 3.2: (a) Schematic design of a triple glazing window installed in the SolAce unit. The window consists of one 4 mm standard soda-lime (float) pane combined with two thicker (5 and 6 mm) ESG (tempered glass) panes with two air-gaps of 16 mm. Two structured low-e insulating coatings can be found on surfaces 3 and 5 (1 being the outer and 6 the inner surface). (b) Drawing showing the ablation principle of the insulating transparent coating. (c) Microscope image of the low-e coating after the ablation process. The width of each line is approximately 25 μm .

-60 dB, indicating a slightly lower attenuation than what we have obtained with our simulation. This inconsistency could be due to the fact that our model does not take into account the framing of the window, it simulates an infinitely large glazing without any edge-effects. The attenuation of the standard IGU with two low-e coatings may thus be overstated. It should also be noted that the behavior of the transmission loss of the EM wave depends on the angle of incidence, which in the case of the SolAce unit is around 30° . A comparable simulation with an incident angle of 30° for s and p polarization was also carried out and showed similar results. In the frequency range above 3 GHz the two IGUs (no coating and laser-treated) show a stronger attenuation which is most likely due to resonance frequencies between the glass cavities creating constructive and destructive interferences^[25].

A contour plot of the measured values is presented in Figures 3.4a and 3.4b. It was smoothed using thin-plate spline (TPS) algorithm with a total points increase factor of 200 and smoothing parameter of 0.0001. On the right part of the unit (where the windows were interchanged) a significant improvement in signal strength between the two configurations can be observed. This increase is especially visible in Figure 3.4b where the improved signal (in green) follows a straight line with an angle corresponding to the incident angle, i.e. 30° , starting from the opening of the two windows, suggesting a highly directional propagation of the EM waves inside the building. In both configurations, a green spot of higher signal power can be seen in the bottom-middle part. A possible explanation for this might be that the wall on the edge is made of agglomerated wood panel and wood fiber which is relatively transparent to the EM waves.

It should be noted that the values shown in Figures 3.4a and 3.4b are the relative difference

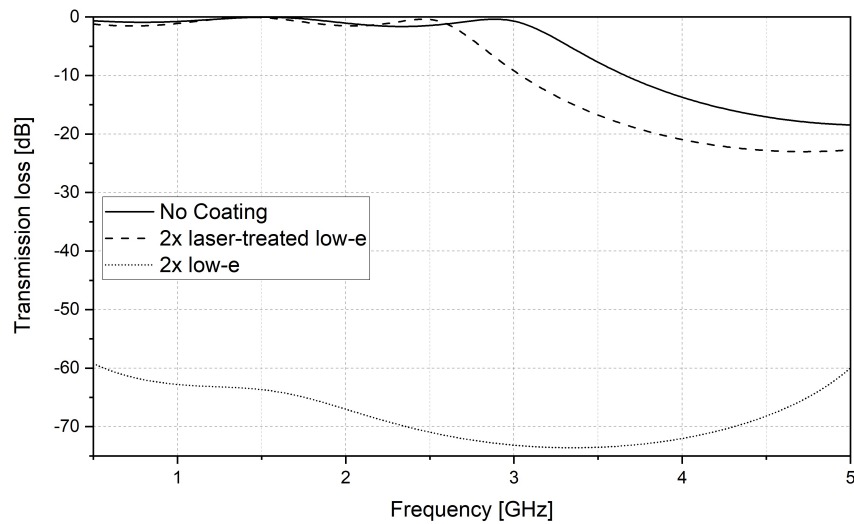


Figure 3.3: Simulation of EM waves propagating perpendicularly through a triple glazing unit based on the configuration shown in Figure 3.1a at frequency ranging from 0.5 to 5 GHz. The behavior of laser-treated window is comparable to an IGU without low-e coating, while the low-e coated glazing strongly attenuates the signal.

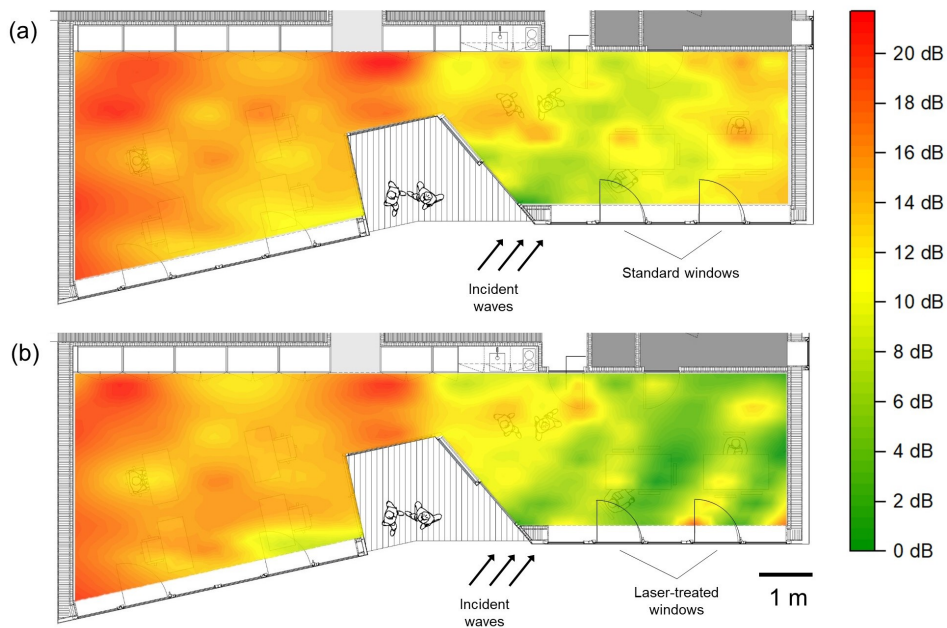


Figure 3.4: Contour plot presenting the change in RSRP values with a precision of ± 1.5 dB between the inside and outside of the unit where (a) shows the first configuration with standard IGU (triple glazing with two low-e coatings) and (b) two hinged windows on the bottom right were replaced with laser-treated glazing. This modification resulted in a highly directional increase of the signal strength.

in RSRP between the inside and outside of the unit. In order to assess the quality of the signal, the absolute RSRP value measured in dBm is more appropriate. RSRP represents a key measure of signal level and quality for modern LTE networks. Values below 80 dBm are described as excellent, between 80 - 90 dBm as good, 90 - 100 dBm as poor and no signal is received above 100 dBm^[55]. In the case of the SolAce unit, RSRP of 71 dBm was measured outside the façade and approximately 91 dBm in the top left corner of the room (see red spots in Figures 3.4a and b). It means that the LTE signal is described as "poor" even-though the emitting cellular antenna is located only 140 m away from the NEST building situated in a high population density near Zürich. The difference in RSRP between inside and outside (20 dB) represents a decrease in signal intensity by 100 times. This transmission loss is lower than the simulated value presented in Figure 3.3 which may be explained by high transmission through the wooden material used in the outer walls. As a contrast with the left side of the unit, the right part, equipped with laser-treated windows, shows excellent RSRP values around 75 dBm corresponding to an increase of 16 dB between the two configurations. It is thought that this result could be replicated to the entirety of the unit if all the windows were treated with our laser process. The reference signal received quality (RSRQ) and signal to noise ratio (SNR) were not evaluated for each points but a single measurement was taken and gave respectively, -9.2 dB and 7.3 dB which corresponds to excellent signal quality^[55].

3.4 Conclusion

Laser-treated low-e coatings for energy-efficient glazing was implemented in a building and the resulting signal strength for mobile communication was mapped. The data show a significant improvement in signal strength for the configuration with laser-treated windows compared to standard insulating glass units. RSRP values increased by up to 16 dB in the area area behind the newly installed windows. A signal attenuation contour plot of the SolAce unit shows a highly directional propagation of the wave which suggests that more than two windows should be treated to achieve better mobile communication in the entire unit. In conclusion, the novel laser-treated coating is especially valuable in the building sector to increase the quality of wireless networks which will become increasingly important for IoT and 5G mobile technology.

HIGHLY SELECTIVE LOW-E COATING **PART II**

4 THEORETICAL UNDERSTANDING OF METAL MESHES

This chapter explores the light/matter interaction through nano/micro-structured coatings using a simulation method based on finite-difference time-domain (FDTD). The aim of these numerical simulations is to optimize the design of a FSS coating to enhance the selectivity of an insulating glazing.

4.1 Introduction

As mentioned in section 1.3, it is desirable for insulating windows in cold climates to achieve a selective behavior in the transmittance of EM waves. Ideally, solar energy should be transmitted and mid-infrared radiations reflected, thus reducing the heating needs in buildings. To predict the amount of light that is passing through an object, it is needed to understand the interaction between light and matter. This can be achieved by solving Maxwell's equations for EM waves. The four Maxwell's equations are shown as a schematic drawing in Figure 4.1 and are explained below:

- (1) **Gauss' law:** the divergence of an electric field is proportional to the local density of charge ρ .
- (2) **Gauss' magnetism Law:** the divergence of the magnetic flux density is equal to zero, meaning that magnetic monopoles do not exist.
- (3) **Faraday's Law:** a time-varying magnetic field induces a spatially varying electric field.
- (4) **Ampère's law** (with Maxwell's addition): a variation in time of a electric field or a flowing electric current J will induce a rotational magnetic field.

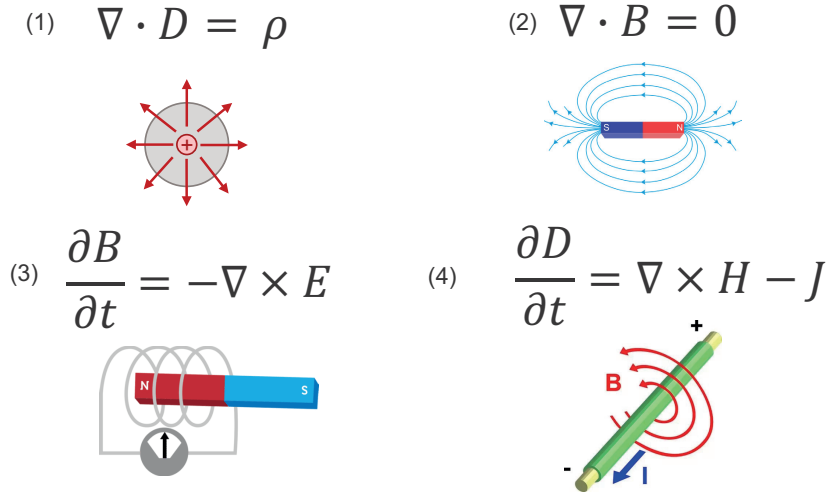


Figure 4.1: Illustration of Maxwell's equation in differential form: (1) Gauss' Law, (2) Gauss' Magnetism Law, (3) Faraday's Law and (4) Ampere's Law.

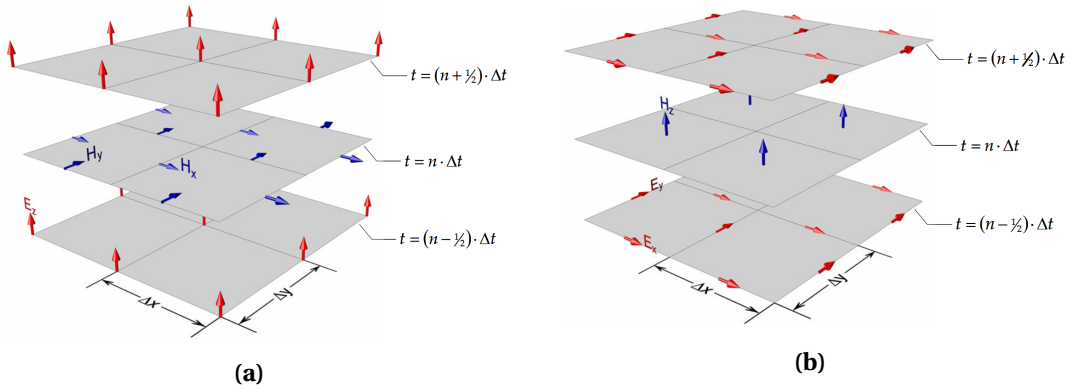


Figure 4.2: Visualization of the Yee cell and leapfrog time-stepping for (a) TM_z and (b) TE_z -mode. An unit cell of Δx by Δy is called a Yee cell. The E_z components are calculated at a distance Δx and Δy , the H components are located in the middle of the cell (in between the E components). Illustrations are taken from M. Meier thesis^[15]

For isotropic media, the relationship between the electric displacement field D and the electric field E or the magnetic flux density B and the magnetic field H are given as follows:

$$D = \epsilon \cdot E = \epsilon_r \cdot \epsilon_0 \cdot E \tag{4.1}$$

$$B = \mu \cdot H = \mu_r \cdot \mu_0 \cdot H \tag{4.2}$$

With ϵ being the permittivity (ϵ_0 , ϵ_r the vacuum and relative permittivity) and μ the permeability (μ_0 , μ_r the vacuum and relative permeability).

Maxwell's equations can be solved numerically using a finite-difference in time-domain (FDTD) method. This numerical analysis provides a full-wave solution without any physical approximation and is often used for the simulation of nano-scale optical devices such as nano-patterned metallic films for transparent electrodes^[56–58]. As shown in Figure 4.2, FDTD (also called Yee's method) consists of using a finite number of grid cells to solve Maxwell's differential equations by approximating derivatives with finite differences. In 2D, these equations can be expressed by the time and spatial distribution of the E and H field in the corresponding radiation modes TM_z and TE_z :

$$\begin{array}{c} \text{TM}_z\text{-mode} \\ \frac{\delta E_z}{\delta t} = \frac{1}{\epsilon} \left[\frac{\delta H_y}{\delta x} - \frac{\delta H_x}{\delta y} - J \right] \end{array} \quad (4.3)$$

$$\frac{\delta H_x}{\delta t} = \frac{1}{\mu} \left[\frac{-\delta E_z}{\delta y} \right] \quad (4.4)$$

$$\frac{\delta H_y}{\delta t} = \frac{1}{\mu} \left[\frac{\delta E_z}{\delta x} \right]$$

$$\begin{array}{c} \text{TE}_z\text{-mode} \\ \frac{\delta H_z}{\delta t} = \frac{1}{\mu} \left[\frac{\delta E_x}{\delta y} - \frac{\delta E_y}{\delta x} \right] \end{array} \quad (4.5)$$

$$\frac{\delta E_x}{\delta t} = \frac{1}{\epsilon} \left[\frac{\delta H_z}{\delta y} - J \right] \quad (4.6)$$

$$\frac{\delta E_y}{\delta t} = \frac{1}{\epsilon} \left[\frac{\delta H_z}{\delta x} - J \right]$$

In TM_z -mode (see Fig. 4.2a), the vertical electric field E_z at $t = (n + 1/2)\Delta t$ is calculated from the spatial distributions of H-field (H_x and H_y) at $t = n\Delta t$ and the initial value of E_z at $t = (n - 1/2)\Delta t$. This is depicted by Maxwell's third law shown in Equation 4.3. In the next time step ($t = 2n\Delta t$), the H-field is determined from the spatial distribution of E_z and $H_{x,y}$ in the previous time step (Eq. 4.4). This finite time-stepping process (leapfrog time-stepping) is repeated as the simulated EM wave travels as a wave package through the structures. An analogous process is carried out for the TE_z -mode presented in Figure 4.2b where the simulation starts with a vertical magnetic field H_z .

This chapter will first present the structural model used for the FDTD simulation. Its accuracy will then be validated by comparing it to the literature and experimental measurements. In a second step, various design parameters are optimized to achieve the optimal selectivity of a structured coating.

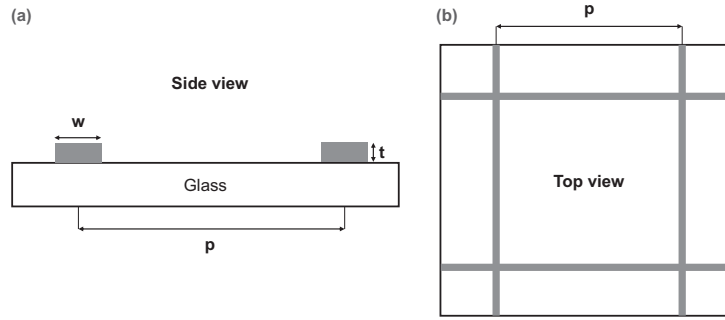


Figure 4.3: (a) Schematic cross-section and (b) top view of a structured coating with w being the width of one line, t the thickness and p the periodicity of one unit cell.

4.2 Materials and Methods

4.2.1 Numerical simulation

The optical response in transmission and reflection are simulated on a specially designed High-Performance Computer (32 cores, 256 GB of RAM and high-end 11.2 TFLOPS graphic card (NVIDIA Quadro RTX 5000)) using a commercial software package from ANSYS Lumerical^[59]. The general design of the structured coating is presented in Fig. 4.3, where p stands for the periodicity of the structure, w the width of the lines and t the thickness of the coating. As shown in Figure 4.4, the simulation consists of a glass substrate (with a fixed refractive index of 1.52) combined with a thin film of silver with n and k values taken from the literature^[60]. A XY-normal incidence plan-wave source is placed above the structure facing downwards to the z -direction (purple arrow). The light is polarized in the x -direction depicting the Transverse electric (TE) mode. Two monitors are placed; one inside the substrate (transmittance) and one behind the source (reflectance). The structured coating is designed as a unit cell combined with periodic boundary conditions in x and y directions to simulate an infinity array of openings. The simulated region is described by the orange box and is composed of perfectly matched layers (PML) at the top and bottom which absorb the EM waves propagating out of the box.

Since the FDTD method solves Maxwell's equations with no approximations, the possible sources of error comes only from the numerical error due to discretization of space and time, use of artificial PML absorbing boundaries, and error in the broadband material fits. In this simulation, a mesh size of one-third of the thickness is chosen for high-accuracy simulation of the conductive film. The PML layer is placed far away from the structure and additional absorbing layers are added to reduce possible errors. Finally the simulation is divided in two wavelength range (250 - 1000 nm and 1000 nm - 20000 nm) to improve the fit of the material n and k coefficients.

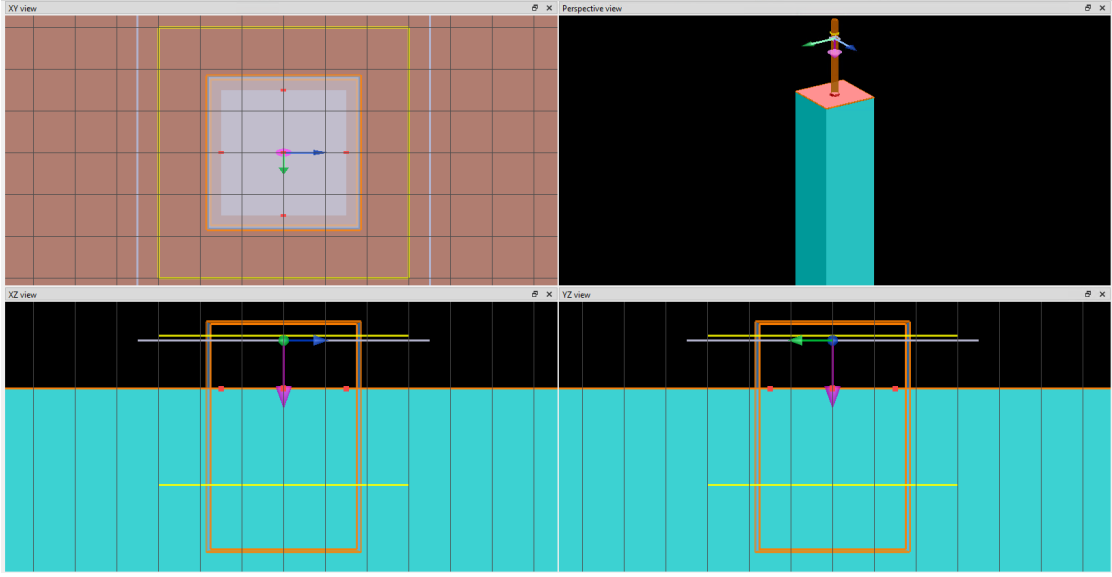


Figure 4.4: Layout Lumerical Software where the large blue rectangle represents a glass substrate of $4 \times 4 \mu\text{m}$ covered by a thin metal coating. The orange box describes the FDTD simulation region where the purple arrow is the incoming EM wave. To extend the model to an infinite array, periodic boundary conditions are used on the side of the model.

Optical values, T_v (visible transmittance) and T_e (solar transmittance), are calculated based on Eq. 4.7 and 4.8^[61,62].

$$T_v = \frac{\sum_{\lambda=380nm}^{780nm} D_\lambda T(\lambda) V(\lambda) \Delta\lambda}{\sum_{\lambda=380nm}^{780nm} D_\lambda V(\lambda) \Delta\lambda} \quad (4.7)$$

where D_λ is the relative spectral distribution of CIE Standard illuminant D65, $T(\lambda)$ the spectral transmittance, $V(\lambda)$ the spectral luminous efficiency for photopic vision and $\Delta\lambda$ the wavelength interval (in nm).

$$T_e = \frac{\sum_{\lambda=380nm}^{2500nm} S_\lambda T(\lambda) \Delta\lambda}{\sum_{\lambda=380nm}^{2500nm} S_\lambda \Delta\lambda} \quad (4.8)$$

where S_λ is the relative spectral distribution of the global solar radiation AM 1.5 (ASTM G173).

The absorptance can be determined using the conservation law, saying that the addition of the transmittance, reflectance and absorptance is equal to 1. Finally, the emissivity at 300 K is calculated using Eq. 4.9.

$$\epsilon = \frac{\sum_{\lambda=50\mu m}^{2.5\mu m} BB_{300K} A(\lambda) \Delta\lambda}{\sum_{\lambda=50\mu m}^{2.5\mu m} BB_{300K} \Delta\lambda} \quad (4.9)$$

with BB_{300K} being the distribution of a black body radiation at 300 K and $A(\lambda) = 1 - T(\lambda) - R(\lambda)$.

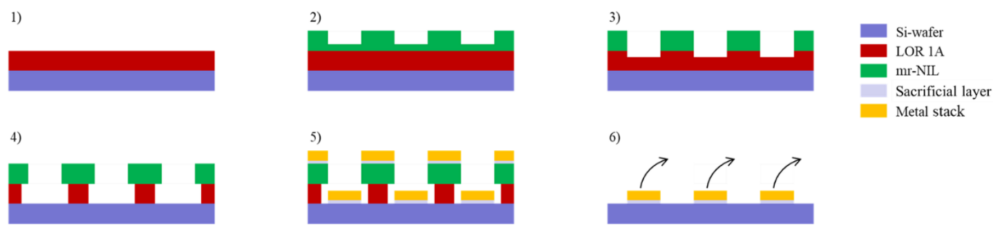


Figure 4.5: Schematics of nanoimprint fabrication process. Figure taken from Mitteramskogler et al. journal paper^[63]

4.2.2 Nano-imprint fabrication

A micro-hole array based on nanoimprint lithography was produced in collaboration with Tina Mitteramskogler from the company PROFACTOR in Austria. The nanoimprint process used for the replication of the nanostructured is presented as a schematic in Figure 4.5. A wafer is spin-coated with a photoresist (LORIA) (1) and imprinted using mr-NIL212FC-XP with a soft h-PDMS/PDMS stamp (2). After oxygen plasma etching (3) and wet chemical etching (4), the desired coating is deposited by plasma sputtering (5). Through immersion in MF24 A the mask is lifted-off (6) and the nanoparticles are ready for particle lift-off via wet-chemical etching of the sacrificial layer. The transmittance is measured using an ultraviolet-visible-near-infrared spectrophotometer (Agilent Cary 5000) in the wavelength range of 200 - 2500 nm.

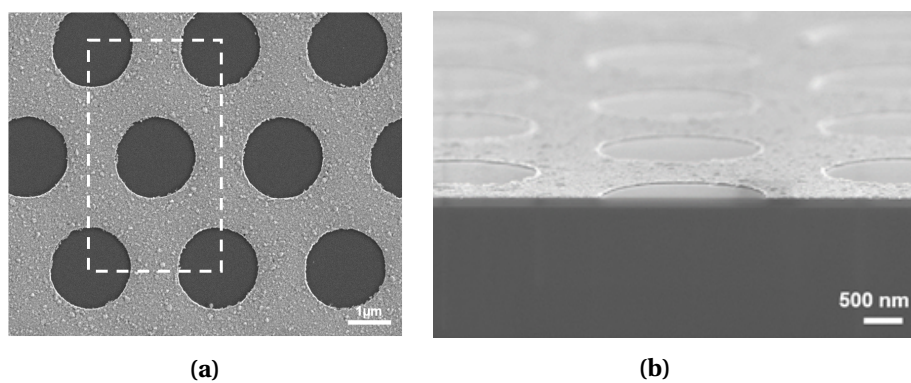


Figure 4.6: SEM images showing the micro-holes array achieved by nanoimprint lithography. (a) top-down view of the structures and (b) 10.5° tilted of a cross-section. The dashed rectangle describes the unit cell chosen for the FDTD simulation, it has a size of 3 x 5.2 μm .

4.3 Results & Discussion

4.3.1 Validation numerical model

Au nano-hole array

As shown in Figure 4.7, the simulation is based on the light/matter interaction of gold nano-hole array as a function of nano-hole diameter presented by Q. Tong et al.^[64]. Similar to their findings, a strong transmittance peak is observed around 1600 nm and rises interesting questions about the mechanisms responsible for it. In the case of $d_{hole} = 500$ and 300 nm, the curves of Fig. 4.7a and Fig. 4.7b are slightly different. This difference might be because different n and k values are used for the materials. Moreover, small waves appear in the curves (especially visible for $d_{hole} = 900$ nm) which might be produced by interference at the boundaries of the unit cell or due to internal reflections within the thick glass layer. This side-by-side comparison of the transmittance gives reliable confidence in the model and the simulation code.

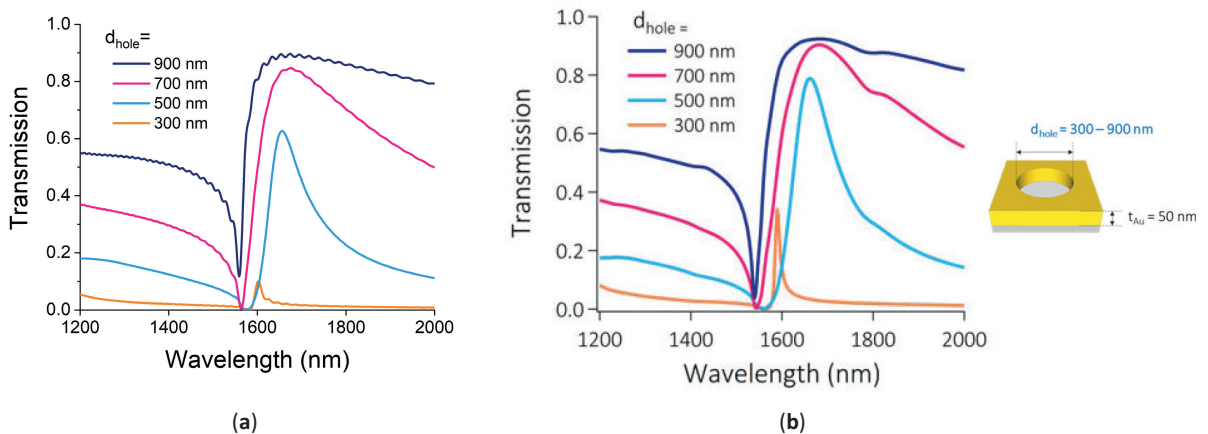


Figure 4.7: Simulated transmission spectra of Au nano-holes array as a function of nano-hole diameter. Where (a) describes the results from this work and (b) simulations based on article by Q. Tong et al.^[64]. The periodicity of the structure is 1000 nm.

Ag micro-hole array

In the second validation step, a micro-hole array produced by nanoimprint lithography is investigated. SEM images in Figure 4.6 show the resulting structures made by nanoimprint lithography. The circles ($1.9 \mu\text{m}$ in diameter) are arranged in a hexagonal pattern with a center-to-center distance of $3 \mu\text{m}$. The thickness of the film is measured on a different cross-sectional image and gives approx. 32 nm. The dashed rectangle describes the unit cell used for the FDTD simulation, it has a dimension of 3 by $5.2 \mu\text{m}$. Figure 4.8 presents the transmittance spectra of the measured and simulated samples. It can be seen that, in both cases (full coating

and structured), the simulation predicts similar transmittance in the visible spectrum as the fabricated samples. It is shown that the structuring of the silver coating can improve the transmittance of the sample by up to approx. 20% percentage points in the visible range. For wavelength above 1000 nm, the simulated data for micro-holes shows less transmission in the NIR. Two factors could explain this behaviour: (i) the silver on the nanoimprint samples oxidized during the transport which lowered its conductivity and NIR transmittance; (ii) the sample was not homogenous over the entire surface that was characterized leading to different interaction with light.

These results confirm that the model created in the simulation software closely describes the behavior of light/matter interaction on structured thin film material. The knowledge acquired during this validation process is further utilized in the next section to optimize the spectral selectivity of silver coatings.

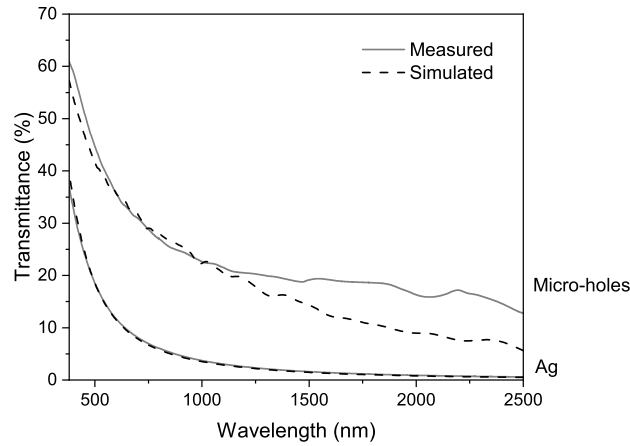


Figure 4.8: Transmittance spectra of measured and simulated 32 nm silver thin film coating compared to a micro-hole array structured film. The simulated model fits closely the measured data in the visible range and has a slightly higher transmittance in the NIR.

4.3.2 Optimization solar radiation vs emissivity

Perfect electrical conductor nanomesh

A model is first created with a single layer of a perfect electrical conductor (PEC) (infinite electrical conductivity) based on squared geometry presented in Fig. 4.3. The aim is to investigate the impact on the transmittance of each dimension of the design presented in Fig. 4.3 (linewidth, thickness and periodicity). Figure 4.9a shows the resulting transmittance when the linewidth w is varied while the periodicity and thickness are kept constant. As w increases the size of the opening in the mesh diminishes which leads to a reduction in transmittance. The most interesting aspect of this graph is the transmission maximum located around 2'000

nm: for a linewidth of 100 and 200 nm the peak is first located at exactly 2'000 nm which corresponds to the periodicity of the unit cell. Then, it moves to higher wavelengths as w increases. The 100 % transmittance peak reminds of a absentee layer founds in thin film interference and/or metamaterial cloaking. For $w = 100$ nm, high transmittance peaks can also be seen in the visible spectrum which might be due to resonance effect.

Larger openings allow higher transmittance, however the band selectivity is wider. In contrast, smaller openings allow for fewer transmission resonance modes, resulting in sharper peaks and a decrease in the transmission coefficients for wavelengths below the size of the periodicity. When w reaches 1'500 nm, the transmittance falls under 20% meaning that the opening might not be large enough for the successful transmission of light.

Figure 4.9b presents the influence of the film thickness on the transmittance. All designs exhibit a strong maximum at 100% of transmittance around 2'000 nm. As the thickness increases, this maximum shifts to higher wavelengths and the transmittance cutoff in the NIR spectrum is more pronounced.

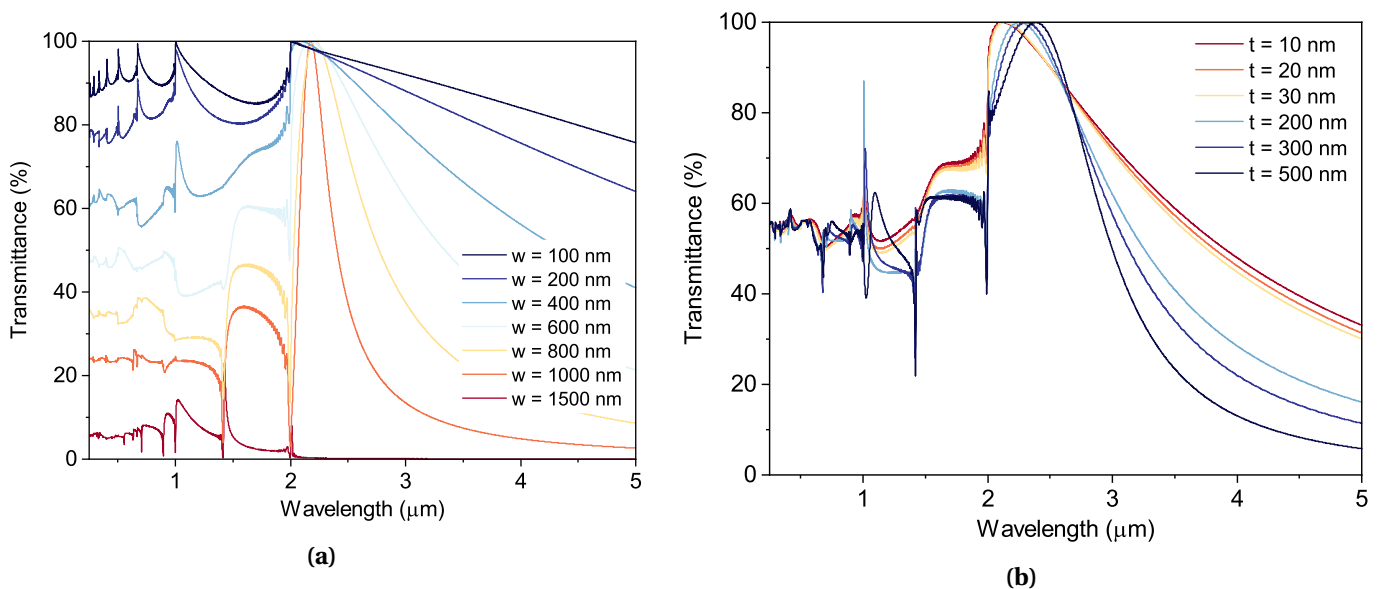


Figure 4.9: Transmittance spectra of a structured PEC mesh with a square geometry and a constant periodicity $p = 2000$ nm. (a) the linewidth w is varied from 100 to 1500 nm ($t = 35$ nm) and (b) the thickness t is swept between 10 and 500 nm ($w = 500$ nm).

Lastly, the periodicity is varied while the p/w ratio is kept at 2.5. The resulting transmittance is shown in Figure 4.10. Interestingly, the shape of the curves stays constant throughout all variations and is comparable to the transmittance of nano-hole array presented in the previous section. As the periodicity (and hence the linewidth) decreases, the maximum of the peak is blue-shifted. This striking observation means that the transmittance peak could potentially be tuned by modifying the dimension of the structure to achieve high transmittance in visible

light and strong reflectance in the NIR. This effect is further investigated in the next section.

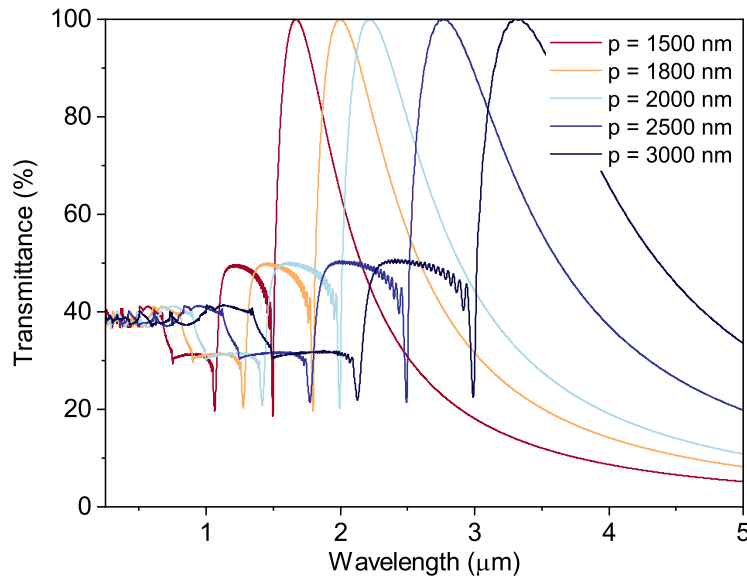


Figure 4.10: Transmittance spectra of a structured PEC mesh with a ratio $p/w = 2.5$ kept constant and a thickness of 35 nm. p is varied and w is adapted accordingly to keep the fixed ratio. The transmission peak moves according to the periodicity.

Ag nanomesh

The final design examined in this chapter consists of a structured thin Silver film placed on a glass substrate. Figure 4.11 presents the transmittance, reflectance and absorptance spectrum of a 10 nm silver coating and is in agreement with values reported in the literature^[65,66]. The graph can be divided into three parts:

- (i) below 322 nm the refractive index is high, meaning that a strong reflection occurs
- (ii) around 322 nm, both n and k coefficients are low and the transmittance depends on the skin depth: for ultra-thin silver film (10 nm) the thickness of the coating lies below the skin depth δ , meaning that part of the electromagnetic field will propagate through the metal film.
- (iii) above the plasma oscillation (natural frequency of oscillation within the metal at which free electrons and positive ions may be thought of as plasma) which, for Ag, is located at 322 nm (3.85 eV)^[67], the coefficient k is raising drastically leading to an increase in reflection.

The skin depth is defined according to the equation of conductivity^[68]:

$$\delta = \sqrt{\frac{2}{\sigma_{Ag}\omega\mu_0}} \tag{4.10}$$

in which the conductivity of Ag is $\sigma_{Ag} = 6.30 \times 10^7 \text{ S/m}$, μ_0 the permeability of free space and ω angular frequency of current ($\omega = 2\pi c/\lambda$). The resulting skin depth in bulk Ag is plotted in Figure 4.12.

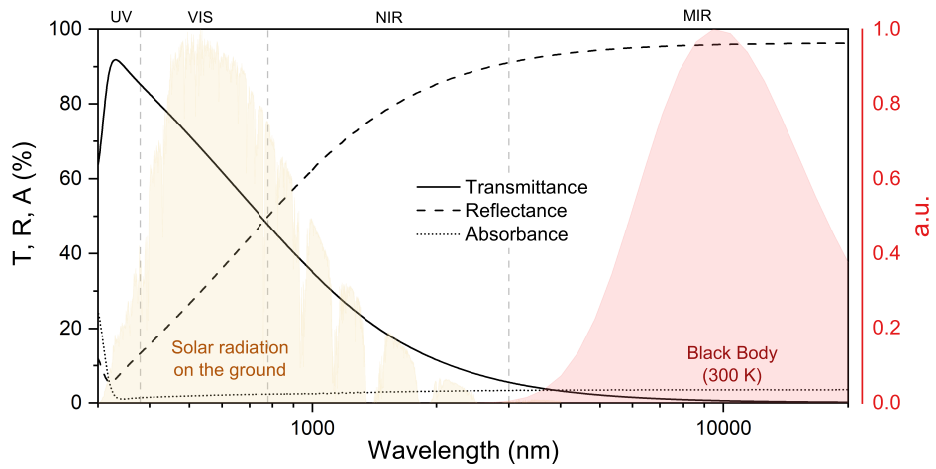


Figure 4.11: Transmittance, reflectance and absorbance spectra of a 10 nm Ag coating.

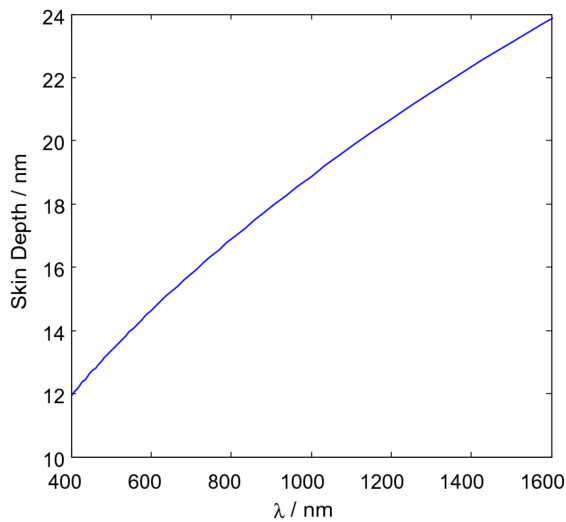


Figure 4.12: The skin depth of bulk Ag for varying wavelengths of incident light.

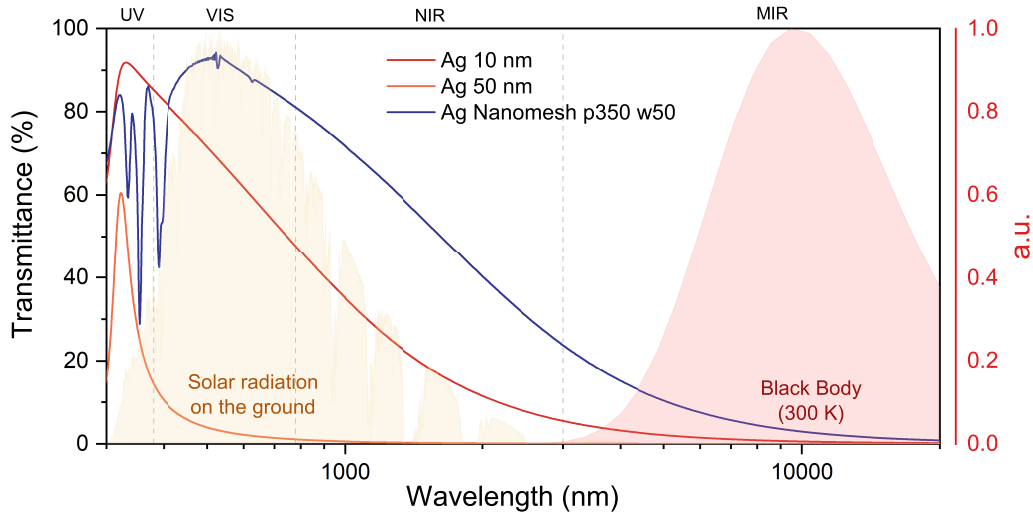


Figure 4.13: Transmittance spectra of two Ag coatings with thicknesses of 10 and 50 nm and a nanomesh structured Ag film with $p = 350$ nm, $w = 50$ nm and $t = 50$ nm. The structured coating shows high transmittance in the visible range and decreases significantly in the MIR region. Both, the global solar irradiance at 1.5 AM and the blackbody radiation are normalized between 0 and 1 and expressed in arbitrary unit (a.u.) as reference.

As shown in Figure 4.13, two different thicknesses of ultrathin Ag film (10 and 50 nm) are compared to a nano-structured 50 nm thick coating. Because of the larger thickness in the 50 nm thin film, the transmittance is smaller and the cutoff above the plasma oscillation is more defined. The optimized nanomesh design shown in blue has a periodicity, linewidth and thickness of, respectively, 350, 50 and 50 nm. The linewidth to thickness ratio is kept at 1:1 because of manufacturing limitations. It can be seen that the nanomesh exhibits high transmittance in the visible spectrum which then significantly decreases in the MIR range. As mentioned before the periodicity of the mesh plays an important role in explaining the transmission peak around 540 nm. Above this distance, the wavelength of the EM waves become too large to be transmitted through the mesh structure and are mostly reflected. This means that the MIR radiation of a blackbody at room temperature (300K) are reflected, leading to a low emissivity.

More complex interactions are taking place below 540 nm. Full-wave simulations allow to visualize locally the E-field distributions and can help understanding the behavior of the light when the size of the structure and the wavelengths become closer. Figure 4.14 shows the E-field distribution at wavelengths of 363 and 540 nm. At 363 nm, the light is strongly attenuated with a dip in transmittance. This effect reminds of coupled surface plasmon resonance occurring on the surface of the mesh grid. It can be seen clearly in the cross-section image (see Fig. 4.14c) where the electric field increases to more than 13 V/m and shows bright resonance effects on the surface of the film. In contrast, at 540 nm, the EM wave interacts lightly with

Table 4.1: Visible, solar transmittance and emissivity. The value for single glazing are taken from AGC^[11].

Design	T_v [%]	T_e [%]	ϵ [%]	T_e/ϵ
10 nm Ag	65.8	53.2	3.5	15.2
50 nm Ag	2.9	3.1	1	3.1
Ag nanomesh	91.1	78.7	4.7	16.7
Ag nanomesh - 4%	87.1	74.7	4.7	15.9
Single glazing with low-e	84	54	~ 3.5	15.4

the mesh but does not exceed 3.4 V/m. Moreover, the distribution of the E-field inside the opening is more homogeneous (see Fig. 4.14b).

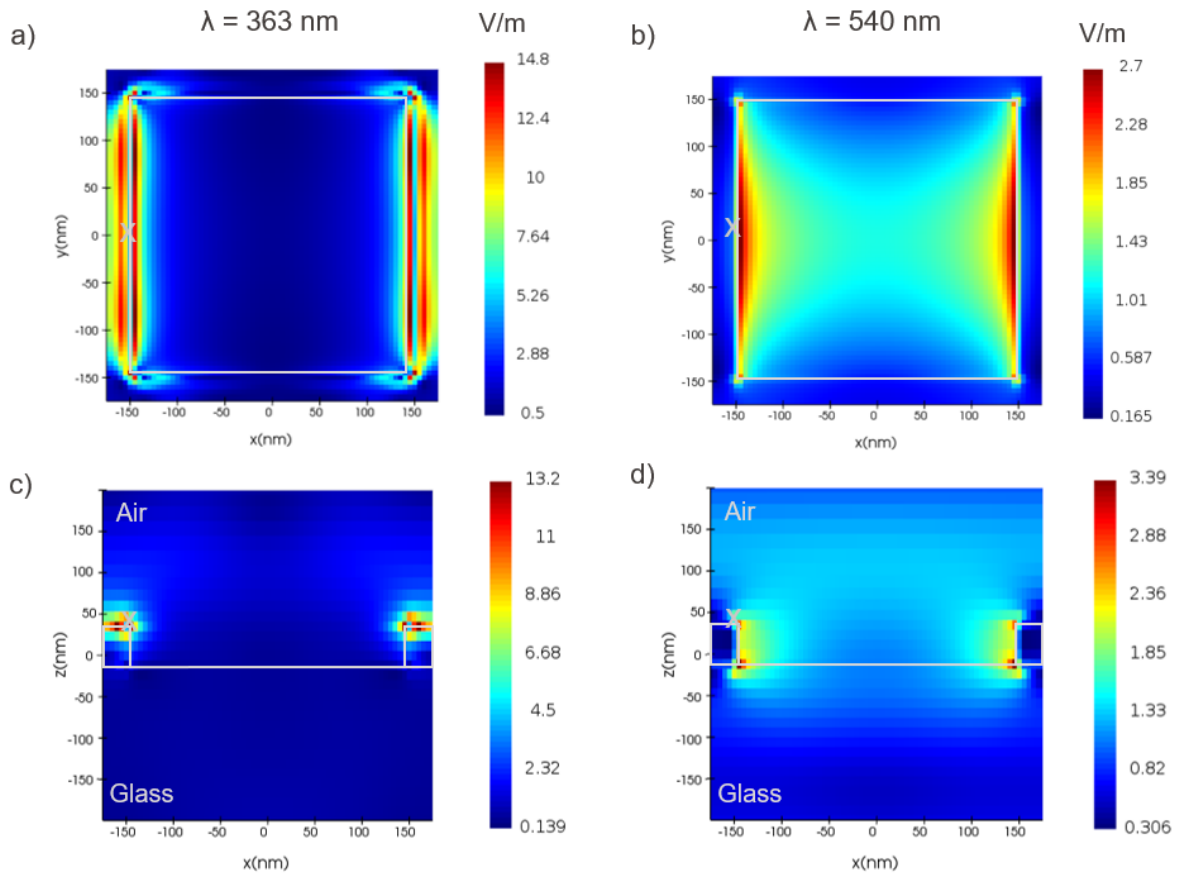


Figure 4.14: (a,b) Top-view and (c,d) cross-section of the electric field distribution in V/m through the mesh at a wavelength of 363 and 540 nm. The edges of the Ag structure are drawn in white lines. The white crosses indicates the location of the monitor compared to each other.

As presented in Table 4.1, the selective behaviour of the nanomesh results in excellent visible

and solar transmittance while achieving low emissivity at room temperature. As mentioned by A. Faist^[12], a ratio U-value/SHGC allows to evaluate the thermal quality of a glazing: this quality improves when the ratio decreases. In the case of these simulation, the factor ϵ plays a role in the determination of the U-value and T_e of the SHGC. Hence, the ratio T_e/ϵ should be as high as possible to improve the thermal quality of a glazing.

It should be noted that the low-e coating used in the single glazing consists of a silver thin film combined with additional anti-reflective layer systems which increases the visible and solar transmittance. Finally, to equally compare the low-e with the simulation an additional 4% reflection due to the second glass/air interface (which is not simulated) should be subtracted from the transmittance. Overall, the optimized nanomesh achieves a slightly improved visible transmittance and an increase of around 20% percentage points in solar transmittance compared to conventional low-e coating while maintaining low emissivity.

4.4 Conclusion

In this chapter, the potential of improving the spectral selectivity of thin film by 2D structuring has been investigated. A numerical model is used to simulate the interaction of an incident beam of light on a thin metal coating. The amount of light passing through the film is then monitored by measuring the E-field distributions, which, in turn, gives the transmittance. The model is first validated by comparing it to other simulations found in the literature and through the fabrication and characterization of nanoimprint micro-holes samples. It is then used to optimize the size of silver meshes to achieve high transmittance in the visible range and strong reflectance in the MIR (low-e). It is found that a mesh size of $p = 350$ and $w = 50$ nm gives outstanding properties and represents a good candidate to achieve high solar heat gain in low-e coatings. This study opens the pathway to the future production of nano-structured samples using, for example, e-beam lithography in a clean room to achieve the required definition in the nano-scale and validate the model presented in this chapter.

EC WINDOWS WITH ADAPTABLE **PART III**
SELECTIVITY

5 ELECTROCHROMIC DEVICE WITH HIERARCHICAL METAL MESH ELECTRODES

This chapter is based on the submitted journal paper:

Fleury, J., Burnier, L., Lagier M., Shukla S., Manwani K., Panda E. and Schüler, A., 2022. Electrochromic device with hierarchical metal mesh electrodes: transmittance switching in the full spectral range of solar radiation, Submitted to *Solar Energy Materials and Solar Cells*

Author contribution for the journal paper:

In this article, JF designed the research with the support of all co-authors. JF conducted the following tasks: methodology, formal analysis, investigation, data curation. writing—original draft preparation, writing—review/editing and visualization.

Within this chapter, hierarchical metal mesh structures are fabricated for use as transparent conductive electrodes in electrochromic devices with large-band transmittance switching. Electrochromic materials (WO_3 and Ta:NiO) are deposited by plasma sputtering on the metal mesh and characterized in a custom-made electrochemical setup allowing in-situ photo-spectrometer measurement. Electrochromic devices based on the WO_3 cathode and Ta:NiO anode combined with the hierarchical metal mesh are fabricated. The resulting device achieves remarkable optical modulation in the full spectral range of solar radiation compared to conventional ITO-based devices. This study paves the way for development of hierarchical metal mesh-based electrochromic devices which offer high potential for energy savings through wide band modulation of solar heat gain in buildings in countries with warm and cold seasons.

5.1 Introduction

Space heating in European countries such as Switzerland corresponds to a share of around one-third of the total energy consumption^[69]. To reduce energy loss, the use of insulating

glazing belongs to the state of the art in modern as well as retrofit buildings. These windows achieve high insulation properties by combining multiple glass panes with one or several low-emissivity (low-e) coatings. Low-e coatings are transparent in the visible (VIS) range and act as reflectors in the mid-infrared (MIR) range, which reduces energy loss through thermal radiation^[17,70]. Due to the coating, solar heat transmitted into buildings is also greatly reduced which could be desirable in countries with hot, stable climates. However, in countries with distinctive seasons, a more precise control of the transmittance through window glazing is desirable. This could be achieved by implementing smart windows with switchable electrochromic (EC) glazing^[71,72]. EC materials can modulate their optical properties in the visible and near-IR (NIR) ranges upon application of an electrical voltage. The heating/cooling and lighting energy loads of a building could thus be reduced significantly by optimizing the amount of light entering the building, depending on external weather. Several studies investigated the modulation of electrochromic devices (ECD) in the near-infrared and infrared region of the spectrum and present promising results^[73–81].

Nowadays, EC glazings are conventionally produced by utilizing indium tin oxide (ITO) as a transparent conductive film (TCF) for electrodes. However, ITO presents a few shortcomings: it is brittle, has limited electrical conductivity and shows degradation upon cyclic operation^[82]. Moreover, its scarcity and high demand are making ITO increasingly expensive^[21]. Because of its plasma frequency located around 1300 nm, ITO coatings also reduce transmittance in the NIR spectrum^[22]. Knowing that 50% of the solar heat radiation is delivered in the NIR spectrum^[23], ITO coatings present significantly lower energy saving potential in the winter period. Metal meshes are promising candidates to substitute ITO because they exhibit high transmittance in the visible and NIR spectrum, and have excellent conductivity and mechanical flexibility. What is more, unlike conventional TCF, the thickness of the metal mesh can be increased to improve its conductivity without reducing its transparency. A literature review of various structures and materials used as metal meshes are presented in Table 5.1. A figure of merit proposed by Haacke^[83] is used to compare the different transparent conductive films:

$$\phi_H = \frac{T_{550nm}^H}{R_s} [10^{-3} \Omega^{-1}] \quad (5.1)$$

where $H = 10$ is the exponent proposed by Haacke (which stipulates that the maximum ϕ_H should be optimized for a 90% optical transmission) and T_{550nm} is the visible transmittance at 550 nm.

It can be seen that, so far, the highest figure of merit has been achieved by a hierarchical structure composed of a nano- and micromesh^[84].

In this study, a hierarchical structure composed of a platinum metal mesh and an ultra-thin tungsten film is used to improve the NIR transmittance and electrical properties of a $WO_3 / Ta:NiO$ ECD. The electrochromic properties are investigated through cyclic voltammetry (CV) and chronoamperometry (CA) while performing an in-situ characterization of the transmittance with a UV-VIS-NIR spectrometer.

Table 5.1: Literature review of transparent conductive films and their physical properties.

ϕ_H ($10^{-3}\Omega^{-1}$)	Mesh design	Material	Periodicity (μm)	Line width (μm)	Thickness (nm)	T_{550nm} (%)	R_s (Ω/\square)	Ref.
221	Hole / hexagon ^a	Ag	2 / 500	0.1 / 10	0.03 / 1	83	0.7	[84]
109	Square grid	Ag	50	0.607	2000	96.3	6.3	[85]
60.5	Hexagon	Cu + AZO	30	1	62	90.6	6.2	[86]
46.5	Square grid	Ag	10	1	600	84.3	3.9	[87]
43.7	Film ^b	ITO	-	-	300	85	4.5	[88]
12.4	Square grid	Ag	300	15	2000	~ 78	20	[89]
8.9	Hole	Cu	10	1.2	19	83	17.5	[90]
7.8	Hole	Ag	10	0.1	300	83	20	[91]
5.6	Hole	Ag	0.590	0.177	20	85	35	[92]
3.8	Square grid	Cu / Ti	0.7	0.07	40 / 2	78	22	[93]
2.1	Square grid	Cu / Ag	7	0.5	100	> 80	< 50	[94]
0.8	Hole	Pt	0.08	0.03	30	75.2	71	[95]
0.4	Nanowire	Ag	-	-	100	65	36	[22]

^a hierarchical structure composed of a nano- and micromesh, ^b Commercially available

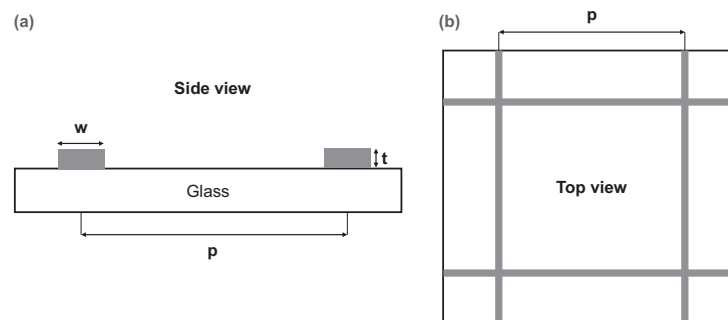


Figure 5.1: (a) Schematic cross-section and (b) top view of a metal mesh with w being the width of each deposited line, t the thickness and p the periodicity of one unit cell.

5.2 Methodology

This section presents the steps that were carried out to (i) produce and characterize transparent mesh electrodes; and (ii) fabricate ECDs and analyze them.

5.2.1 Manufacturing of transparent mesh electrodes

UV-photolithography is used for the origination of the metal structure. The chosen metal mesh design is presented in Fig. 5.1 and the process used to produce these structures is outlined in Fig. 5.2. Before starting the process, 500 μm thick 4" soda-lime glass wafers are cleaned in a Piranha (a solution made of a 3:1 mixture of concentrated sulfuric acid (H_2SO_4) with hydrogen peroxide (H_2O_2)) for 2 x 5 min at 100 °C. A Süss ACS200 GEN3 modular cluster tool is then used

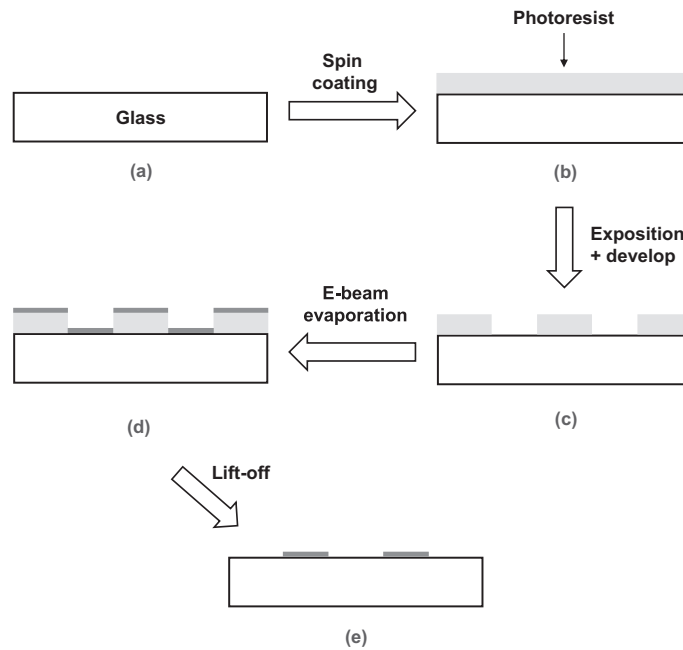


Figure 5.2: Step-by-step outline of the process to produce transparent mesh electrodes using UV-photolithography. The substrate (a), consisting of soda-lime glass, and is spin-coated with a negative photoresist (b). The sample is locally exposed to a UV-laser to harden the photoresist. This is followed by the removal of non-exposed resist (c). A thin metal film is then evaporated over the sample (d) and, finally, the remaining photoresist is lifted-off in a chemical bath to produce the mesh structure (e).

to spin coat the negative photoresist AZ® nLOF 2020 and to develop the wafer after exposition (Fig. 5.2b and c). The UV exposure is carried out by Direct laser writing at a wavelength of 375 nm with a Mask-Less Aligner (MLA150) developed by Heidelberg Instruments GmbH. Right after development, a O₂ high frequency plasma (Tepla 300) is used for 10 sec at 200 W to clean any residues. Once the wafer is cleaned, metal films are deposited by e-beam evaporation through a Leybold Optics LAB 600H (Fig. 5.2d). The deposition consists of an adhesion layer of 10 nm Titanium (Ti) followed by Silver (Ag), Platinum (Pt) or Aluminum (Al). Finally, the photoresist is lifted-off in a bath of MICROPOSIT™ Remover 1165, leading to the desired mesh structure on the glass wafer (Fig. 5.2e).

The desired hierarchical structure is achieved by depositing a conductive thin film onto the micrometric metal mesh. Two configurations are compared in this work: a tungsten and a niobium-doped anatase TiO₂ (NTO) thin film. NTO is deposited using a Nb₂O₅:TiO₂ compound target (6 at% Nb, purity: 99.99%). The deposited NTO film is then post-annealed at 823 K for 1 hr (with a heating rate of 3 K/min) in a vacuum (at a pressure of 2.2×10^{-6} mbar)^[96]. Deposition parameters for both films are depicted in Table 6.1.

Table 5.2: Deposition parameters plasma sputtering: the working pressure in the range of 10^{-2} mbar allowed for the growth of a nanoporous coating which is beneficial for ions permeability in ECDs.

Coating	W	WO ₃	Ta:NiO	NTO
Target	W		Ni _{0.91} Ta _{0.09}	Nb ₂ O ₅ :TiO ₂
Applied power	Direct Current		DC-pulsed	RF
Power / W	150	100	120	60
Frequency	-	-	250 kHz	13.56 MHz
Pulse width / ns	-	-	496	-
Deposition time	10 sec	140 min	180 min	180 min
Thickness / nm	6	200	175	126
Ar / sccm	28	18	62.5	50
O ₂ / sccm	-	6	2	-
Ratio O ₂ /Ar	-	33 %	3.2 %	-
Pressure / 10^{-2} mbar	0.43	4.1	1.7	1.25

5.2.2 Electrical and optical characterization

The experimental sheet resistance is determined by surface resistivity measurements^[97]. The configuration for metal meshes consists of two equal-sized electrodes in close contact with the mesh on each side of a square sample (the distance between the electrodes has to be equal to the width of the sample). This configuration ensures for macroscopic sheet resistance, which means that the size of the square is larger than the periodicity of the mesh. The transmittance is measured using an ultraviolet - visible - near-infrared spectrophotometer (Agilent Cary 5000) in the wavelength range of 200 - 2500 nm, combined with an integrated sphere to measure the total and diffuse transmittance. This allows to calculate haze, which is equal to diffuse over total transmittance.

5.2.3 Preparation electrochromic layers

The anode (Ta:NiO) and the cathode (WO₃) are deposited using reactive plasma sputtering in a sputter-up configuration of the following targets: tungsten (Kurt J Lesker 99.95 % purity) and nickel-tantalum (Ni-Ta 91-9 at%) with a diameter of 50.8 mm (2"). The deposition parameters are presented in Table 6.1. As previously shown^[19,98], working pressure in the range of 10^{-2} mbar is beneficial for ions permeability in ECDs. The EC-layers are deposited on transparent metal meshes and ITO-coated glass from Delta Technologies (X174, X190, X307). The samples are masked with square apertures of 14.5 x 14.5 mm to define a fixed area for electrochemical experiments. The coatings are simultaneously deposited on a single-side polished Si (100) substrate. This allows to monitor the thickness through a cross-section image, as analyzed by scanning electron microscopy (SEM, Zeiss GeminiSEM 300). Finally, the porosity is verified using spectroscopic ellipsometry by comparing the refractive index of the deposited film to that of the bulk material.^[99–102]

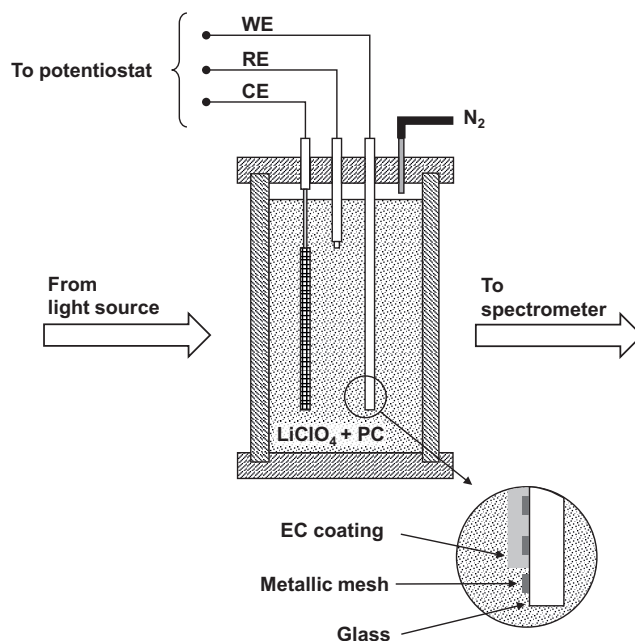


Figure 5.3: Electrochemical setup designed for optical characterization of EC half devices. The experiment consists of three electrodes: a platinum mesh counter electrode (CE), a non-aqueous Ag/Ag⁺ reference electrode (RE) and a glass coated with a transparent conductive film and WO₃ or Ta:NiO as a working electrode (WE). The electrolyte is kept under an inert environment during the characterization through a constant flow of nitrogen within the cell.

5.2.4 Electrochemical experiments

As shown in Fig. 5.3, a custom-made data acquisition setup was built to simultaneously monitor the electrochromic and optical properties of the EC coatings. Electrochemical lithiation consists of a three-electrode cell containing a liquid electrolyte, 1M lithium perchlorate in propylene carbonate (LiClO₄-PC), and connected to a Bio-Logic SP-200 potentiostat/galvanostat (accuracy less than 0.5 %). A platinum mesh counter electrode is chosen for its large high surface area, good electrical conductivity, and robustness. For a non-aqueous electrochemical experiment, reference electrodes containing water and chloride are problematic^[103]. For this reason, a non-aqueous silver-silver ion (Ag/Ag⁺) reference electrode is preferred. This reference is immersed in a solution of 0.01M AgNO₃ and 0.1M Tetrabutyl ammonium perchlorate (TBAP) in acetonitrile^[104]. This leads to a potential of 0.54 V, as opposed to that of a normal hydrogen electrode in water (NHE)^[105–107]. Because of possible oxidation of the films during the electrochemical lithiation^[108], the electrolyte is first deoxygenated with nitrogen bubbles for 30 min and then kept in an over-pressured inert environment during characterization through a constant flow of nitrogen within the cell. The transmittance is measured in-situ every two seconds using a UV/VIS/NIR Zeiss diode array spectrometer (MCS 601 and 611)

which analyses the electromagnetic spectrum from 380 to 2100 nm with a accuracy of $\pm 1\%$ [109,110]. Because of strong absorption peaks from propylene carbonate above 1600 nm, the range is limited from 380 to 1600 nm for data acquisition herein. It should be noted that for this measurement setup, the reference was taken through the electrolyte and the platinum counter-electrode, meaning that the resulting transmittance of the sample is overestimated by at least 8% (reflection of two interfaces air-glass).

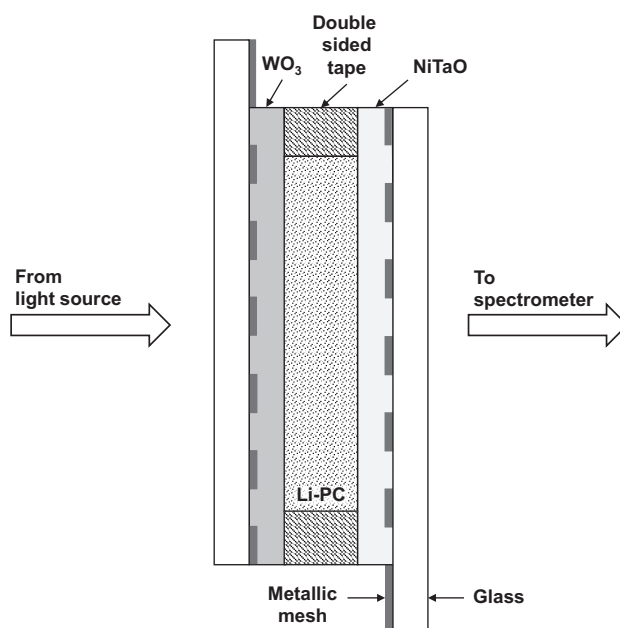


Figure 5.4: Electrochemical setup designed for optical characterization of full devices. The cathode and the anode are glue together with a pre-cut, squared, 0.25 mm thick double sided tape.

This is not the case for the fully functional ECD presented in Fig.5.4. This setup with a 0.25 mm thin electrolyte allows for characterization over the entire solar spectral range. Solar transmittance is usually determined over the full solar range from 250 to 2500 nm. As the maximal range of the spectrometer is 2100 nm, it accounts for 97% of the total solar spectrum, meaning that an error of about 3% should be accounted for.

Cyclic voltammetry (CV) experiments are carried out with four scan rates (10, 20, 50 and 100 mV/s) starting at the open circuit potential and applying a voltage between the working and the reference electrode. The current, and thus the ion intercalation, is measured and gives a "fingerprint" of the electrochemical processes. Chronoamperometry (CA) characterizations are conducted and give useful information about the switching speed, durability, charge density and inserted ions for a given voltage sweep.

5.3 Results & Discussion

This section is divided into three parts. First, the conductive transparent meshes will be compared to conventional ITO films. Then, electrochromic coatings are deposited on top of the conductive layer to create a WO_3 cathode and a Ta:NiO anode which are characterized as individual half devices in the electrolyte. Finally, the two electrodes are combined to work as a fully switchable ECD.

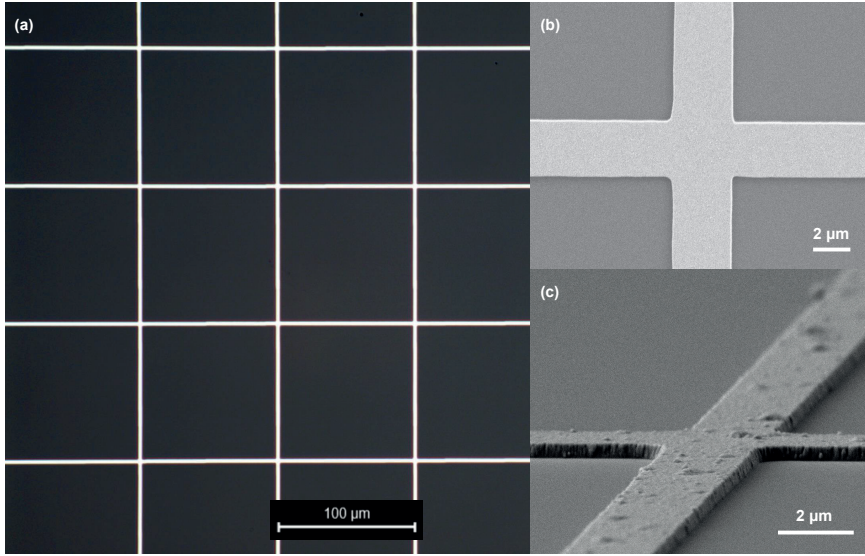


Figure 5.5: (a) Microscope and (b, c) SEM images of a metal mesh with a periodicity (p) of 100 μm , a line width (w) of 2 μm and a thickness (t) of 300 nm

5.3.1 Transparent conductive film

Figure 5.5 provides visual details of the metal mesh through microscope and SEM images. The resulting structures are well-defined and correspond accurately to the design presented in Fig. 5.1. Based on this Figure, τ (the aperture parameter) can be determined as $\tau = 1 - \frac{w}{p}$. The theoretical transmittance of the metal mesh can then be approximated by Eq. 5.2.

$$T_{\text{mesh}} = \frac{(\tau p)^2}{p^2} = \tau^2 \quad (5.2)$$

In addition to the metal mesh, the glass substrate which will reflect some light due to Fresnel losses at the air/glass interface should also be taken into account. This reflection can be calculated using Eq. 5.3^[111].

$$R = \frac{(n_{\text{glass}} - n_{\text{air}})^2}{(n_{\text{glass}} + n_{\text{air}})^2} \quad (5.3)$$

Table 5.3: Optical and electrical properties of transparent conductive films. All metal meshes have an identical aperture parameter τ of 0.98.

Sample name	Material	w (μm)	p (μm)	Thickness (nm)	T_v (%)	T_e (%)	$R'_{s,cal}$ (Ω/\square)	$R'_{s,exp}$ (Ω/\square)	ϕ_H ($10^{-3}\Omega^{-1}$)	Haze (%)
Ref	Soda-lime glass	-	-	-	91.4	90.7	-	-	-	0.2
ITO10	ITO	-	-	120-160 ^a	80	73.8	9-15 ^a	10.7	10	-
ITO20	ITO	-	-	60-100 ^a	73.6	73.7	15-30 ^a	20.8	2.2	-
ITO47	ITO	-	-	30-60 ^a	78.9	77.7	30-60 ^a	47.5	2	-
NTO	Nb ₂ O ₅ :TiO ₂	-	-	126	63.8	65.9	-	382	0.03	-
W	W	-	-	6	86.3	86.8	-	2400	0.1	-
Pt-4-200	Pt	4	200	300	86.9	86.2	17.7	25.9	9.5	1
Pt-2-100	Pt	2	100	300	86.9	86.3	17.7	24.6	10	2.2
Al-2-100	Al	2	100	400	86.5	85.9	3.4	4	58.6	2.2
Ag-10-500	Ag	10	500	400	86.9	86.3	2	2.6	94.5	0.6

^a Data provided by the manufacturer.

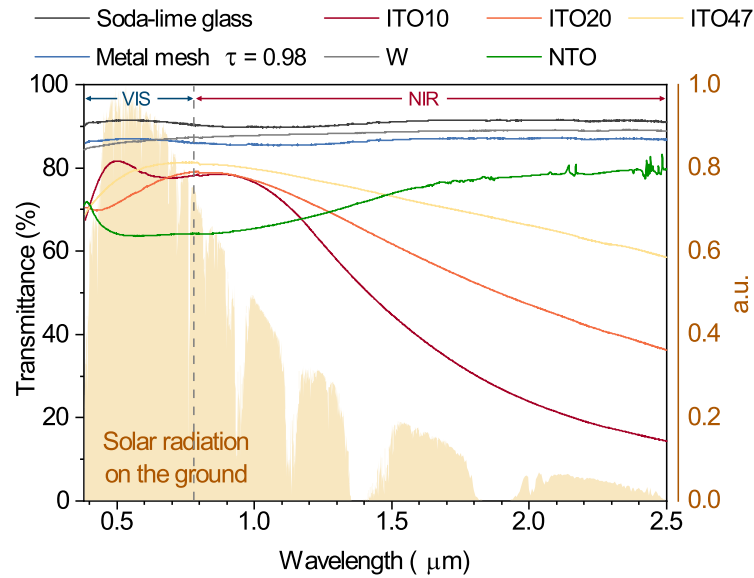


Figure 5.6: Total transmittance spectra comparing various transparent conductive films. All metal meshes have the same aperture parameter of $\tau = 0.98$ and are grouped under the blue line. The solar radiation on the ground is plotted in arbitrary units as reference. The metal meshes produce a spectrally flat transmittance in the full spectral range of solar radiation.

Taking $n_{glass}=1.52$ for soda-lime-silica glass^[112], the reflectance is close to 4% per interface. The absorbance of the 0.5 mm glass substrate is added and the resulting transmittance at 550 nm is 91.3%^[60]. A theoretical approximation of the total transmittance through the samples can thus be made:

$$T = 0.913 \tau^2 \quad (5.4)$$

With an aperture parameter of $\tau = 0.98$, Eq. 5.4 gives a value of 87.7 %. This result is marginally higher than the experimental visible transmittance of ~ 86.9 presented in Table 5.3 for the metal mesh. However, it stays within the ± 1 % experimental error of the spectrometer.

Table 5.3 also compares the electrical properties of the various TCFs presented in this study. The sheet resistance R_s of homogeneous metal films is calculated with Eq. 5.5, where σ is the bulk conductivity and t the thickness of the film.

$$R_s = \frac{1}{\sigma t} \quad (5.5)$$

As shown for Ag^[113], Al^[114] and Pt^[115], the conductivity of thin metal film remains similar to the bulk for thicknesses above 150 nm. The sheet resistance of a squared mesh metal film $R'_{s,cal}$ can thus be calculated by Eq. 5.6^[116]:

$$R'_{s,cal} \approx \frac{1}{1 - \tau} R_s \quad (5.6)$$

What stands out in table 5.3 is that the figure of merit of the metal meshes exceeds that of the most effective ITO coating by nearly a factor of ten. It should be noted that, in the case of the metal mesh, only a small fraction of the surface is covered by the conductive material. This means that locally (on a microscopic scale), the conductivity will be non-existent. Depending on the application this could be compensated by the fact that the contacted material is itself slightly conductive (i.e. semiconductor) and is enough for the device to work properly. One way to overcome this issue is to combine an ultra-thin conductive layer under or over the metal mesh, creating a hierarchical structure to help transfer the electrons through the last few micrometers. A comparable design was proposed by Gao et al.^[84] (see Table 5.1) which combines a nano and micro-structure to increase the overall conductivity and reaches an impressive figure of merit of 221. In this work, an ultra-thin conductive layer of Tungsten (W) and a thin film of NTO are combined to create a hierarchical structure and to improve the interface compatibility between the mesh and the EC coating.

As can be seen in Figure 5.6, the transmittance of the metal meshes is constant and spectrally flat over the full spectral range of solar radiation. In contrast to this, the transmittance of ITO-coated glass decreases significantly for wavelengths above 1100 nm. This attenuation is stronger for ITO coatings with lower sheet resistance. This cut-off in the NIR is likely due to the excitation of electrons into a higher energy level within the same band (intraband transition). This occurs for incident EM radiation above the plasma wavelength λ_p ^[117]. In the case of ITO, the plasma resonance wavelength is located around 1300 nm (depending on the doping level)^[118] which means that EM radiation above this wavelength is either reflected or absorbed. An NTO film is selected because of its larger dielectric constant which results in a red-shift of λ_p and thus restores transparency in the NIR region^[119]. However, the high transmittance in the VIS and NIR range of the metal meshes makes them more suited for modulating the NIR light in an EC setup.

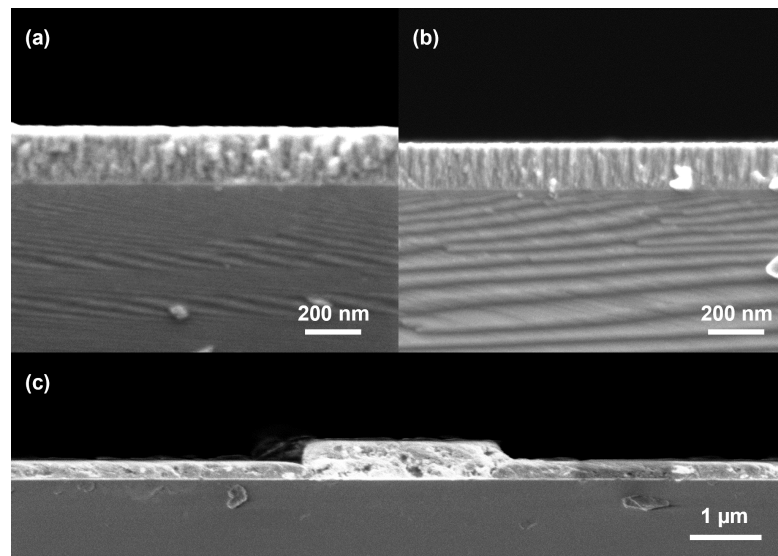


Figure 5.8: Cross-section SEM images of (a,c) WO_3 and (b) Ta:NiO on silicon displaying a thickness of, respectively, 200 and 175 nm. (c) Pt-2-100 metal mesh with WO_3 layer focusing on the metal/semiconductor interface.

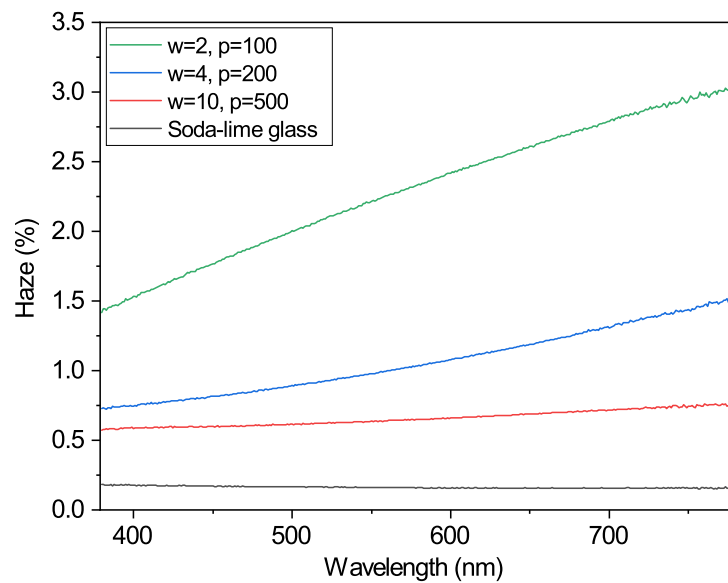


Figure 5.7: Haze factor compared for various sizes of the metal mesh in the visible spectral range: the smaller the structure, the more it diffracts light and thus haze is produced.

It is worth mentioning that, unlike homogenous thin film, the use of a metal grid pattern can potentially lead to light diffraction, creating a negative haze effect through the glass. This concern was assessed by measuring the diffuse transmittance in an integrating sphere and

dividing it by the total transmittance, leading to the haze factor. As shown in Fig. 5.7, the haze increases as the size of the mesh decreases and is stronger for higher wavelengths. A possible explanation for this might be that the dimensions of the metal mesh are of a similar magnitude to the wavelength of the incident light, leading to diffraction and scattering effects. The haze is especially noticeable for the 2 μm wide lines but stays around 2.5 % on average - which is within the acceptable limit in large-scale production (2 % to 5 %^[120]). The patterning of coating could also leading to an appearance of interference color effects. The latter appears often in periodic micro-structured surfaces. In the case of metal mesh with a width of 2 μm this effect was not observed.

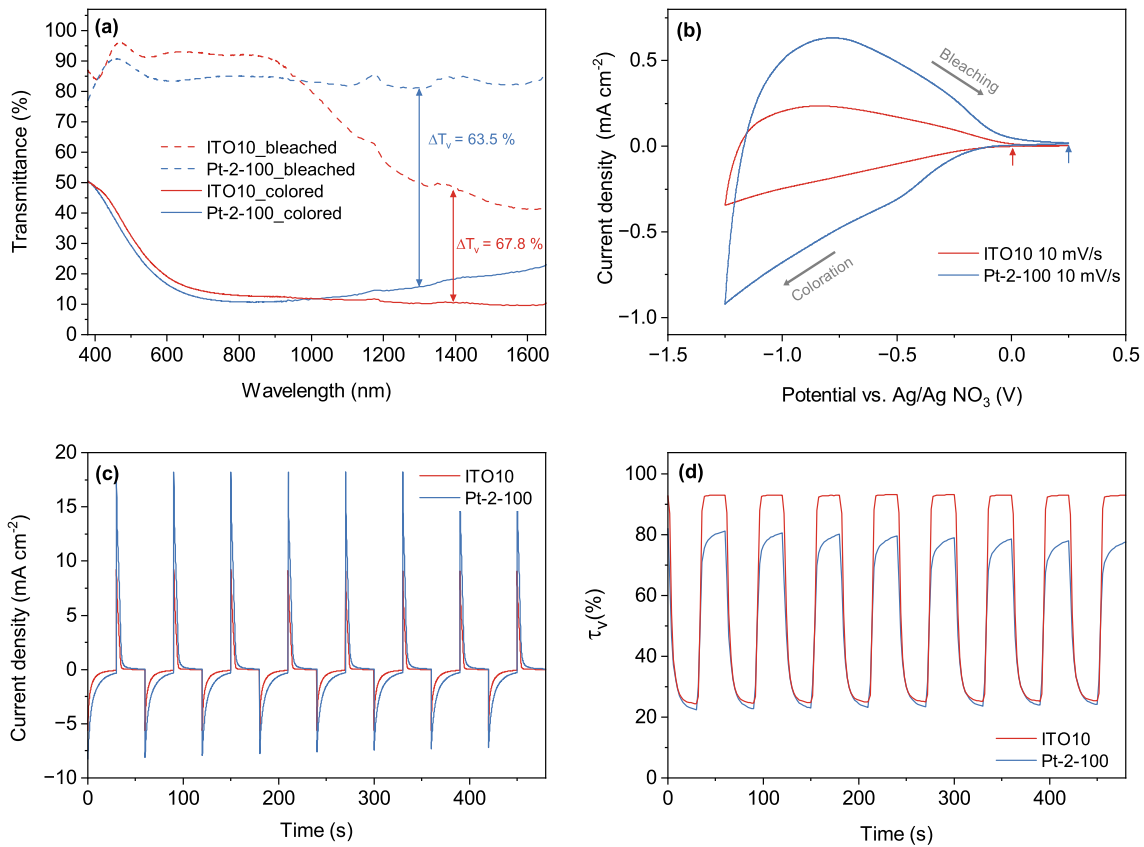


Figure 5.9: Electrochromic properties of the WO_3 cathode in Li-PC measured at -1.25/+0.25 V (vs Ag/Ag^+) comparing ITO and the metal mesh: (a) Transmittance spectra in colored and bleached taken from CA measurements. (b) Cyclic voltammograms at a scan rate of 10 mV/s where the vertical arrows give the open circuit voltage at which the scan started/ended. (c) Chronoamperometry curves for 8 cycles of 30 s and (d) its resulting in situ visible transmittance. Pt-2-100 achieves outstanding transmittance modulation in the NIR spectrum.

5.3.2 Cathode & anode characterization

As presented in Table 5.3, the highest figure of merit for ITO samples is 10, which is comparable to the value achieved by platinum meshes. For that reason, the samples ITO10 and Pt-2-100 which have a similar figure of merit are chosen to further investigate TCF in ECDs. As shown in a previous study^[121], a metal film in contact with WO₃ could oxidize and drastically reduce electrical conductivity. A thin barrier layer of tungsten is shown to protect the film from oxidation. In this work, an intermediate layer with a nominal thickness of 6 nm W is added between the metal mesh and the EC-coating. This ultra-thin layer is thought to improve the electrical and electrochromic performances without significantly reducing the transmittance in the VIS and NIR range (see Fig. 5.6). The W inter-layer could play a role in modifying the interface from a Schottky (rectifying behavior) to an ohmic contact which greatly facilitates the switching reversibility in ECDs. As shown in Table 5.3, the ultra-thin W layer has a sheet resistance of $R'_s \approx 2400 \Omega/\text{sq}$ which is slightly lower than the sheet resistance of a 160 nm thick WO₃ coating ($R'_s \approx 5000 \Omega/\text{sq}$)^[122]. The same tungsten thin film is applied on the ITO10 sample for the WO₃ cathode.

The samples are characterized by SEM, as depicted in Fig. 5.8. The thickness of the films can be measured in Fig. 5.8a for WO₃ and Fig. 5.8b for Ta:NiO and give, respectively, 200 and 175 nm. Fig. 5.8c shows a cross-section image where the Pt mesh and the WO₃ coating are superposed. The WO₃ film covers the entirety of the mesh and creates a well-formed interface between the metal and the semiconductor. It can also be seen that a columnar and porous coating is produced. It is typically formed at higher pressures using plasma sputtering and is desirable for electrochromic application^[98,123].

The porosity p of both films can be calculated by using the refractive indices from ellipsometry measurement and the Lorentz-Lorenz effective medium approximation (EMA)^[124]:

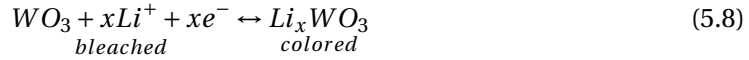
$$p = 1 - P = 1 - \left(\frac{n_f^2 - 1}{n_f^2 + 2} \right) \left(\frac{n_b^2 + 2}{n_b^2 - 1} \right) \quad (5.7)$$

with P being the packing density, n_f and n_b the refractive indices of the films and of bulk, respectively, $n_f=1.93$ and $n_b=2.5$ ^[101] for WO₃ and $n_f=2.05$ and $n_b=2.18$ for NiO^[125]. Using Eq.5.7 results in a porosity of 25.4 % for WO₃ which corroborates the findings of a previous work^[19] and 7.1 % for Ta:NiO.

The electrochemical characterization of the individual WO₃ cathode and Ta:NiO anode is done using the setup shown in Fig. 5.3. The transmittance (bleached and colored) of WO₃ deposited on ITO10 and Pt-2-100 is compared in Fig. 5.9a. In the bleached state, the transmittance change in NIR is more pronounced for the metal mesh where the modulation of ΔT_{1300nm} is 65.4% compared to 38.8 % for ITO. In the colored state, both samples show a strong absorption band centered around 1000 nm, which is mostly likely associated with the reduction of W⁶⁺ to W⁵⁺^[98,126]. A transmittance peak can also be seen in the blue range, a characteristic specific

to WO₃ thin films^[127].

A voltammogram at a scan rate of 10 mV/s is depicted in Fig. 5.9b. It shows that, as the voltage decreases from 0.25 V (vs Ag/Ag⁺), the current remains close to zero until the voltage drops below -0.25 V (vs Ag/Ag⁺). At this point, the current becomes negative - corresponding to ion intercalation (reduction/coloring). As the voltage increases, the current switches from negative to positive, undergoes a broad maximum, and reaches zero again at 0.25 V (vs Ag/Ag⁺). This represents ion de-intercalation (oxidation/bleaching)^[128]:



The overall behavior of the curve is comparable to a reported CV-diagram of amorphous WO₃^[103,124,129]. This CV-shape is typical for amorphous and/or nanocrystalline WO₃, with intercalation sites showing broad distribution with different energy levels^[22,130]. Moreover, the metal mesh exhibits higher overall current density, meaning that, at equivalent voltages, more ions are intercalated in the EC coating compared to the ITO10 sample. For reactions related to ion diffusion, the diffusion of Li⁺ ions into/out of the EC film can be determined based the Randles-Sevcik equation at room temperature^[131].

$$i_p = 2.69 \times 10^5 n^{3/2} C_0 \sqrt{D^+ \nu} \quad (5.9)$$

where i_p is the peak current, D^+ the diffusion coefficient, $n = 1$ the number of electron, C_0 the concentration of active ion in electrolyte and ν the scan rate. The higher the diffusion coefficient, the larger the contact area and the greater the porosity, leading to faster ion insertion/extraction.

In the case of WO₃, the relationship between peak currents and scan rates appears linear, meaning that the reaction of the insertion and extraction of ions is a diffusion-controlled process^[132]. The resulting diffusion coefficients are in the order of 10⁻¹⁰ - 10⁻¹¹ cm²/s which is also similar to reported values^[22,133-135]. It can be noted that the diffusion leading to coloration (intercalation) is higher than the bleaching (de-intercalation). This can be explained by the fact that both processes are not symmetrical. It is believed that the intercalation of Li⁺ ions is mostly influenced by the interface between the EC material and the electrolyte, whereas the de-intercalation is largely governed by ion transport in the film^[103].

Figure 5.9c and 5.9d present the CA experiment where the voltage is switched between -1.25/+0.25 V (vs Ag/Ag⁺). As previously seen in the CV diagram, the metal mesh exhibits higher current density than ITO10 but lower amplitude in the switching range between the bleached and colored states. It means that ITO10 achieves higher efficiency in switching states. This is defined (see Eq.5.12) as coloration efficiency (CE) and can be calculated using charge density (Eq. 5.10) and optical density (Eq. 5.11). A higher CE provides a large optical modulation with small charge insertion or extraction which increases the long-term stability of the ECD^[136].

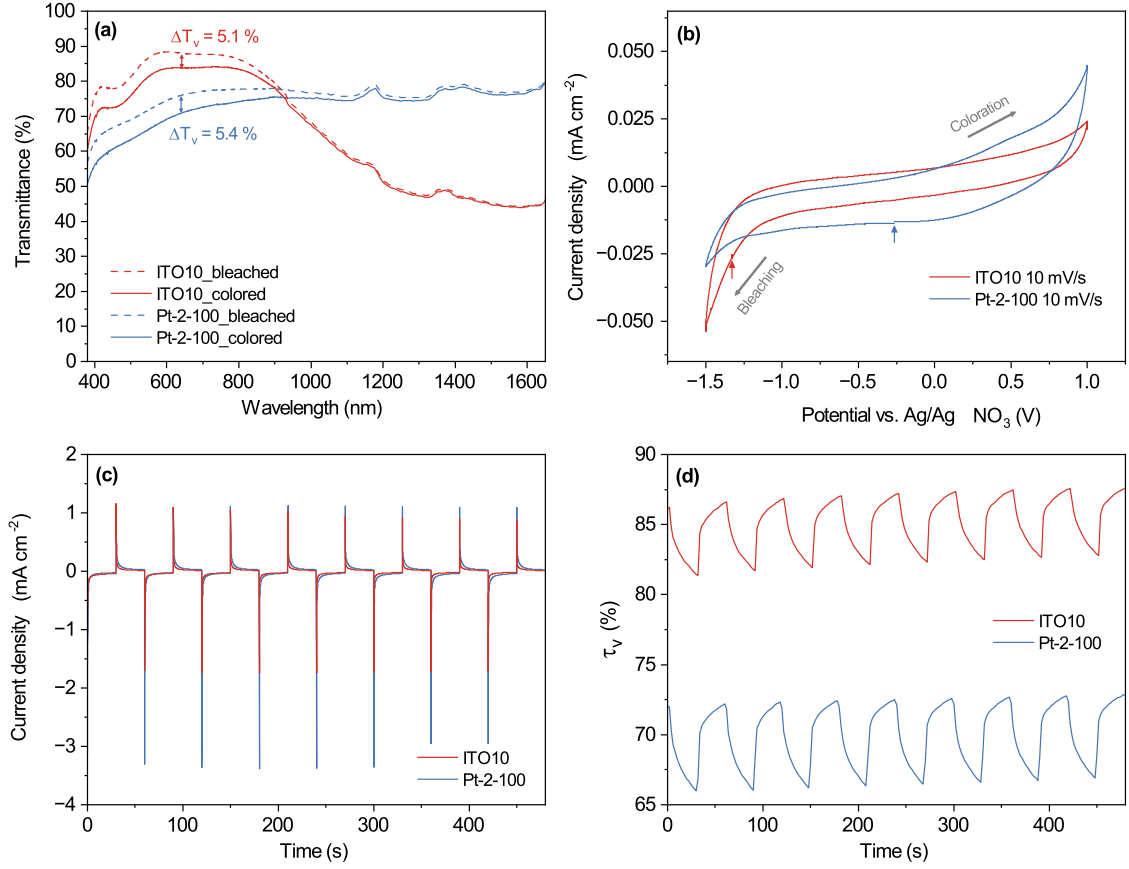


Figure 5.10: Electrochromic properties of the Ta:NiO anode in Li-PC measured at -1.5/+1 V (vs Ag/Ag⁺) comparing ITO and the metal mesh: **(a)** Transmittance spectra in colored and bleached taken from CA measurements. **(b)** Cyclic voltammograms at a scan rate of 10 mV/s at which the vertical arrows give the open circuit voltage where the scan started/ended. **(c)** Chronoamperometry curves for 8 cycles of 30 s and **(d)** the resulting in situ visible transmittance.

As presented in Table 5.4, the CE of Pt-2-100 and ITO10 gives, respectively, 12.5 and 36.4 cm^2/C . These values are comparable to the reported CE for WO₃ (14.9 - 140.8 cm^2/C)^[137-142].

$$Q = \int_0^t i dt \quad (5.10)$$

with Q being the inserted charge (C) and i the current (A) .

$$\Delta OD = \log(T_{v,b}/T_{v,c}) \quad (5.11)$$

$$CE = \frac{\Delta OD}{Q/A} \quad (5.12)$$

Chapter 5. Electrochromic device with hierarchical metal mesh electrodes

where ΔOD is the change in the optical density, Q is the inserted charge, A the surface and $T_{v,b}$ and $T_{v,c}$ refer to the visible transmittance of the film during the bleached and coloration states, respectively.

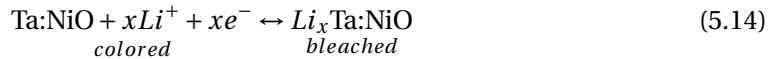
Another important parameter to assess the performance of an EC coating is the intercalation level (x in Li_xWO_3) which is dependent on the charge density and indicates the ability of the film to interleave ions (see Eq. 5.13). In the case of WO_3 , it reaches 57.5 % and 23.8 % for respectively Pt-2-100 and ITO10 which stays below the reported value of $x \approx 65$ % where significant non-reversible ion trapping occurs^[143].

$$x = \frac{QMP}{eAptN_A} \quad (5.13)$$

where Q represents the inserted charge from the CA data, M the molar mass, P the packing density, e the elementary charge, A the area and t the film thickness.

For the anodic side of the ECD, a tantalum-doped nickel oxide was deposited on both samples. It has been shown that tantalum doping increases the optical properties of nickel oxide, it also renders it non-magnetic which enhances its compatibility with industrial large-scale depositions^[144]. Similarly to the cathode, it can be seen that the transmittance (Fig. 5.10a) of the metal mesh sample exhibits higher transparency in the NIR but transmits less light in the visible spectrum. The darkening effect for both samples remains relatively low.

In the case of the voltammetry experiment (see 5.10b), the Ta:NiO anode exhibits an opposite coloring behavior than WO_3 : the ion intercalation (reduction) is correlated to the bleaching of the sample and the de-intercalation leads to coloring^[145].



The CV-curves presented in Figure 5.10b exhibit a smooth transition and can be compared to other CV measurements on NiO films^[146,147]. In these reported voltammograms, a peak in current density can be seen during bleaching and coloration, but is not entirely visible in the measurements herein. Figure 5.10c and 5.10d present the CA experiment where the voltage is switched between -1.5/+1 V (vs Ag/Ag⁺). As depicted in Table 5.4, the number of inserted ions is higher in the case of the metal mesh (1.9 % and 0.95%) and the resulting CE (12.1 and 21.3 cm²/C) is lower than that of ITO10. Compared to WO_3 , the Ta:NiO coating provides less ions insertion and longer switching speed. A possible explanation might be the fact that film porosity is lower for Ta:NiO (7.1%), which reduces the mobility of Li⁺ ions. This is consistent with the rather low diffusion coefficients in the range of 10⁻¹³ and 10⁻¹⁴ cm²/s which is less than the reported values for NiO (10⁻¹⁰ cm²/s)^[148]. A more porous structure could improve the electrolyte penetration and provide a larger surface area for charge-transfer reactions.

Table 5.4: Electrochromic properties for the cathode, anode and fully functional ECD. t_c and t_b give the switching time needed to reach 95 % and D_c^+ , D_b^+ the diffusion coefficient for, respectively, the coloration and bleaching state.

Electrode	CA								CV		
	CE $\left(\frac{cm^2}{C}\right)$	Q_{ins}/A $\left(\frac{mC}{cm^2}\right)$	Q_{ext}/A $\left(\frac{mC}{cm^2}\right)$	x (%)	t_c (s)	t_b (s)	ΔT_v (%)	ΔT_e (%)	D_c^+ $\left(\frac{cm^2}{s}\right)$	D_b^+ $\left(\frac{cm^2}{s}\right)$	
Cathode (WO ₃)	Pt-2-100	12.5	-45.9	44.9	57.5	14	12	61	-	1.6×10^{-10}	1.2×10^{-10}
	ITO10	36.4	-19	18.5	23.8	16	12	67.8	-	3.3×10^{-11}	2.4×10^{-11}
Anode (Ta:NiO)	Pt-2-100	12.1	-2.78	1.9	1.9	26	22	5.4	-	1.1×10^{-13}	7.0×10^{-14}
	ITO10	21.3	-1.24	0.95	0.86	28	24	5.1	-	7.8×10^{-14}	2.4×10^{-14}
EC-device	Pt-2-100	25.5	-15.9	14.3	19.9 ^a 10 ^b	18	18	35.7	36.1	-	-
	ITO10	34.8	-10.3	7.4	12.9 ^a 5.1 ^b	22	12	33.6	24.3	-	-

^a inserted Li⁺ ion in WO₃, ^b inserted Li⁺ ion in Ta:NiO.

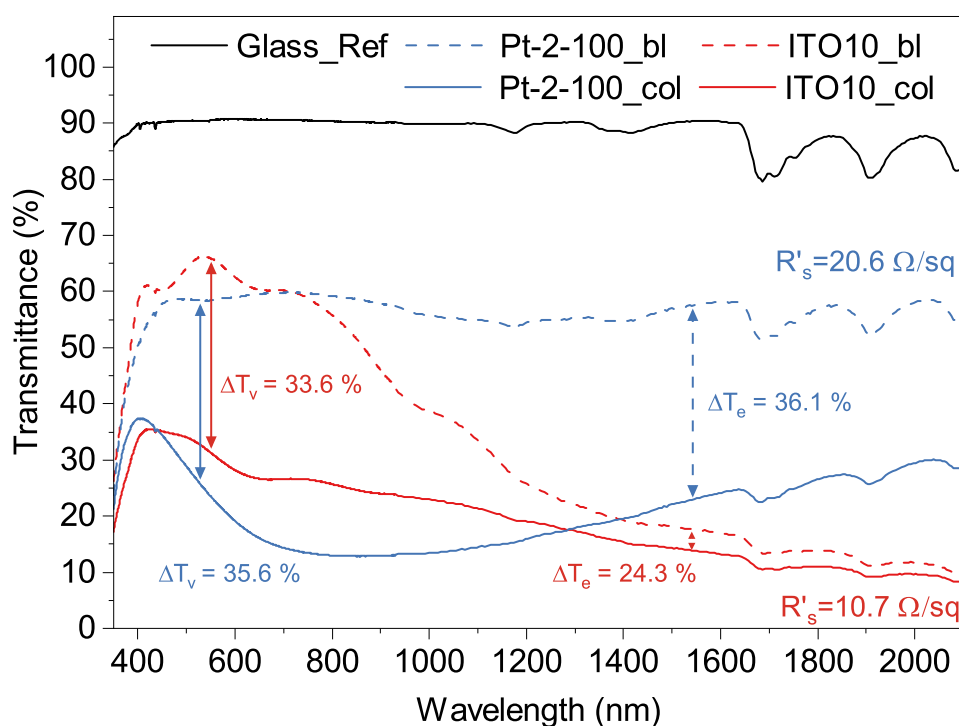


Figure 5.11: UV-Vis-NIR transmittance spectra of the full-device taken from the CA experiment comparing the metal mesh and ITO10 in the bleached and colored states. The modulation in solar transmittance is significantly larger for Pt-2-100 (36.1 %) compared to ITO (24.3 %).

5.3.3 Electrochromic device

Two fully functional electrochromic devices (ITO10 and Pt-2-100) are fabricated based on the setup presented in Fig. 5.4. The transmittance of both samples in the bleached and colored states are compared in Figure 5.11. The black curve represents the transmittance of a reference sample with two glass slides and the electrolyte. From this curve, it can be seen that weak absorption from the electrolyte still occurs at 1700 and 1900 nm, creating a decrease in transmittance. As mentioned before, the large spectral range of this setup allows to determine visible and solar transmittance (Eq. 4.7 and 4.8). The light modulation in the visible spectrum (Table 5.4) is similar for the ITO10 sample ($\Delta T_v = 33.6\%$) and the metal mesh ($\Delta T_v = 35.6\%$). In the NIR region, the transmittance of the metal mesh ($\Delta T_e = 36.1\%$) is considerably larger than ITO10 ($\Delta T_e = 24.3\%$). This can be attributed to the higher NIR transmittance of the metal mesh (as explained in the TCF section). It is worth mentioning that the NIR transmittance could be further reduced below 10% by increasing the thickness of the film, as previously shown^[98].

Figures 5.12a and 5.12b present the voltammograms of Pt-2-100 and ITO100. The sweep voltage range (-2.5/4 V for the metal mesh and -2.5/2.5 V for ITO) was chosen due to the stability of the device. It was found that for voltages above 2.5 V, the device with ITO would start to show a brownish coloration, potentially due to a reduction of the ITO layer, leading to degradation and irreversible damage of the sample^[149]. A strong peak can be seen during the bleaching of Pt-2-100. This peak is thought to be related to ion intercalation within the Ta:NiO layer, which was previously reported for NiO^[146,147]. As depicted in Table 5.4, the intercalation level of Li⁺ ions in Ta:NiO layer is ~5x larger compared to bleaching of the anode alone. This finding suggests that the electrical potential on the anode is higher in the full device and could be a limiting factor for switching efficiency.

During coloration, several peaks are observed in the device with a metal mesh, and these are more pronounced at a faster scan rate. These features may be related to the reduction of $W^{6+} \rightarrow W^{5+}$ or $W^{5+} \rightarrow W^{4+}$ which results in the blueish coloration of WO_3 ^[150]. The drop in current density happening during the bleaching of the metal mesh (Fig.5.12a) might occur from side reactions originating from the interface between the EC material and the metal mesh, such as gas evolution or substrate decomposition.

CA experiments are carried out on the electrochromic devices and are presented in Figures 5.12c and d. It can be seen that the coloration speed of the metal mesh ($t_c = 18$ s) is faster than the one for ITO ($t_c = 22$ s). This effect might be due to an unfavorable interface between the EC material and the ITO, leading to a decrease in ion permeability.

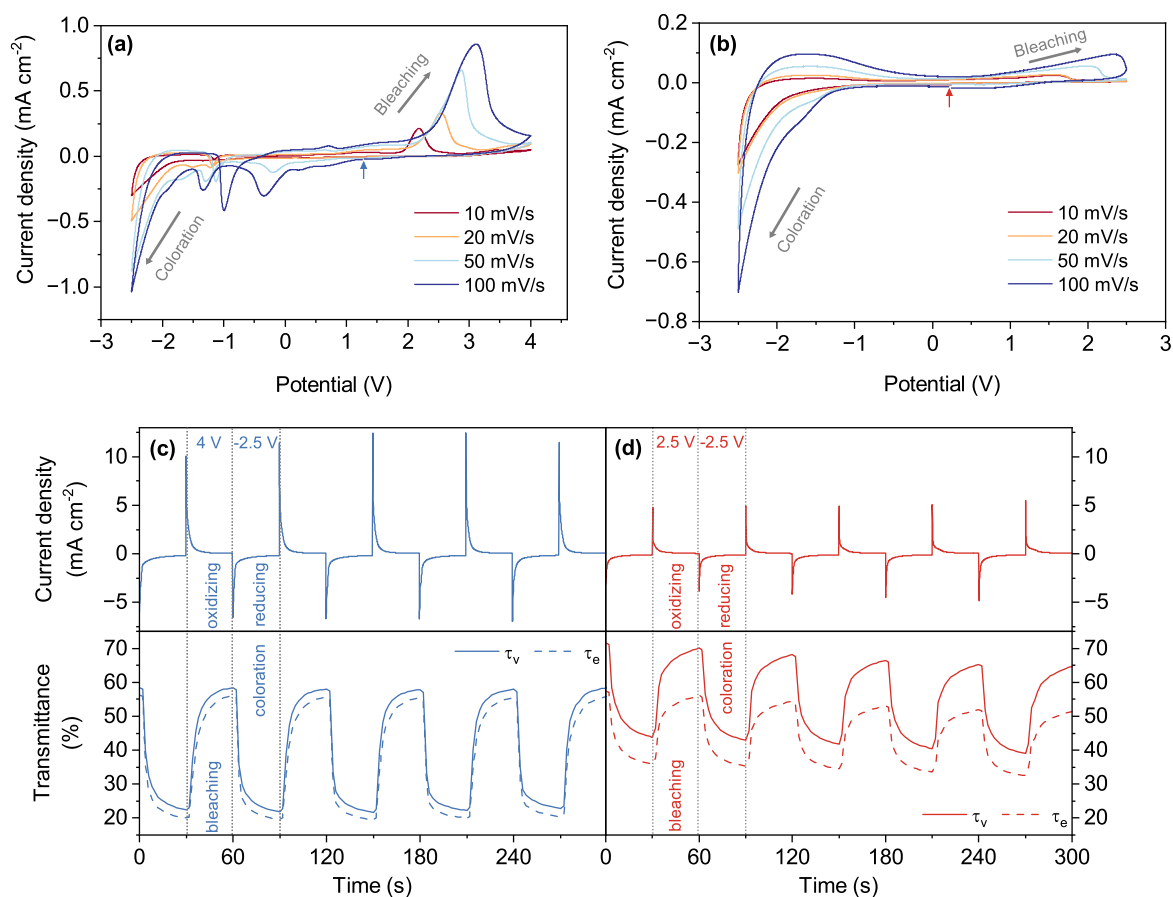


Figure 5.12: Electrochromic properties of full devices in Li-PC measured at -2.5/+4 V for the metal mesh, (a,c), and at -2.5/+2.5 V for ITO, (b,d): (a,b) Cyclic voltammograms at a scan rate of 10, 20, 50 and 100 mV/s where the vertical arrows give the open circuit voltage at which the scan started/ended. (c) Chronoamperometry curves for 5 cycles and (d) the resulting in situ visible and solar transmittance.

As shown in Table 5.4, ΔQ ($Q_{ins} - Q_{ext} = 2.9 \text{ mC/cm}^2$) of ITO10 is rather large, meaning that irreversible incorporation of Li⁺ ions is taking place. This is a well-known cause for degradation of EC WO₃ thin films^[151]. This degradation can also be seen in the transmittance spectra of ITO10 where T_v and T_e slowly decrease after each cycle. On the other hand, Pt-2-100 exhibits a low charge density difference between the inserted and extracted ions, and the transmittance stays constant over the 5 cycles. Pictures of the coloration/bleaching process is shown in Figure 5.13. Further investigation will be needed to determine durability over several hundred cycles.

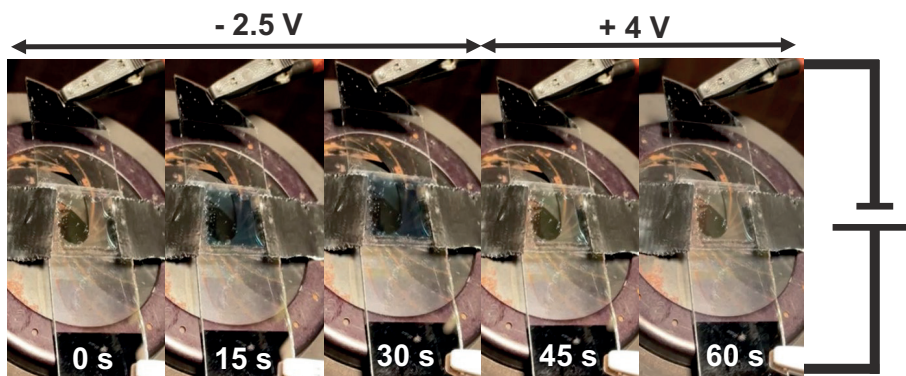


Figure 5.13: Photos of the Pt-2-100 metal mesh ECD during coloration/bleaching process. First a -2.5 V potential is applied for 30 s leading the coloration. Then it is switched to 4 V for the bleaching phase. The black circle behind the device is the diaphragm opening to the spectrometer.

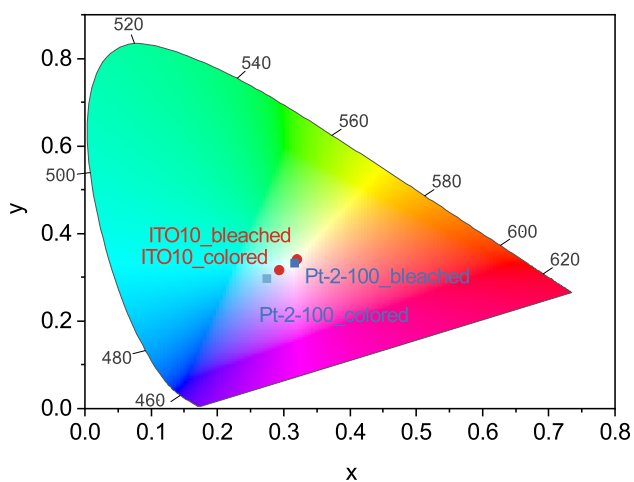


Figure 5.14: CIE 1931 color diagram with the x, y color coordinates of full devices in colored and bleached states. Pt-2-100 shows a slightly more pronounced blue tint in the colored state.

Finally, the color diagram of both samples is presented in Figure 5.14. In the bleached state, the color is similar for both samples. In contrast, ITO is slightly more color-neutral in the colored state. As presented in Fig. 5.11, oscillations due to interference in the visible spectrum can be seen for ITO in the bleached state. This indicates a difference in the refractive index between the layers, which could have an influence on the color of the device. Generally, the blue hue in

the colored state is less pronounced than in other reported values for WO_3 [19,152]. This can be explained by the fact that WO_3 is combined with Ta:NiO, which exhibits a slight yellow tint (complementary color of blue) in the colored state thereby reducing the prominence of the blue color.

5.4 Conclusion

The aim of the present research was to examine the use of hierarchical metal meshes as a replacement of ITO transparent conductive electrodes in ECDs. Metal meshes are fabricated and characterized, they show excellent electrical conductivity and wide-band optical transmittance. WO_3 and Ta:NiO electrochromic coatings are then successfully deposited on the metal mesh electrodes by plasma sputtering, and characterized as separate cathode and anode. Both WO_3 and Ta:NiO films deposited on the metal mesh exhibit high transmittance, not only in the visible, but also in the NIR spectrum. Finally, an ECD based on the hierarchical metal mesh substrate is assembled. The resulting device achieves remarkable optical modulation in the full spectral range of solar radiation compared to conventional ITO-based devices. This study opens up the path to hierarchical metal mesh based ECDs which have a high potential for energy savings through wide band modulation of the solar heat gain in buildings of countries with varying climates.

6 ELECTRONIC PROPERTIES AND ION MIGRATION OF WO₃:MO THIN FILMS

This chapter is based on the published journal paper^[126]:

Fleury, J., Burnier, L. and Schüler, A., 2022. Electronic properties and ion migration of “in vacuo” lithiated nanoporous WO₃: Mo thin films. *Journal of Applied Physics*, 131(1), p.015301.

Author contribution for the journal paper:

In this article, JF designed the research with the support of all co-authors. JF prepared all the figures and conducted the analysis of the results as well as the redaction of the manuscript. JF helped for the XPS and UPS characterization of the sample and was responsible for the submission process. All co-authors supported in revising and finalizing the manuscript.

This chapter investigates the potential of electrochromic (EC) glazing by doping the electrochromic coating with molybdenum. It relates the optical and electronic properties of nanoporous amorphous molybdenum doped tungsten trioxide thin films (WO₃:Mo) in the bleached state and upon lithiation. When such film is used as a cathode in EC devices, the color neutrality could be improved with respect to pure WO₃ and electrochromic transmittance control could be achieved in the full spectral range of solar radiation. This will help manage daylight and solar heat gains in building thereby allowing a reduction of energy consumption caused by heating, cooling and artificial lighting.

6.1 Introduction

EC materials are increasingly used in buildings as smart windows to dynamically control the heat gains by solar radiation as well as visual comfort and is often seen as the future of shading in buildings.^[72,153] They represent a promising and functional alternative to the traditional Venetian blind facilitating glare reduction (transmittance below 1%), offering unobstructed

views and natural day lighting while, at the same time, reducing the energy consumption for heating and cooling. As an example, in 2017, space heating was the dominant part of Swiss energy consumption (239.2 PJ), corresponding to a share of 31.3 % of the total energy (763.4 PJ) [69]. An important part of this energy is lost through the building fenestration because of poor energy efficient glazing which are not adjustable to dynamic climate fluctuations. [78] A modulation of the transmittance in the visible and near-infrared (NIR) spectra improves the selectivity over the solar spectrum and thus reduces the energy consumption. Previous studies have reported a NIR-selective electrochromic device by incorporating nanocrystals into amorphous materials. [79–81]

Moreover, it is thought that a combination of molybdenum and tungsten trioxide could also exhibit a selective behaviour. Pure tungsten trioxide is widely known for its excellent electrochromic properties and numerous studies have reported positive further improvement, such as color neutrality by incorporating molybdenum in this material. [154–156] It was shown that Mo-doping promotes the coloration efficiency in both visible and NIR regions, [157–160] and enhances the mechanical properties. [161] Although several investigations have been carried out on molybdenum doped tungsten trioxide for electrochromic devices, [98,162–166] there has been little scientific research regarding the lithiation process specifically. The aim of this study is to investigate the electronic structure and optical properties of Mo doped WO₃ using X-ray and Ultraviolet Photoelectron Spectroscopy (XPS, UPS). In particular, it will focus on the interactions between lithium ions in the material and their affinity towards tungsten or molybdenum.

6.2 Methodology

6.2.1 Film Preparation

Reactive sputtering in a sputter-up configuration was used as the deposition method. The setup consists of five magnetrons and allows for co-sputtering of thin films using two different direct-current (DC) power sources. The WO₃:Mo layer examined in this study was deposited on silicon and glass substrates from the following targets: tungsten (Kurt J Lesker 99.95 % purity) and a molybdenum (Codex-International 99.95 % purity) with a diameter of 50.8 mm (2"). The specific deposition parameters are shown in Table 6.1. A working pressure in the range of 10⁻² mbar was shown to provide a nanoporosity which is beneficial for ions permeability in EC devices. These parameters were previously optimized by Lagier et al. and further details about the setup can be found in a recent publication. [98] In this work, new samples were specifically produced for an extensive XPS/UPS measurement campaign to understand the electronic properties of WO₃:Mo and the migration of ions during lithiation.

The lithiation process was conducted in a vacuum chamber connected in-line to the main sputtering chamber. The setup consisted of a lithium dispenser (LI/NF/1.25/25 FT10 + 10) [167] which was thermally evaporated by a chemical reaction between lithium chromate (Li₂CrO₄) and a getter material (Zr-Al 84-16 %). It was shown that pure alkali materials can be deposited by evaporation with low amounts of residual oxygen and hydrogen. [168] The sample was

Table 6.1: Deposition parameters. The working pressure in the range of 10^{-2} mbar allowed for the growth of a nanoporous coating which is beneficial for ions permeability in EC devices.

Mo _{0.1} W _{0.9} O ₃		
Target	W	Mo
Applied power	DC 150 W	DC 120 W
Deposition time	3 min 30 sec	
Thickness	70 nm	
Ar (sccm)	18	
O ₂ (sccm)	6	
Ratio O ₂ /Ar	33 %	
Working pressure	2.9×10^{-2} mbar	

repeatedly lithiated for short periods of time and characterized between each step. The amount of lithium deposited was measured with a quartz crystal microbalance and the concentration was compared to the tungsten content in the film. For accurate assessment, the lithium content of one evaporated dispenser was determined by inductively coupled plasma mass spectrometry.^[19]

6.2.2 X-ray and Ultraviolet Photoelectron Spectroscopy (XPS, UPS)

XPS and UPS were performed in a high vacuum cluster allowing an in-situ transfer between the deposition and characterization chamber. This setup allows for the surface to be observed "as deposited", without any contamination which represents a significant advantage since XPS and UPS are highly surface-sensitive techniques. XPS measurements were performed on the sample after each lithiation evaporation to understand the electronic state and the chemical environment. The XPS-setup consists of a unmonochromatized Mg K α line at 1253.6 eV (12 keV with 25 mA anode current), an energy analyzer (Leybold EA-11) and achieves a resolution in the order of 1.2 eV. The survey scans were measured at a pass energy of 50.4 eV and the high-resolution core-level spectra of the elements at 29.9 eV. The spectrometer energy scale was calibrated with a gold bulk element (99.99 % purity), taking Au 4f_{7/2} core level signal at 83.8 eV binding energy (BE) as a reference.^[169,170] The pressure in the characterization chamber was kept below 4×10^{-8} mbar during analysis. UPS was used to precisely analyze the electronic states at lower binding energy (in the range of tens of eV). The setup comprises a helium discharge lamp with a energy of $h\nu = 21.22$ (He I). UPS spectra were calibrated with the Fermi level measured on the gold reference sample. The resolution is given by the width of the Fermi level cut-off, which in this case is 0.4 eV. The work function and valence band maximum were determined from, respectively, the high and low BE cutoff region of the spectra. Concentrations of the elements and deconvolutions were obtained with CasaXPS software. The composition of the sample was calculated from the core level signals after subtracting a Shirley background and using the Scofield derived relative sensitivity factors (RSF).

6.2.3 Optical Characterization

A variable-angle spectroscopic ellipsometer (SE-2000 from Semilab) was used to determine the thickness and porosity of the sample. The data were analyzed with "SEA" software using a Cauchy dispersion law to determine the refractive index and thickness. Transmittance spectra were measured from 350 to 2100 nm with a Zeiss diode array spectrometer (MCS 601 and MCS 611). The light sources comprise quartz tungsten halogen lamps and ultraviolet fluorescence lamps with a diffusing panel in the front. Both light sources were connected to a stabilized DC power supplies to ensure a continuous stability of radiation intensity.

6.2.4 Determination of optical band gap

The calculation of the optical band gap (E_g) for indirect electron transitions in WO₃:Mo was done by means of a Tauc plot (eq. 6.1). The optical band gap can be determined by extrapolating the linear region of $(\alpha h\nu)^{1/2}$ curve and reading the energy value from the linear extrapolation and the intersection with the abscissa.

$$(\alpha h\nu)^{1/n} = K(h\nu - E_g) \quad (6.1)$$

with α being the absorption coefficient, h Planck constant, ν light frequency, E_g optical band gap energy and K a constant. n is related to the type of optical transition of the semiconductor ($n=2$ for indirect allowed transition as it is the case for WO₃).^[171]

6.3 Results & Discussion

6.3.1 XPS

The chemical composition and oxidation state of lithium ions intercalated into WO₃:Mo were studied by XPS analysis. The composition was found to be Mo_{0.1}W_{0.9}O₃. The survey spectra showed no traces of C adsorbents, thus providing a contamination-free environment on the sample surface. As reported by Dixon et al.^[172], it is of critical importance to minimize the surface contamination to achieve high quality surface measurement and, at the same time, avoiding the use of argon ion sputtering which could lead to a reduction of tungsten and thus modify the measured spectra.^[173] Because of their very small photo-ionization cross-section, core levels due to the intercalated lithium ions could not be observed by XPS.^[103]

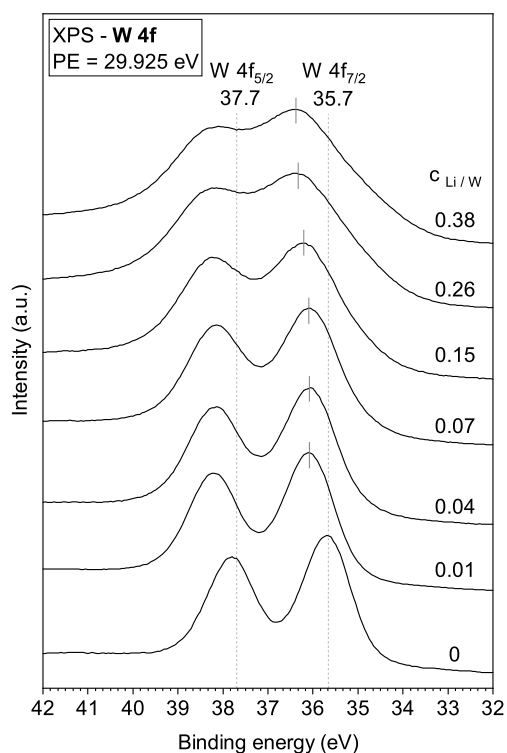


Figure 6.1: XPS Core-level spectra of W 4f doublet. The curves compare the different nominal concentrations of lithium ions over tungsten content ($c_{Li/W}$). For higher concentration, the peaks are shifting to higher BE and the doublet is broadened, the latter indicating the formation of W^{5+} oxidation states.

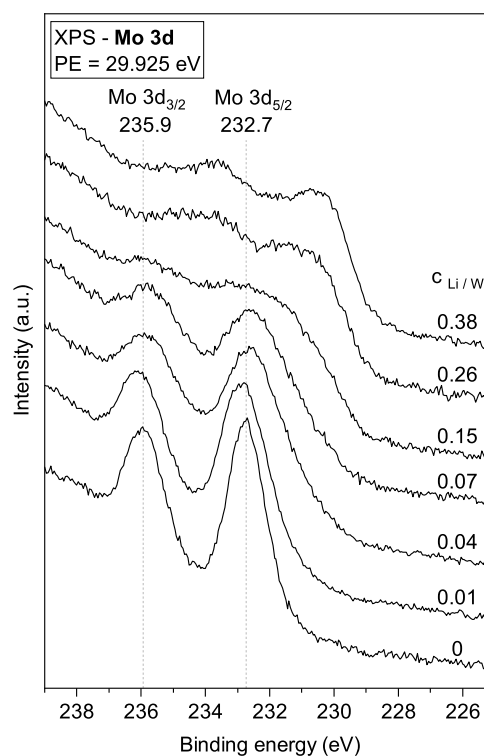


Figure 6.2: XPS Core-level spectra of Mo 3d doublet. The shape of the spectrum at $c_{Li/W} = 0.07$ has changed considerably, suggesting a higher concentration of Mo^{5+} oxidation states. This phenomenon is further accentuated with increasing lithium concentration and a new peak appears at lower BE.

As shown in Figure 6.1, the $W 4f_{7/2}$ and $W 4f_{5/2}$ peaks for pristine $Mo_{0.1}W_{0.9}O_3$ are located at 35.7 eV and 37.7 eV which is consistent with the values for $Mo_{0.05}W_{0.95}O_3$ measured by Wang et al.^[174] As a comparison, $W 4f_{7/2}$ peak in WO_3 was reported to be between 35.3 to 36 eV.^[175–179] Figure 6.2 shows the high-resolution spectra of $Mo 3d_{5/2}$ and $3d_{3/2}$ peaks which are located, respectively, at 232.7 eV and 235.9 eV. These values are similar to those reported in the literature for pure MoO_3 .^[177,180–183] The O 1s photoemission peak is presented in Figure 6.3 and is located at 530.6 eV. Vasilopoulou et al. measured comparable values of 530.6 and 530.4 eV for, respectively, WO_3 and MoO_3 oxides^[184,185] which are assigned to the typical W-O and Mo-O bond.^[186,187] As it can be observed in all three core-level spectra, the lithiation process causes a general tendency to increase the binding energies. This shift may be explained by the reduction of W and Mo atoms which could yield abundant mid-gap states and lead to a blue shift of the Fermi Level.^[163,188] Indeed, it was shown that the mechanism by which intercalated alkali atoms contribute to electrochromic nature of WO_3 exhibits similar behaviour as oxygen

vacancies.^[189–191] It is thus thought that, during the lithiation process, the electronic structure undergoes specific changes regarding the core levels of tungsten and molybdenum oxides.

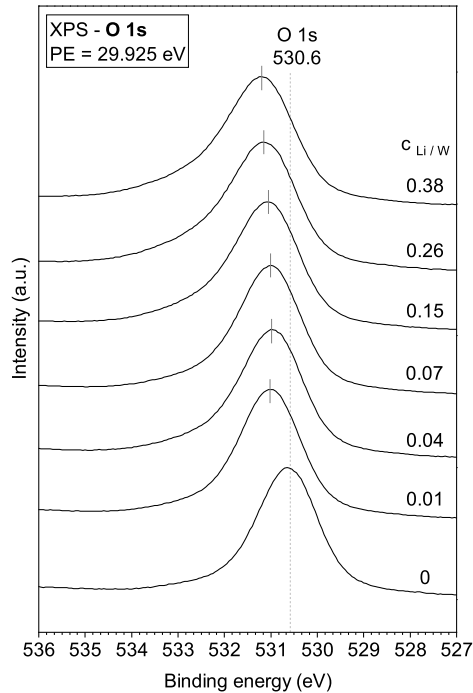


Figure 6.3: XPS Core-level spectra of O 1s peak. A shift towards higher BE can be seen as the lithium concentration increases.

Figure 6.4a and 6.4b depict a deconvolution of the WO₃ and MoO₃ core-level spectra, obtaining quantitative information on the relative number of W / Mo atoms in their corresponding oxidation states. The deconvolution in Figure 6.4a was performed using Gaussian-Lorentzian contributions after the subtraction of a Shirley background. The W 4f doublets were constrained by a W 4f_{5/2}:W 4f_{7/2} spin-orbit separation of 2.15 eV^[192] and the areal ratio was set to 3:4. The full width at half maximum of both peaks were similar, therefore a constrain was set for all other doublets. In addition to the two major peaks present in the non-lithiated state, another doublet appeared with increasing lithium content. It is ascribed to the presence of W⁵⁺ oxidation states which are associated to the blue coloration of the lithiated tungsten oxide^[103]. The small feature at 41 eV is linked to the W 5p_{3/2} core level. In the case of MoO₃ core-level (Figure 6.4b), the spectrum could not be subtracted with a Shirley background because of the close proximity to the W 4d peaks (247 eV), hence a linear background was used. The W 3d doublets were constrained by a Mo 3d_{3/2}:Mo 3d_{5/2} spin-orbit separation of 3.13 eV^[183] and the peak area ratio was set to 3:2. It can be seen that, even for small amount of intercalated lithium ions, the shape of the spectrum was modified considerably.

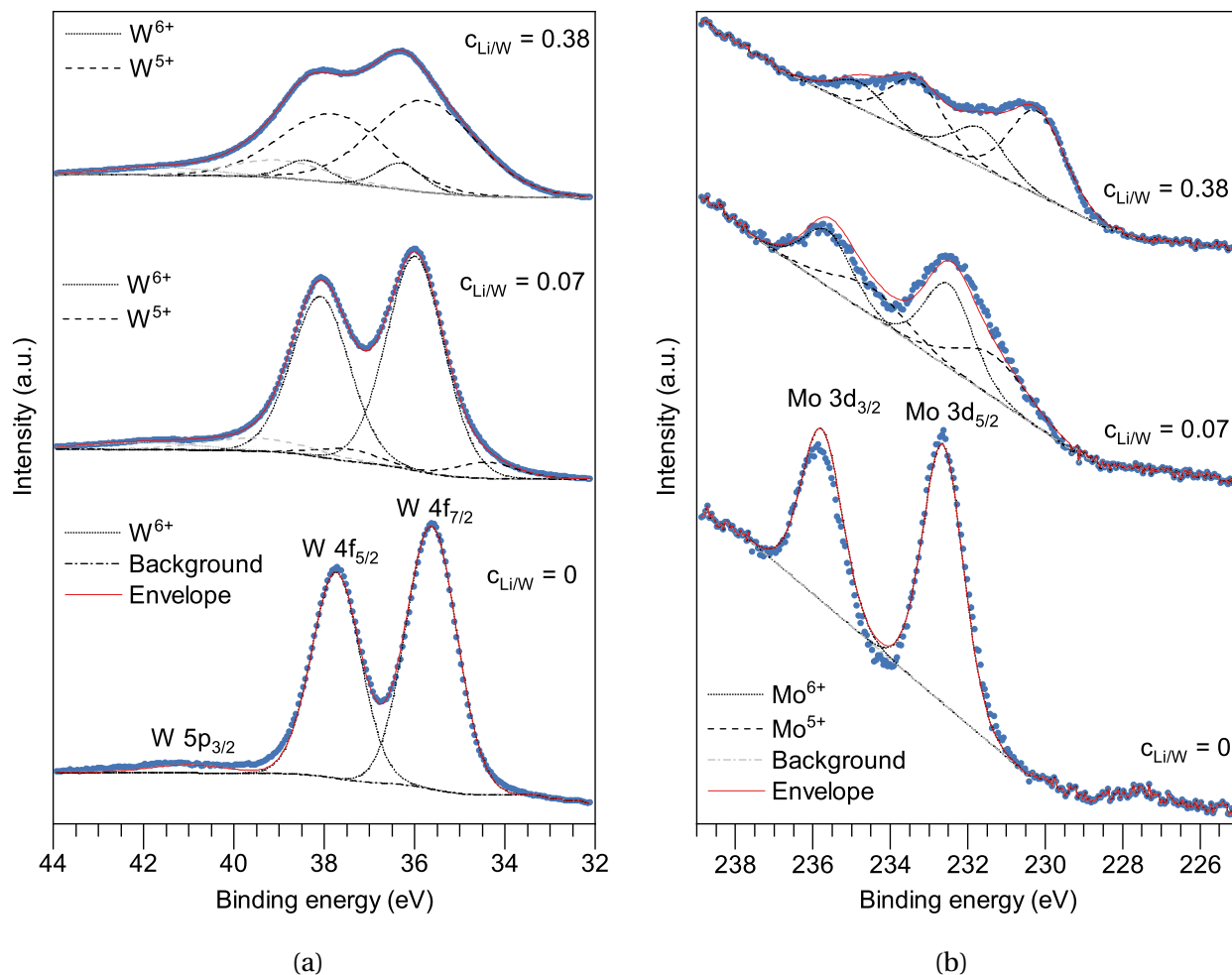


Figure 6.4: Deconvolution of (a) W 4f and (b) Mo 3d doublet at different nominal lithium concentration $c_{Li/W} = 0, 0.07$ and 0.38 . Experimental data are displayed in blue dots, contributions of W 4f and Mo 3d peaks in dark and W 5p in light grey. Both non-lithiated spectra ($c_{Li/W} = 0$) reveal a well-resolved doublet, attributed to the 6+ oxidation states. As the lithium concentration increases, the core levels change in line shape caused by the occurrence of 5+ oxidation states.

To compare the oxidation between the two core level spectra, the contribution of 6+ and 5+ oxidation states were calculated from the relative area under each doublet. The results are presented as a plot in Figure 6.5. It should be noted that the oxidation states are measured on the surface of the material (XPS) whereas the lithium content was calculated for the bulk film (nominal Li concentration). For lithium concentration below $c_{Li/W} = 0.07$, the lithiation process appears to occur predominantly in the Mo core level with a up to 25% difference of occupation states. Therefore it is thought that lithium ions have a higher affinity towards the

molybdenum atoms. This specific behaviour opens possibilities such as selectively lithiate one element at a time allowing for an adjustable coloration in electrochromic glazing.

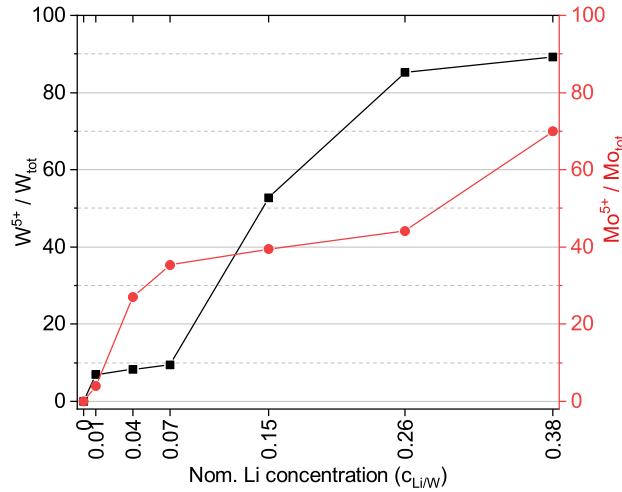


Figure 6.5: Relative number of tungsten and molybdenum atoms in 5+ state (W^{5+}/W_{tot} , Mo^{5+}/Mo_{tot}) vs. the bulk nominal concentration of lithium ions. The ratio of W^{5+} oxidation states increases slowly at $c_{Li/W} = 0.07$ and more significantly at the end of the lithiation process. In contrast, the number of Mo^{5+} oxidation states increase rapidly at the beginning of the lithiation and slower towards the end.

6.3.2 UPS and optical spectrometry

In this section, an attempt of describing the relation between the electronic structure and the spectral absorption of the material will be given using UPS and VIS-NIR spectrometer measurements. First the results from the He I measurements are presented and then a discussion is held about the energy levels.

Figure 6.6a shows the secondary-electron cut-off region of the spectra. As the number of intercalated ions increases, the onset edge of the valence band shifts towards higher binding energies, indicating a decrease of the work function. Figure 6.6b presents the full-range valence band spectra. The main features between 15 and 3 eV are generally associated to the oxygen orbitals in WO₃^[184,193] and MoO₃^[185]. The peak at approximately 6 eV is assigned to O 2p derived band and the bump between 12.0 and 14.0 eV corresponds to the hybridized W 4d and Mo 3d – O2p band. Figure 6.6c shows the valence band edge which is located around 3 eV below the Fermi level and shifts to 3.4 eV. The pristine WO₃:Mo film shows a pronounced Urbach tail extending down to 1 eV. Since such features was not reported for crystalline WO₃^[194], it is thought that large band tail originates from the amorphous nature of the coating.^[195] Additionally, two striking features are the peaks around 2.2 and 0.8 below

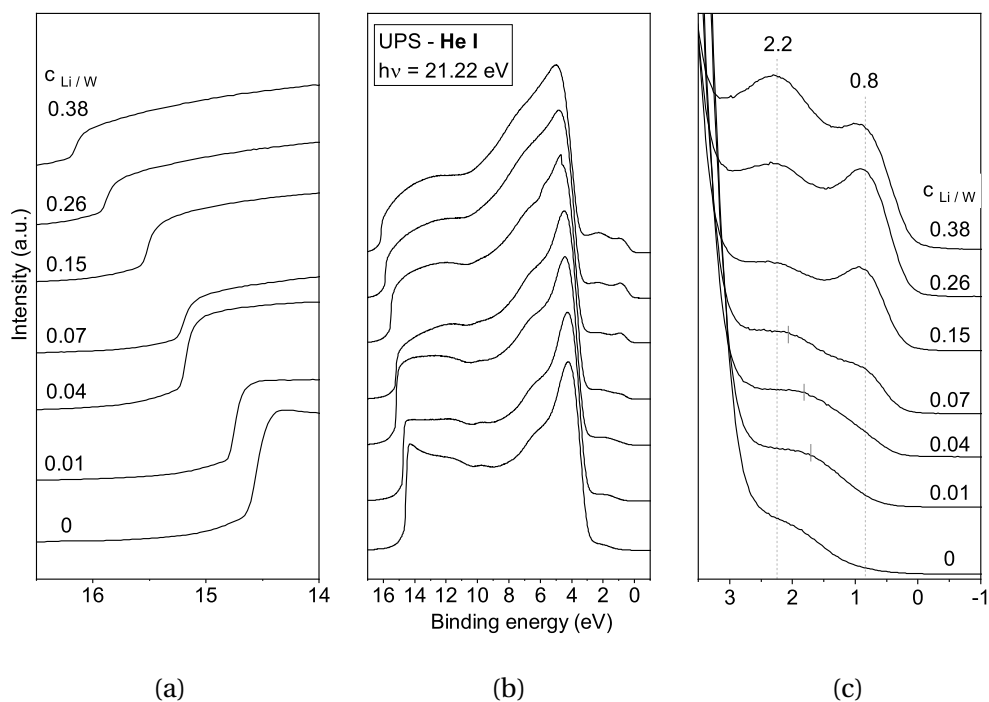


Figure 6.6: UPS photoemission spectra of $\text{Mo}_{0.1}\text{W}_{0.9}\text{O}_3$ with varying concentration of lithium ions $c_{\text{Li}/\text{W}}$ switching from as-deposited transparent to colored state with (a) being the secondary-electron cut-off region, (b) the entire view of the valence band spectra and (c) the near Fermi level region.

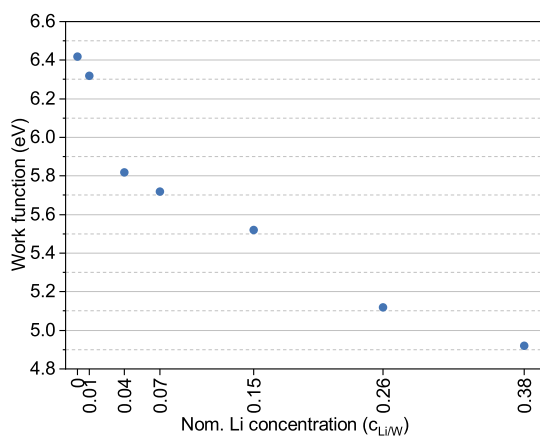


Figure 6.7: Plot of the work function at different nominal Li concentration. The work function declines rapidly with few intercalated lithium ions and then decreases linearly at higher ions content.

the Fermi level whose intensity increases under ion intercalation. These peaks match those observed in earlier studies for WO₃ [184,196] and MoO₃. [185,188,197]

Figure 6.7 shows the evolution of the work function for varying lithium concentration. Initially, the work function decreases rapidly which may be correlated to the density of donor states from the increase of 5+ oxidation states. The linear decrease that follows could be caused by the addition of low electronegative cations in the material. A similar behaviour of the work function was described by Greiner et al. for WO₃ and MoO₃. [197]

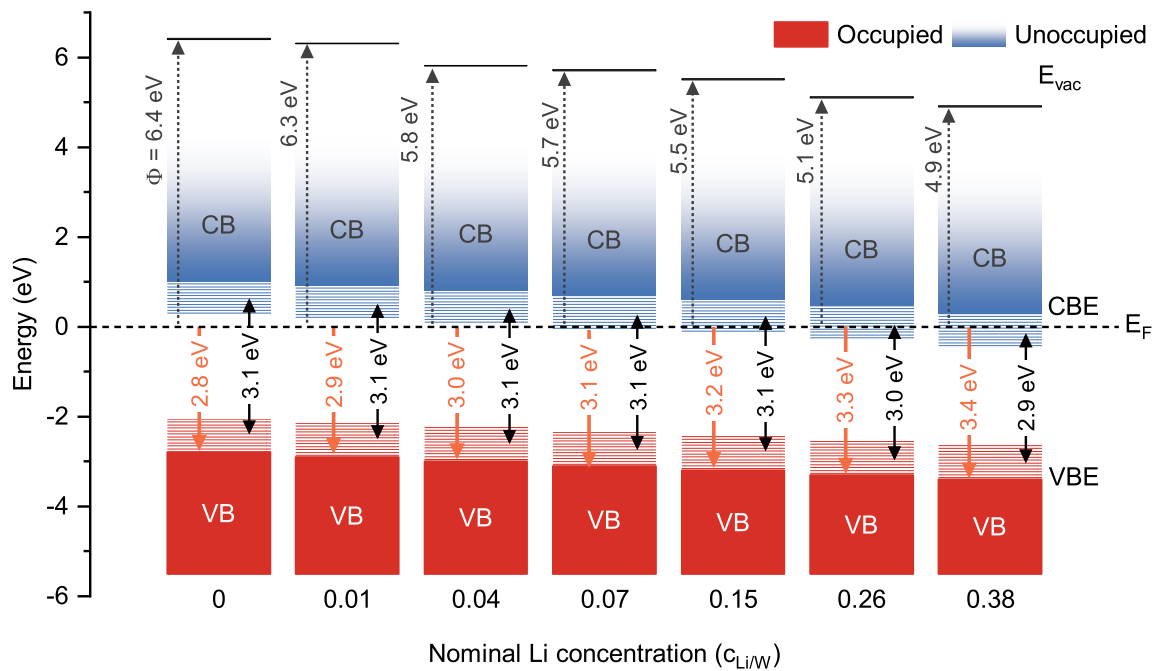


Figure 6.8: Schematic diagram of the energy levels in the valence and conduction band with increasing ion intercalation. The red and blue stripes describe partially localized states near the valence band and conduction band edge. The values in orange give the energy of VBE and in black the optical band gap. The dotted arrows represent the work function (Φ). The Fermi level (E_F) was set to a fixed value of 0 eV.

Figure 6.8 provides an overview of the energy levels in the valence and conduction band for varying lithium concentration based on the UPS spectra presented in Figure 6.6. The work function was calculated from the onset value in Figure 6.6a and the valence band edge (VBE) from the onset in Figure 6.6c. The optical band gap was derived from the transmittance spectra using the Tauc plot method described in section 6.2.4. It differs from the electronic band gap from the fact that it represents the threshold for photons to be absorbed, in contrast to the threshold of electron-hole pair creation. This difference is illustrated by the partially localized states (Urbach tail) above the VBE and the excitonic states [198] below the CBE. Both are

described by, respectively, the red and blue stripes in Figure 6.8 and 6.9. For $\text{Mo}_{0.1}\text{W}_{0.9}\text{O}_3$, the optical band gap starts at 3.1 eV and decreases to 2.9 eV which is consistent with other studies reporting values between 2.91 and 3.15 eV for WO_3 [195,199,200] and 2.78 for $\text{Mo}_{0.01}\text{W}_{0.99}\text{O}_3$. [156] As mentioned before, a shift towards higher BE can be observed (pushing the Fermi-level closer to the conduction band) which is indicative of the creation of new occupied states inside the band gap. This phenomenon can be explained by examining the crystal structure of Mo doped WO_3 : pure tungsten and molybdenum trioxide are known to be a defect perovskite-like ReO_3 octahedral crystal structure surrounded by six oxygen atoms. [171,201,202] This structure was demonstrated through first-principles density functional calculations [203,204] and also holds true for the short-range amorphous metal oxides like WO_3 and Mo_3 thin films. [205] This specific crystal structure and electric fields give rise to a split of the W 5d and Mo 4d orbitals into partially delocalized t_{2g} and e_g levels. The created orbitals are located near the edge of the conduction band and within the band gap, near the Fermi level. [171]

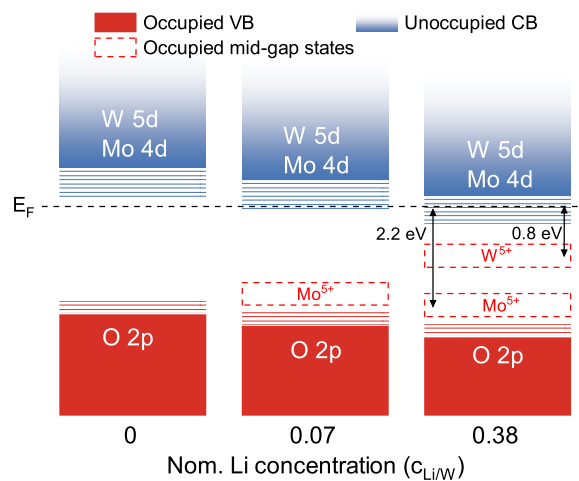


Figure 6.9: Energy level schematic of lithiated $\text{Mo}_{0.1}\text{W}_{0.9}\text{O}_3$ with O 2p, Mo 4d and W 5d bands. First the Mo^{5+} gap states are preferentially filled with the electrons from the lithium ions. In a second phase, the W^{5+} gap states are filled.

As shown in Figure 6.9, in pristine $\text{WO}_3:\text{Mo}$, the O 2p band is filled and the conduction band is empty, the optical band gap is thus wide enough to render it transparent. At the initial stages of lithiation ($c_{\text{Li}/\text{W}} = 0.07$), charges are preferably transferred from lithium to molybdenum t_{2g} bands of Mo 4d leading to the reduction of Mo^{6+} to Mo^{5+} . As observed previously in UPS, this is energetically favorable because the corresponding t_{2g} states have higher BE in Mo than W. This might also be related to the smaller extent of the d orbitals of Mo relatively to W meaning that the Li electrons are more confined near the Mo than the W ions. This is in agreement with the formation enthalpies from oxides obtained by Matskevich et al. [206]. The creation of these mid-gap states in the oxide's electronic structure leads to a wide absorption peak due the Mo-Mo (d-d) transition. The wide absorption maximum is located in the visible spectra

with a energy around 2.2 eV (560 nm) providing color neutrality. The optical absorption is strong due to sufficient overlapping of bonding and anti-bonding wave functions leading to high oscillator strengths. During this first stage of lithiation, the Fermi level is shifted towards the conduction band, as it occurs for n-type semi-conductors.^[207]

At higher Li concentrations, W⁶⁺ ions are more numerous than the Mo⁶⁺ ones, which suggests a reversing mechanism where the t_{2g} bands of W 5d are successively filled, creating another mid-gap band and an absorption peak between 1.3 and 0.8 eV (950 and 1550 nm). This leads to a shift of the overall absorption maximum towards higher wavelength. These observations are compatible with the model proposed by Greiner et al. and Vasilopoulou et al. for WO₃ and MoO₃.^[98,185,197] As demonstrated in the past for molybdenum^[208] and tungsten^[209], the occurrence of two bands within the gap also happens when reduced and when doped with hydrogen. Therefore this effect is not related to the nature of the dopant but rather to that of the materials.

The selective reduction of W and Mo, could potentially be used to build color neutral electrochromic glazing with tunable light transmittance in the visible and NIR spectrum. It is therefore especially interesting to investigate bilayer configurations and characterize the behaviour of each layer.



Figure 6.10: Cross-section schematic of the four combinations chosen to study the propagation of lithium in the material. The two configurations on the upper half are used as reference and the two at the bottom are the investigated bilayers.

6.3.3 Lithiation bilayers

To further investigate the propagation of lithium ions in the material, four type of samples with different configurations were prepared. As show in Figure 6.10, Mo_{0.1}W_{0.9}O₃ and WO₃ layers were deposited on glass and ITO with alternating layers sequence. The first sample consists of a single layer of WO₃ and the second one, of a single layer of WO₃:Mo. Bilayer 1 and

2 are double layers of each material with, respectively, $\text{WO}_3\text{:Mo}$ or WO_3 on top. All samples were then dry-lithiated in vacuo and the optical transmittance was measured for bleached and colored states (see Figure 6.11). It can be seen that both bilayer samples exhibit relatively similar transmittance spectra no matter which material is on top of the device. The optical density in the visible range (OD_{vis}) for WO_3 , $\text{WO}_3\text{:Mo}$, Bilayer 1 and 2 was, respectively, 1.57, 1.93, 1.72 and 1.59. The most striking distinction can be found in the visible range of the spectra in the colored states where pure WO_3 feature a sharp peak around 400 nm and a strong absorption in the NIR compared to the other samples. It is therefore likely that, in the case of bilayer 2 (WO_3 on top), the lithium ions diffuse through the WO_3 layer thanks to its high nano-porosity and columnar morphology.^[98] These findings also support the idea that Mo induced states have lower energy and act as a trap for the electrons.

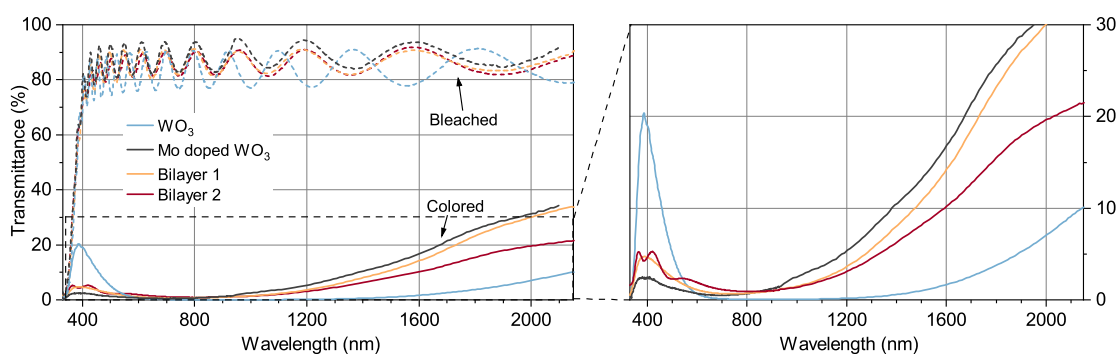


Figure 6.11: Spectral transmittance of the four investigated samples in bleached and colored states, where the right side shows a magnification of the curves in colored state. Bleached samples show oscillations due to interference fringes. Upon lithiation, all samples show similar transmittance with the exception of pure WO_3 which strongly transmits in the blue and absorbs in the NIR range. Bilayer 2 (with pure WO_3 on top) shows a VIS absorption in the blue range, which is characteristic to the $\text{WO}_3\text{:Mo}$ layer.

6.4 Conclusion

The present study contributes to existing knowledge on electrochromic material by providing XPS, UPS and optical characterization of $\text{Mo}_{0.1}\text{W}_{0.9}\text{O}_3$. It was shown that Li ions preferably fill the molybdenum 5+ states (energetically lower) and then, at higher concentration, the tungsten 5+ gap states are filled with a up to 25% difference of occupation state. The optical transmittance spectrum is in agreement with this statement and show a gradual rise in absorption in the amorphous molybdenum-doped tungsten trioxide film. The absorption band is first located around 550 nm (2.25 eV) and progressively shifts towards higher wavelength, up to 800 nm (1.55 eV). This variation in light absorption can be associated to the intercalation of lithium ions in newly formed partially delocalized t_{2g} mid-gap states. It was found from the UPS spectra that, upon lithiation, the VBE shifts to higher binding energies which leads to a decrease in the work function. Finally, it was shown that lithium ions are able to diffuse

Chapter 6. Electronic properties and ion migration of WO₃:Mo thin films

through the WO₃ in a bilayer configuration due to the high nano-porosity and columnar morphology of the coating. To the best of our knowledge, this is the first time that the lithiation process and more specifically the lithium affinity for WO₃:Mo is investigated by means of in-situ photoelectron spectroscopy. These findings could pave the way to future applications such as color neutral electrochromic windows with dual-band modulation of visible and NIR light. A natural progression of this work will be to investigate the practical application of WO₃:Mo as an electrochromic layer in a working device.

7 CONCLUSION

This chapter summarizes the highlights of the thesis and presents the contributions that this work has provided in regard to the research questions proposed in Section 1.5. Finally, an outlook provides suggestions about a multifunctional smart window design and further research directions.

In this doctoral thesis, the potential of reducing energy consumption by improving architectural glazing is studied. It is shown that commercially available low-e coatings in insulated glass unit (IGU) improve the energetic performance of the window but also have shortcomings. The main idea of this work is to look for solutions to overcome these disadvantages using laterally structured conductive coatings. This led to the first scientific question:

"How do EM waves interact with different designs of laterally structured conductive coatings and what are potential applications?"

It is demonstrated that metal coatings can be structured into patch arrays or mesh structures. These designs share similar physical properties where the patches act as a high-pass filter and the meshes as a low-pass filter. This translated into two specific applications: a microwave transparent window using patch arrays and selective high solar gain glazing using a mesh design.

Regarding the first application, several studies have been done on the topic of microwave transparent glazing but some questions remained open, one of them being:

"How much are centimetric waves attenuated by a window with a structured coating and how do these waves propagate inside a building?"

As presented in Chapter 2, a patch array with small cell periodicity and narrow engraving width are preferable for high transmission of microwaves in the range of 26 - 40 GHz while maintaining thermal insulation. It is shown that the thickness of the glass pane and the air

Chapter 7. Conclusion

gap distance play an important role in the position and bandwidth of the transmission peaks. A field test experiment done at the SolAce unit in NEST, Dübendorf showed a highly directional propagation of EM waves from mobile telecommunication inside buildings (see Chap. 3). This suggests that a large part of a glazing façade should be laser-treated to achieve optimal signal for mobile communication. Overall it is shown that novel laser-treated coating is especially advantageous in the building sector to improve the quality of wireless networks which will become increasingly important for the Internet of Things and $\geq 5G$ mobile technology.

Concerning the second application, the understanding of the interaction between an incoming beam of light and matter is crucial to predict how a structured coating will transmit the EM wave:

"How does the transmittance of a light depends on the dimensions of the structure?"

A full-wave simulation using FDTD is presented in Chapter 4. This method provides the E-field distributions of the EM waves by solving Maxwell's equations, giving the transmittance of an incident plane wave after passing through the structured coating. The model is first compared to results published in the literature and validated using samples produced by nano imprint lithography. Various parameters (linewidth, periodicity and thickness) are optimized to achieve high transmittance in the solar spectral range while reflecting infrared radiation in the MIR spectrum.

The resulting structured coating increases solar heat gains and thus helps reduce the space heating energy in buildings during cold months. However, the risk of glare and overheating increases considerably. For that reason, adaptive solar protection such as electrochromic windows is studied and leads to the last scientific question:

"How can electrochromic devices be improved to be used as adaptive solar protection?"

In Chapter 5, hierarchical metal meshes are introduced in place of ITO transparent conductive electrodes in electrochromic devices (ECDs). Metal meshes achieve low sheet resistance and large-band transmittance allowing for remarkable optical modulation in the full spectral range of solar radiation compared to conventional ITO-based devices. Moreover, the electronic structure of electrochromic material (tungsten trioxide) is investigated in Chapter 6. It is shown that the color neutrality and broadband modulation of the spectral transmission can be improved by doping WO_3 with Molybdenum. In-situ Photoelectron Spectroscopy measurements reveal that the coloration mechanism is related to the reduction of W^{6+} to W^{5+} and Mo^{6+} to Mo^{5+} . In the initial stages of lithiation, Mo is preferably reduced followed by the reduction of W which could provide a dual-band modulation of visible and near-infrared light. Both of these findings pave the way for next-generation EC devices with color neutral and broadband modulation of the solar spectrum and provide a high potential for energy savings

by controlling the solar heat gains in buildings.

7.1 Outlook

The work presented within this thesis proposed individual suggestions to improve the functionality of insulated glazing. Some questions remains open on the application side, e.g. where do we still need improvement, how to manufacture and what is the balance of cost and benefit. In the following, an design is provided on a multifunctional smart window that is particularly effective for seasonal modulation of the solar radiation in buildings.

As shown in Figure 7.1, this proposed glazing consists of a metal nanomesh similar to the one studied in Chapter 4. The transparent conductive layer acts as a conductor in the last hundreds of nanometers and, at the same time, as a selective coating to reflect the MIR. A larger micrometric metal mesh is added on top of the nanomesh to achieve high conductivity on large-scale devices while keeping a high visible transmittance. In that sense, the linewidth of the mesh should remain below $10\ \mu\text{m}$ to ensure that the structures are not visible to the bare eye. As explained in Chapter 5, an ultrathin metal layer is then added on top the hybrid meshes to improve the interface with the electrochromic layer and to protect the metal mesh from degradation. A enhanced electrochromic coating based on doping of tungsten trioxide (see Chapter 6) is evaporated above the hierarchical structure and acts as light modulator for adaptive solar protection. A solid ion conductor is placed above the EC layer and the same process is then repeated to produce the ion storage on top of the existing multilayer. Both, the EC layer and ion storage can easily be interchanged.

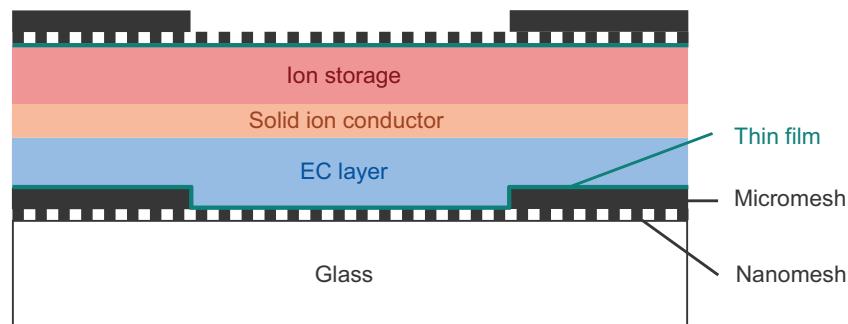


Figure 7.1: 2D cross-section combining multiple hierarchical structured layers for multifunctional electrochromic application.

The combination of these technologies results in an electrochromic window with a full solar spectral range, color neutrality, fast switching speed, and low emissivity in the MIR resulting in excellent thermal insulation. This multifunctional glazing thus represents an ideal candidate for the modulation of solar heat gain in varying climates.

Chapter 7. Conclusion

At the same time, it also rises several further research questions regarding large-scale manufacturing of nanometric structures. Nowadays, sample production in the nanoscale is mostly limited to the size of silicon wafers used in the clean room environment. Promising technologies such as gravure printing (micrometric scale) and nanoimprint lithography (nanometric scale) are closing the gap towards large-scale manufacturing and represents promising methods for producing the proposed design.

BIBLIOGRAPHY

- [1] Kemmler A 2022 Analyse des schweizerischen Energieverbrauchs 2000-2021 Tech. rep. Swiss Federal Office of Energy SFOE
- [2] Florio P, Tendon X, Fleury J, Costantini C, Schueler A and Scartezzini J L 2022 *Energies* **15** 793 ISSN 1996-1073
- [3] OlliPekka R 2013 *Ministry of Transport and Communications Working Group*
- [4] Asp A, Baniya A, Yunas S F, Niemelae J and Valkama M 2015 Applicability of Frequency Selective Surfaces to Enhance Mobile Network Coverage in Future Energy-Efficient Built Environments *Proceedings of European Wireless 2015; 21th European Wireless Conference* pp 1–8
- [5] Ängskog P, Bäckström M and Vallhagen B 2015 Measurement of radio signal propagation through window panes and energy saving windows *2015 IEEE International Symposium on Electromagnetic Compatibility (EMC)* pp 74–79
- [6] Rodriguez I, Nguyen H C, Jorgensen N T K, Sorensen T B and Mogensen P 2014 Radio Propagation into Modern Buildings: Attenuation Measurements in the Range from 800 MHz to 18 GHz *2014 IEEE 80th Vehicular Technology Conference (VTC2014-Fall)* pp 1–5
- [7] Hoppe R, Wolfle G and Landstorfer F M 1999 Measurement of building penetration loss and propagation models for radio transmission into buildings *Gateway to 21st Century Communications Village. VTC 1999-Fall. IEEE VTS 50th Vehicular Technology Conference (Cat. No.99CH36324)* vol 4 pp 2298–2302 vol.4
- [8] Bouvard O, Lanini M, Burnier L, Witte R, Cuttat B, Salvadè A and Schüler A 2017 *Energy Procedia* **122** 781–786 ISSN 1876-6102
- [9] Burnier L, Lanini M, Bouvard O, Scanferla D, Varathan A, Genoud C, Marguerit A, Cuttat B, Dury N, Witte R, Salvadè A and Schüler A 2017 *IET Microwaves, Antennas & Propagation* **11** 1449–1455 ISSN 1751-8733
- [10] Ade P A R, Pisano G, Tucker C and Weaver S 2006 A review of metal mesh filters *Milimeter and Submillimeter Detectors and Instrumentation for Astronomy III* vol 6275 (International Society for Optics and Photonics) p 62750U
- [11] Glass Configurator AGC Europe <https://www.agcourglass.com/configurator/en> Accessed on 2022–12–01
- [12] Faist A 1988 *EPFL Le projet LESO Synthèse des principaux résultats*
- [13] Costa F, Monorchio A and Manara G 2014 *Applied Computational Electromagnetics Society Journal* **29**

Bibliography

- [14] Ulrich R 1967 *Infrared Physics* **7** 37–55 ISSN 0020-0891
- [15] Meier M 2006 *Mikrostrukturierte Metallschichten Auf Glas* Ph.D. thesis Bayerischen Julius-Maximilians-Universität Würzburg
- [16] Chambers J, Hollmuller P, Bouvard O, Schueler A, Scartezzini J L, Azar E and Patel M K 2019 *Energy* **185** 136–147 ISSN 0360-5442
- [17] Daqiqeh Rezaei S, Shannigrahi S and Ramakrishna S 2017 *Solar Energy Materials and Solar Cells* **159** 26–51
- [18] Sibilio S, Rosato A, Scorpio M, Iuliano G, Ciampi G, Vanoli G P and de Rossi F 2016 *International Journal of Heat and Technology* **34** S481–S488 ISSN 03928764
- [19] Bouvard O, Lagier M, Burnier L, Krammer A and Schüler A 2021 *Thin Solid Films* **730** 138700 ISSN 0040-6090
- [20] Lokanc M, Eggert R and Redlinger M 2015 The Availability of Indium: The Present, Medium Term, and Long Term Tech. Rep. NREL/SR-6A20-62409, 1327212
- [21] Kumar A and Zhou C 2010 *ACS Nano* **4** 11–14 ISSN 1936-0851
- [22] Zhou K, Wang H, Zhang S, Jiu J, Liu J, Zhang Y and Yan H 2017 *Journal of Materials Science* **52** 12783–12794 ISSN 1573-4803
- [23] Synnefa A, Santamouris M and Apostolakis K 2007 *Solar Energy* **81** 488–497 ISSN 0038-092X
- [24] Touch Display Research Inc <https://touchdisplayresearch.com/?cat=41> Accessed on 2022-12-01
- [25] Fleury J, Lanini M, Pose C, Burnier L, Salvadè A, Zimmermann E, Genoud C and Schüler A 2020 *Applied Physics A: Materials Science & Processing* **126** 417 ISSN 0947-8396
- [26] Netze S 2019 Mobile radio frequencies for 5g awarded in switzerland Technical report Eidgenössische Kommunikationskommission ComCom
- [27] Hossain S 2013 *American Journal of Engineering Research* **02** 344–353
- [28] Kiani G I, Olsson L G, Karlsson A and Esselle K P 2010 *IET Microwaves, Antennas & Propagation* **4** 955–961 ISSN 1751-8733
- [29] Panwar N, Sharma S and Singh A K 2016 *Physical Communication* **18** 64–84 ISSN 1874-4907
- [30] Ullah I, Zhao X, Habibi D and Kiani G 2011 Transmission improvement of UMTS and Wi-Fi signals through energy saving glass using FSS *WAMICON 2011 Conference Proceedings* pp 1–5
- [31] Sohail S and Zarar M 2015 **10** 8902–8906
- [32] Rafique U, Ahmed M M, Haq M A and Rana M T 2011 Transmission of RF signals through energy efficient window using FSS *2011 7th International Conference on Emerging Technologies* pp 1–4
- [33] Widenberg B and Rodriguez J V 2002 *Design of Energy Saving Windows with High Transmission at 900 MHz and 1800 MHz (Technical Report LUTEDX/(TEAT-7110/1-14/(2002) vol TEAT-7110)* ([Publisher information missing])
- [34] Habib S, Butt M F U and Kiani G I 2015 Parametric analysis of a band-pass FSS for double glazed soft-coated energy saving glass *2015 International Symposium on Antennas and Propagation (ISAP)* pp 1–4

- [35] Kiani G I and Aldhaferi R W 2014 Wide band FSS for increased thermal and communication efficiency in smart buildings *2014 IEEE Antennas and Propagation Society International Symposium (APSURSI)* pp 2064–2065 ISSN 1947-1491
- [36] Bouvard O, Lanini M, Burnier L, Witte R, Cuttat B, Salvadè A and Schüler A 2016 *Applied Physics A* **123** 66 ISSN 1432-0630
- [37] Munk B A 2000 *Frequency Selective Surfaces: Theory and Design* | Wiley
- [38] Gustafsson M, Karlsson A, Rebelo A and Widenberg B 2006 *IEEE Transactions on Antennas and Propagation* **54** 1897–1900 ISSN 1558-2221
- [39] Sohail S I, Esselle K P and Kiani G 2012 Design of a bandpass FSS on dual layer energy saving glass for improved RF communication in modern buildings *Proceedings of the 2012 IEEE International Symposium on Antennas and Propagation* pp 1–2 ISSN 1947-1491
- [40] Costa F, Monorchio A and Manara G 2010 *IEEE Transactions on Antennas and Propagation* **58** 1551–1558 ISSN 1558-2221
- [41] Kiani G I, Karlsson A, Olsson L and Esselle K P 2007 Glass Characterization for Designing Frequency Selective Surfaces to Improve Transmission through Energy Saving Glass Windows *2007 Asia-Pacific Microwave Conference* pp 1–4 ISSN 2165-4743
- [42] Zaidi A A, Baldemair R, Tullberg H, Bjorkegren H, Sundstrom L, Medbo J, Kilinc C and Da Silva I 2016 *IEEE Communications Magazine* **54** 90–98 ISSN 1558-1896
- [43] Lerch M, Svoboda P, Trindade O, Resch J, Raida V and Rupp M 2019 Identifying Multipath Propagation in Vehicular Repeater Deployments by LTE Measurements *2019 IEEE 89th Vehicular Technology Conference (VTC2019-Spring)* pp 1–5 ISSN 2577-2465
- [44] Majed M B, Rahman T A and Aziz O A 2018 *International Journal of Electrical and Computer Engineering* **8** 2254–2260
- [45] Paschotta R 2008 *Encyclopedia of Laser Physics and Technology* 2nd ed (Weinheim: Wiley-VCH) ISBN 978-3-527-40828-3
- [46] Klar T, Perner M, Grosse S, von Plessen G, Spirkl W and Feldmann J 1998 *Physical Review Letters* **80** 4249–4252
- [47] Ahmadvand A, Sinha R, Gerislioglu B, Karabiyik M, Pala N and Shur M 2016 *Optics Letters* **41** 5333–5336 ISSN 1539-4794
- [48] Patenaude A 1991 *PROGRESSIVE ARCHITECTURE* **72** 41
- [49] Wu T K 2005 Frequency Selective Surfaces *Encyclopedia of RF and Microwave Engineering* (American Cancer Society) ISBN 978-0-471-65450-6
- [50] Fleury J, Burnier L, Delaporte H and Schüler A 2021 *Journal of Physics: Conference Series* **2042** 012181 ISSN 1742-6596
- [51] Palattella M R, Dohler M, Grieco A, Rizzo G, Torsner J, Engel T and Ladid L 2016 *IEEE Journal on Selected Areas in Communications* **34** 510–527 ISSN 0733-8716
- [52] Kim H and Nam S 2021 *IEEE Antennas and Wireless Propagation Letters* **20** 108–112 ISSN 1548-5757
- [53] Fleury J, Burnier L, Lanini M, Domenico M D, Zimmermann E, Genoud C, Salvadè A and Schueler A 2019 *Journal of Physics: Conference Series* **1343** 012199 ISSN 1742-6596
- [54] Richner P, Heer P, Largo R, Marchesi E and Zimmermann M 2017 *Informes de la con-*

Bibliography

- strucción* **69** 3 ISSN 0020-0883
- [55] RSRP and RSRQ - Teltonika Networks Wiki
- [56] Catrysse P B and Fan S 2010 *Nano Letters* **10** 2944–2949 ISSN 1530-6984
- [57] Shin S, Ganorkar S, Kim J, Kim Y H, Kim Y T and Kim S I 2015 *Journal of Nanoscience and Nanotechnology* **15** 7640–7644 ISSN 1533-4899
- [58] Stelling C, Singh C R, Karg M, König T A F, Thelakkat M and Retsch M 2017 *Scientific Reports* **7** 42530 ISSN 2045-2322
- [59] Ansys Lumerical FDTD <https://www.ansys.com/products/photonics/fdtd>
- [60] Polyanskiy M N Refractive index database <https://refractiveindex.info> Accessed on 2022-09-15
- [61] EN410: 2011 *Glass in building - Determination of luminous and solar characteristics of glazing*
- [62] Jelle B P 2013 *Solar Energy Materials and Solar Cells* **116** 291–323 ISSN 0927-0248
- [63] Mitteramskogler T, Haslinger M J, Shoshi A, Schrittwieser S, Schotter J, Brueckl H and Muehlberger M 2018 Fabrication of nanoparticles for biosensing using UV-NIL and lift-off *34th European Mask and Lithography Conference* vol 10775 (International Society for Optics and Photonics) p 107750Y
- [64] Tong Q 2016 *Direct Laser Writing of Polymeric and Metallic Nanostructures via Optically Induced Local Thermal Effect* Ph.D. thesis
- [65] Gong J, Dai R, Wang Z and Zhang Z 2015 *Scientific Reports* **5** 9279 ISSN 2045-2322
- [66] Valkonen E, Karlsson B and Ribbing C G 1984 *Solar Energy* **32** 211–222 ISSN 0038-092X
- [67] McAlister A J and Stern E A 1963 *Physical Review* **132** 1599–1602
- [68] Wu C, Song G, Liu H, Cui L, Yu L and Xiao J 2013 *Journal of Modern Optics* **60** 190–196 ISSN 0950-0340
- [69] Kemmler A 2018 Analyse des schweizerischen Energieverbrauchs 2000-2017 Tech. rep. Swiss Federal Office of Energy SFOE
- [70] Rezaei S D, Shannigrahi S and Ramakrishna S 2017 *Solar Energy Materials and Solar Cells* **159** 26–51 ISSN 0927-0248
- [71] Granqvist C G, Lansåker P C, Mlyuka N R, Niklasson G A and Avendaño E 2009 *Solar Energy Materials and Solar Cells* **93** 2032–2039 ISSN 0927-0248
- [72] Granqvist C G 2014 *Thin Solid Films* **564** 1–38 ISSN 0040-6090
- [73] Cui B B, Zhong Y W and Yao J 2015 *Journal of the American Chemical Society* **137** 4058–4061 ISSN 0002-7863
- [74] Davy N C, Sezen-Edmonds M, Gao J, Lin X, Liu A, Yao N, Kahn A and Loo Y L 2017 *Nature Energy* **2** 1–11 ISSN 2058-7546
- [75] Niu J, Wang Y, Zou X, Tan Y, Jia C, Weng X and Deng L 2021 *Applied Materials Today* **24** 101073 ISSN 2352-9407
- [76] García-Cañadas J, Meacham A P, Peter L M and Ward M D 2003 *Angewandte Chemie International Edition* **42** 3011–3014 ISSN 1521-3773
- [77] Dyer A L, Grenier C R G and Reynolds J R 2007 *Advanced Functional Materials* **17** 1480–1486 ISSN 1616-3028
- [78] Wang Y, Runnerstrom E L and Milliron D J 2016 *Annual Review of Chemical and*

- Biomolecular Engineering* **7** 283–304 ISSN 1947-5446
- [79] Williams T E, Chang C M, Rosen E L, Garcia G, Runnerstrom E L, Williams B L, Koo B, Buonsanti R, Milliron D J and Helms B A 2014 *Journal of Materials Chemistry C* **2** 3328–3335 ISSN 2050-7534
- [80] Llordés A, Wang Y, Fernandez-Martinez A, Xiao P, Lee T, Poulain A, Zandi O, Saez Cabezas C A, Henkelman G and Milliron D J 2016 *Nature Materials* **15** 1267–1273 ISSN 1476-4660
- [81] Llordés A, Garcia G, Gazquez J and Milliron D J 2013 *Nature* **500** 323–326 ISSN 1476-4687
- [82] Yu L, Shearer C and Shapter J 2016 *Chemical Reviews* **116** 13413–13453 ISSN 0009-2665
- [83] Haacke G 1976 *Journal of Applied Physics* **47** 4086–4089 ISSN 0021-8979
- [84] Gao T, Huang P S, Lee J K and Leu P W 2015 *RSC Advances* **5** 70713–70717 ISSN 2046-2069
- [85] Chung S i, Kim P K, Ha T g and Han J T 2019 *Nanotechnology* **30** 125301 ISSN 0957-4484
- [86] Kim W K, Lee S, Hee Lee D, Hee Park I, Seong Bae J, Woo Lee T, Kim J Y, Hun Park J, Chan Cho Y, Ryong Cho C and Jeong S Y 2015 *Scientific Reports* **5** 10715 ISSN 2045-2322
- [87] Choi H J, Choo S, Jung P H, Shin J H, Kim Y D and Lee H 2015 *Nanotechnology* **26** 055305 ISSN 0957-4484
- [88] Präzisions Glas Optik <https://www.pgo-online.com/> Accessed on 2022–11–12
- [89] Lee J, Lee Y, Ahn J, Kim J, Yoon S, Kim Y S and Cho KY 2017 *Journal of Materials Chemistry C* **5** 12800–12806 ISSN 2050-7534
- [90] Paeng D, Yoo J H, Yeo J, Lee D, Kim E, Ko S H and Grigoropoulos C P 2015 *Advanced Materials* **27** 2762–2767 ISSN 1521-4095
- [91] Kwon N, Kim K, Sung S, Yi I and Chung I 2013 *Nanotechnology* **24** 235205 ISSN 0957-4484
- [92] Ho Y H, Chen K Y, Liu S W, Chang Y T, Huang D W and Wei P K 2011 *Organic Electronics* **12** 961–965 ISSN 1566-1199
- [93] Kang M G, Joon Park H, Hyun Ahn S and Jay Guo L 2010 *Solar Energy Materials and Solar Cells* **94** 1179–1184 ISSN 0927-0248
- [94] Jung P H, Doo Kim Y, Choi H J, Hoon Sung Y and Lee H 2016 *RSC Advances* **6** 92970–92974
- [95] Jang H Y, Lee S K, Cho S H, Ahn J H and Park S 2013 *Chemistry of Materials* **25** 3535–3538 ISSN 0897-4756
- [96] Manwani K and Panda E 2021 *Materials Science in Semiconductor Processing* **134** 106048 ISSN 1369-8001
- [97] Ghorbani M M and Taherian R 2019 12 - Methods of Measuring Electrical Properties of Material**Hereby from Keithley Co. and Dr. Michael B. Heaney is appreciated due to valuable content used in this chapter. *Electrical Conductivity in Polymer-Based Composites* Plastics Design Library ed Taherian R and Kausar A (William Andrew Publishing) pp 365–394 ISBN 978-0-12-812541-0
- [98] Lagier M, Bertinotti A, Bouvard O, Burnier L and Schüler A 2021 *Optical Materials* **117** 111091 ISSN 0925-3467
- [99] Markel V A 2016 *JOSA A* **33** 1244–1256 ISSN 1520-8532
- [100] Millán C, Santonja C, Domingo M, Luna R and Satorre M Á 2019 *Astronomy & Astrophysics* **628** A63 ISSN 0004-6361, 1432-0746
- [101] Sawada S and Danielson G C 1959 *Physical Review* **113** 1008–1013
- [102] Schüler A, Ellenberger C, Oelhafen P, Haug C and Brenn R 2000 *Journal of Applied Physics*

Bibliography

- 87** 4285–4292 ISSN 0021-8979
- [103] Granqvist C G 1995 *Handbook of Inorganic Electrochromic Materials* (Elsevier) ISBN 978-0-08-053290-5
- [104] Mansour D, Bouvard O and Schüler A 2017 *Energy Procedia* **122** 787–792 ISSN 1876-6102
- [105] Chowdhury D R, Spiccia L, Amritphale S S, Paul A and Singh A 2016 *Journal of Materials Chemistry A* **4** 3655–3660 ISSN 2050-7496
- [106] Kratochvil B, Lorah E and Garber C 1969 *Analytical Chemistry* **41** 1793–1796 ISSN 0003-2700
- [107] Meites L 1963 *Handbook of Analytical Chemistry*. (New York: McGraw-Hill) ISBN 978-0-07-041336-8
- [108] Reichman B and Bard A J 1979 *Journal of The Electrochemical Society* **126** 583 ISSN 1945-7111
- [109] Bouvard O, Burnier L, Oelhafen P, Tonin A, Wüst P, Sidler F, Zweifel G and Schüler A 2018 *Energy Efficiency* **11** 1397–1410 ISSN 1570-6478
- [110] Steiner R, Oelhafen P, Reber G and Romanyuk A 2005
- [111] Swanepoel R 1983 *Journal of Physics E: Scientific Instruments* **16** 1214–1222 ISSN 0022-3735
- [112] Rubin M 1985 *Solar Energy Materials* **12** 275–288 ISSN 0165-1633
- [113] Antonets I V, Kotov L N, Nekipelov S V and Golubev Y A 2004 *Technical Physics* **49** 306–309 ISSN 1090-6525
- [114] Karoui A 2011 *ECS Transactions* **41** 21 ISSN 1938-5862
- [115] Hoffmann H and Fischer G 1976 *Thin Solid Films* **36** 25–28 ISSN 0040-6090
- [116] Hautcoeur J, Castel X, Colombel F, Benzerga R, Himdi M, Legeay G and Motta-Cruz E 2011 *Thin Solid Films* **519** 3851–3858 ISSN 0040-6090
- [117] Wooten F 1973 *American Journal of Physics* **41** 939–940 ISSN 0002-9505
- [118] Hu L, Kim H S, Lee J Y, Peumans P and Cui Y 2010 *ACS Nano* **4** 2955–2963 ISSN 1936-0851
- [119] Hitosugi T, Yamada N, Nakao S, Hirose Y and Hasegawa T 2010 *physica status solidi (a)* **207** 1529–1537 ISSN 1862-6319
- [120] ASTM D1003 2021 *Standard Test Method for Haze and Luminous Transmittance of Transparent Plastics*
- [121] Wang S J, Wang M C, Chen S F, Li Y H, Shen T S, Bor H Y and Wei C N 2018 *Sensors (Basel, Switzerland)* **18** 2803 ISSN 1424-8220
- [122] Chen H, Chiasera A, Armellini C, Speranza G, Varas S, Sayginer O, Alfano A, Cassinelli M, Caironi M, Suriano R, Zaghloul M, Tagliaferri A, Ferrari M and Pietralunga S M 2021 *EPJ Web of Conferences* **255** 05003 ISSN 2100-014X
- [123] Gil-Rostra J, Cano M, Pedrosa J M, Ferrer F J, García-García F, Yubero F and González-Elipe A R 2012 *ACS Applied Materials & Interfaces* **4** 628–638 ISSN 1944-8244
- [124] Camirand H, Baloukas B, Klemberg-Sapieha J E and Martinu L 2015 *Solar Energy Materials and Solar Cells* **140** 77–85 ISSN 0927-0248
- [125] Usha K S, Sivakumar R and Sanjeeviraja C 2013 *Journal of Applied Physics* **114** 123501 ISSN 0021-8979
- [126] Fleury J, Burnier L and Schüler A 2022 *Journal of Applied Physics* **131** 015301 ISSN

- 0021-8979
- [127] Granqvist C G 2013 *Electrochromic Metal Oxides: An Introduction to Materials and Devices* *Electrochromic Materials and Devices* (John Wiley & Sons, Ltd) chap 1, pp 1–40 ISBN 978-3-527-67985-0
- [128] Seman M and Wolden C A 2003 *Journal of Vacuum Science & Technology A* **21** 1927–1933 ISSN 0734-2101
- [129] Lu H, Wang R, Bao F, Ye J, Lin H, Zhu H, Wan M, Yang H, Shen K and Mai Y 2022 *Optical Materials* **133** 112848 ISSN 0925-3467
- [130] Bessière A, Badot J C, Certiat M C, Livage J, Lucas V and Baffier N 2001 *Electrochimica Acta* **46** 2251–2256 ISSN 0013-4686
- [131] Chokshi K, Qutubuddin S and Hussam A 1989 *Journal of Colloid and Interface Science* **129** 315–326 ISSN 0021-9797
- [132] Li G, Zhang S, Guo C and Liu S 2016 *Nanoscale* **8** 9861–9868 ISSN 2040-3372
- [133] Chen P W, Chang C T, Ko T F, Hsu S C, Li K D and Wu J Y 2020 *Scientific Reports* **10** 8430 ISSN 2045-2322
- [134] Liang L, Zhang J, Zhou Y, Xie J, Zhang X, Guan M, Pan B and Xie Y 2013 *Scientific Reports* **3** 1936 ISSN 2045-2322
- [135] Dalavi D S, Devan R S, Patil R A, Patil R S, Ma Y R, Sadale S B, Kim I, Kim J H and Patil P S 2013 *Journal of Materials Chemistry C* **1** 3722–3728 ISSN 2050-7534
- [136] Lee S H, Cheong H M, Tracy C E, Mascarenhas A, Czanderna A W and Deb S K 1999 *Applied Physics Letters* **75** 1541–1543 ISSN 0003-6951
- [137] More A J, Patil R S, Dalavi D S, Mali S S, Hong C K, Gang M G, Kim J H and Patil P S 2014 *Materials Letters* **134** 298–301 ISSN 0167-577X
- [138] Ng C Y, Abdul Razak K and Lockman Z 2015 *Electrochimica Acta* **178** 673–681 ISSN 0013-4686
- [139] El-Nahass M M, Saadeldin M M, Ali H A M and Zaghllol M 2015 *Materials Science in Semiconductor Processing* **29** 201–205 ISSN 1369-8001
- [140] Yin Y, Lan C, Guo H and Li C 2016 *ACS Applied Materials & Interfaces* **8** 3861–3867 ISSN 1944-8244
- [141] Meenakshi M, Sivakumar R, Perumal P and Sanjeeviraja C 2016 *Materials Today: Proceedings* **3** S30–S39 ISSN 2214-7853
- [142] Pauporté T 2002 *Journal of The Electrochemical Society* **149** C539 ISSN 1945-7111
- [143] Wen R T, Granqvist C G and Niklasson G A 2015 *Nature Materials* **14** 996–1001 ISSN 1476-4660
- [144] Bouvard O V C 2019 *Coatings with tailored electronic and optical properties for advanced glazing* Ph.D. thesis EPFL
- [145] Passerini S and Scrosati B 1992 *Solid State Ionics* **53–56** 520–524 ISSN 0167-2738
- [146] Wang F, Jia J, Zhao W, Zhang L, Ma H, Li N and Chen Y 2022 *Materials Science in Semiconductor Processing* **151** 106986 ISSN 1369-8001
- [147] Purushothaman K K and Muralidharan G 2009 *Functional Materials Letters* **02** 143–145 ISSN 1793-6047
- [148] Xia X H, Tu J P, Zhang J, Wang X L, Zhang W K and Huang H 2008 *Nanotechnology* **19**

Bibliography

- 465701 ISSN 0957-4484
- [149] Benck J D, Pinaud B A, Gorlin Y and Jaramillo T F 2014 *PLOS ONE* **9** e107942 ISSN 1932-6203
- [150] Darmawi S, Burkhardt S, Leichtweiss T, A Weber D, Wenzel S, Janek J, T Elm M and J Klar P 2015 *Physical Chemistry Chemical Physics* **17** 15903–15911
- [151] Arvizu M A, Wen R T, Primetzhofer D, Klemberg-Sapieha J E, Martinu L, Niklasson G A and Granqvist C G 2015 *ACS Applied Materials & Interfaces* **7** 26387–26390 ISSN 1944-8244
- [152] Dong D, Robichaud J and Djaoued Y 2021 *Canadian Journal of Chemistry* **99** 549–556 ISSN 0008-4042
- [153] Granqvist C G, Arvizu M A, Bayrak Pehlivan İ, Qu H Y, Wen R T and Niklasson G A 2018 *Electrochimica Acta* **259** 1170–1182 ISSN 0013-4686
- [154] Arvizu M A, Niklasson G A and Granqvist C G 2017 *Chemistry of Materials* **29** 2246–2253 ISSN 0897-4756
- [155] Gaillard N, Cole B, Kaneshiro J, Miller E L, Marsen B, Weinhardt L, Bär M, Heske C, Ahn-Soon K, Yan Y and Al-Jassim M M 2010 *Journal of Materials Research* **25** 45–51 ISSN 2044-5326
- [156] Madhavi V, Kondaiah P, Hussain O M and Uthanna S 2013 *Conference Papers in Energy* **2013** e104047 ISSN 2356-6108
- [157] Cui Y, Wang Q and Gao Y 2020 *Materials Today Communications* **25** 101611 ISSN 2352-4928
- [158] Arvizu M A, Granqvist C G and Niklasson G A 2016 *Journal of Physics: Conference Series* **682** 012005 ISSN 1742-6596
- [159] Pennisi A, Simone F and Lampert C M 1992 *Solar Energy Materials and Solar Cells* **28** 233–247 ISSN 0927-0248
- [160] Faughnan B W and Crandall R S 1977 *Applied Physics Letters* **31** 834–836 ISSN 0003-6951
- [161] Dubey P, Lopez G A, Martinez G and Ramana C V 2016 *Journal of Applied Physics* **120** 245103 ISSN 0021-8979
- [162] Li N, Teng H, Zhang L, Zhou J and Liu M 2015 *RSC Advances* **5** 95394–95400 ISSN 2046-2069
- [163] Rahimnejad S, He J, Pan F, Lee X, Chen W, Wu K and Xu G 2014 *Materials Research Express* **1** 045044
- [164] Arntz F O, Goldner R B, Morel B, Hass T E and Wong K K 1990 *Journal of Applied Physics* **67** 3177–3179 ISSN 0021-8979
- [165] Vargas M, Rubio E J, Gutierrez A and Ramana C V 2014 *Journal of Applied Physics* **115** 133511 ISSN 0021-8979
- [166] Lin Y S, Tsai T H, Hung S C and Tien S W 2013 *Journal of Solid State Electrochemistry* **17** 1077–1088 ISSN 1433-0768
- [167] Getters S 1983
- [168] Towe M 2003 *Photoelectron Spectroscopy Studies of Carbon Based Fusion Reactor Materials* Ph.D. thesis University of Basel
- [169] Schüler A, Thommen V, Reimann P, Oelhafen P, Francz G, Zehnder T, Düggelin M, Mathys

- D and Guggenheim R 2001 *Journal of Vacuum Science & Technology A* **19** 922–929 ISSN 0734-2101
- [170] Schüler A, Videnovic I R, Oelhafen P and Brunold S 2001 *Solar Energy Materials and Solar Cells* **69** 271–284 ISSN 0927-0248
- [171] He Y, Wu Z, Fu L, Li C, Miao Y, Cao L, Fan H and Zou B 2003 *Chemistry of Materials* **15** 4039–4045 ISSN 0897-4756
- [172] Dixon R A, Williams J J, Morris D, Rebane J, Jones F H, Egdell R G and Downes S W 1998 *Surface Science* **399** 199–211 ISSN 0039-6028
- [173] Xie F Y, Gong L, Liu X, Tao Y T, Zhang W H, Chen S H, Meng H and Chen J 2012 *Journal of Electron Spectroscopy and Related Phenomena* **185** 112–118 ISSN 0368-2048
- [174] Wang B, Man W, Yu H, Li Y and Zheng F 2018 *Materials* **11** 1627 ISSN 1996-1944
- [175] Bouvard O, Krammer A and Schüler A 2016 *Surface and Interface Analysis* **48** 660–663 ISSN 1096-9918
- [176] Kerkhof F P J M, Moulijn J A and Heeres A 1978 *Journal of Electron Spectroscopy and Related Phenomena* **14** 453–466 ISSN 0368-2048
- [177] Colton R J, Guzman A M and Rabalais J W 1978 *Journal of Applied Physics* **49** 409–416 ISSN 0021-8979
- [178] Colton R J and Rabalais J W 1976 *Inorganic Chemistry* **15** 236–238 ISSN 0020-1669
- [179] Biloen P and Pott G T 1973 *Journal of Catalysis* **30** 169–174 ISSN 0021-9517
- [180] Alov N V 2015 *physica status solidi c* **12** 263–266 ISSN 1610-1642
- [181] Sarma D D and Rao C N R 1980 *Journal of Electron Spectroscopy and Related Phenomena* **20** 25–45 ISSN 0368-2048
- [182] Kim K S, Baitinger W E, Amy J W and Winograd N 1974 *Journal of Electron Spectroscopy and Related Phenomena* **5** 351–367 ISSN 0368-2048
- [183] Cimino A and De Angelis B A 1975 *Journal of Catalysis* **36** 11–22 ISSN 0021-9517
- [184] Vasilopoulou M, Soultati A, Georgiadou D G, Stergiopoulos T, Palilis L C, Kennou S, Stathopoulos N A, Davazoglou D and Argitis P 2014 *Journal of Materials Chemistry A* **2** 1738–1749 ISSN 2050-7496
- [185] Vasilopoulou M, Douvas A M, Georgiadou D G, Palilis L C, Kennou S, Sygellou L, Soultati A, Kostis I, Papadimitropoulos G, Davazoglou D and Argitis P 2012 *Journal of the American Chemical Society* **134** 16178–16187 ISSN 0002-7863
- [186] Wagner C D, Davis L E, Zeller M V, Taylor J A, Raymond R H and Gale L H 1981 *Surface and Interface Analysis* **3** 211–225 ISSN 1096-9918
- [187] Fleisch T H and Mains G J 1982 *The Journal of Chemical Physics* **76** 780–786 ISSN 0021-9606
- [188] Greiner M T and Lu Z H 2013 *NPG Asia Materials* **5** e55–e55 ISSN 1884-4057
- [189] Wang W, Janotti A and de Walle C G V 2016 *Journal of Materials Chemistry C* **4** 6641–6648 ISSN 2050-7534
- [190] Niklasson G A, Berggren L and Larsson A L 2004 *Solar Energy Materials and Solar Cells* **84** 315–328 ISSN 0927-0248
- [191] Bechinger C, Oefinger G, Herminghaus S and Leiderer P 1993 *Journal of Applied Physics* **74** 4527–4533 ISSN 0021-8979

Bibliography

- [192] Ho S F, Contarini S and Rabalais J W 1987 *The Journal of Physical Chemistry* **91** 4779–4788 ISSN 0022-3654
- [193] Du Y, Zhang K H L, Varga T and Chambers S A 2014 *Applied Physics Letters* **105** 051606 ISSN 0003-6951
- [194] Zhu J, Vasilopoulou M, Davazoglou D, Kennou S, Chroneos A and Schwingenschlögl U 2017 *Scientific Reports* **7** 40882 ISSN 2045-2322
- [195] Johansson M B, Zietz B, Niklasson G A and Österlund L 2014 *Journal of Applied Physics* **115** 213510 ISSN 0021-8979
- [196] Hashimoto S and Matsuoka H 1991 *Journal of The Electrochemical Society* **138** 2403 ISSN 1945-7111
- [197] Greiner M T, Chai L, Helander M G, Tang W M and Lu Z H 2012 *Advanced Functional Materials* **22** 4557–4568 ISSN 1616-3028
- [198] Ping Y, Rocca D and Galli G 2013 *Physical Review B* **87** 165203
- [199] Diaz-Reyes J, Castillo-Ojeda R, Galván-Arellano M and Zaca-Moran O 2013 *Advances in Condensed Matter Physics* **2013**
- [200] Lethy K J, Beena D, Mahadevan Pillai V P and Ganesan V 2008 *Journal of Applied Physics* **104** 033515 ISSN 0021-8979
- [201] Granqvist C G 2000 *Solar Energy Materials and Solar Cells* **60** 201–262 ISSN 0927-0248
- [202] Zhou L, Zhu J, Yu M, Huang X, Li Z, Wang Y and Yu C 2010 *The Journal of Physical Chemistry C* **114** 20947–20954 ISSN 1932-7447
- [203] Mehmood F, Pachter R, Murphy N R, Johnson W E and Ramana C V 2016 *Journal of Applied Physics* **120** 233105 ISSN 0021-8979
- [204] de Wijs G A and de Groot R A 1999 *Physical Review B* **60** 16463–16474
- [205] Triana C A, Araujo C M, Ahuja R, Niklasson G A and Edvinsson T 2017 *Scientific Reports* **7** 2044 ISSN 2045-2322
- [206] Matskevich N I, Shlegel V N, Semerikova A N and Matskevich M Y 2020 *Journal of Chemical & Engineering Data* **65** 1523–1530 ISSN 0021-9568
- [207] Kalanur S S 2019 *Catalysts* **9** 456
- [208] Kostis I, Vourdas N, Papadimitropoulos G, Douvas A, Vasilopoulou M, Boukos N and Davazoglou D 2013 *The Journal of Physical Chemistry C* **117** 18013–18020 ISSN 1932-7447
- [209] Vasilopoulou M, Kostis I, Vourdas N, Papadimitropoulos G, Douvas A, Boukos N, Kennou S and Davazoglou D 2014 *The Journal of Physical Chemistry C* **118** 12632–12641 ISSN 1932-7447

Jeremy FLEURY

PhD Student

+41 79 934 80 86

@ jeremy.fleury@epfl.ch

linkedin.com/in/jeremyfleury

Morges, Switzerland



EXPERIENCE

Project Engineer

École Polytechnique Fédérale Lausanne

05/2017 - 10/2018 Lausanne, Switzerland

Research group "Nanotechnology for Solar Energy Conversion" at the Solar Energy and Building Physics Laboratory (LESO-PB)

- Reduction of the heat energy needs of trains by an improved vehicle envelope

Scientific Assistant

University of Toronto

09/2016 - 05/2017 Toronto, Canada

Department of Materials Science & Engineering
Advanced Photovoltaics and Devices (APD) Research Group

- "Optimisation study of the nanosecond Laser-Induced Forward-Transfer (LIFT) process with thin aluminum films in air and in argon"

Civil Service

Hospital of Bruderholz

07/2011 - 08/2012 Basel, Switzerland

Engineering Department

EDUCATION

PhD Student

École Polytechnique Fédérale de Lausanne (EPFL)

10/2018 - 02/2023 Lausanne, Switzerland

Research group "Nanotechnology for Solar Energy Conversion" at the Solar Energy and Building Physics Laboratory (LESO-PB)

- Transparent structured conductive coating for applications in smart windows

M.Sc. Nanosciences, Major Physics

University of Basel

09/2015 - 05/2017

B.Sc. Nanosciences

University of Basel

09/2012 - 08/2015

Baccalaureate Mathematics and Physics

High School, Liestal and Porrentruy

09/2012 - 08/2015

- One year Liestal (German) & 2 years in Porrentruy (Bilingual FR/GER)

LANGUAGES

French



Swiss German



English



Spanish



PASSIONS



Ski touring, climbing & alpinism

are activities that allow me to fulfil my love for nature and for the mountains



Physical & Mental Health

are my priorities. Always working out, eating good food and taking care of my well-being



Sustainability

and renewable energy drive me forward to working on a future free of fossil fuels

SKILLS

Software

Latex

MS-Office

OriginLab

G-Code

Illustrator

AutoDesk Inventor

Lab Equipment

ns LASER

CNC

SEM

AFM

EDAX

Vacuum Coating

XPS/UPS

Sputtering

PUBLICATIONS

Publications include peer-reviewed articles in scientific journals and international conference proceedings, patents and co-supervised student work.

Journal papers

Fleury, J., Lanini, M., Pose, C., Burnier, L., Salvadè, A., Zimmermann, E., ... & Schüler, A. (2020). Wide band-pass FSS with reduced periodicity for energy efficient windows at higher frequencies. *Applied Physics A*, 126(6), 1-11.

Fleury, J., Burnier, L., & Schüler, A. (2022). Electronic properties and ion migration of "in vacuo" lithiated nanoporous WO₃: Mo thin films. *Journal of Applied Physics*, 131(1), 015301.

Chatelain, T., Mauree, D., Taylor, S., Bouvard, O., **Fleury, J.**, Burnier, L., & Schüler, A. (2019). Solar cooking potential in Switzerland: Nodal modelling and optimization. *Solar Energy*, 194, 788-803.

Florio, P., Tendon, X., **Fleury, J.**, Costantini, C., Schueler, A., & Scartezzini, J. L. (2022). Performance Assessment of a nZEB Carbon Neutral Living/Office Space and Its Integration into a District Energy-Hub. *Energies*, 15(3), 793.

Marot, L., **Fleury, J.**, Haas, D., Iyyakkunnel, S., Sanchez, F., Steiner, R., ... & Meyer, E. (2022). In situ work function measurements of W, WO₃ nanostructured surfaces. *Surface and Coatings Technology*, 447, 128870.

Conference proceedings and abstracts

Fleury, J., Burnier, L., Lanini, M., Di Domenico, M., Zimmermann, E., Genoud, C., ... & Schueler, A. (2019, November). Novel microwave transparent low emissivity coating for energy-efficient glazing: towards 5G frequencies. In *Journal of Physics: Conference Series* (Vol. 1343, No. 1, p. 012199). IOP Publishing.

Fleury, J., Burnier, L., Delaporte, H., & Schüler, A. (2021, November). Combining thermal insulation and mobile communication in buildings: influence of laser-treated glazing on microwave propagation. In *Journal of Physics: Conference Series* (Vol. 2042, No. 1, p. 012181). IOP Publishing.

Manuscripts submitted

Fleury, J., Burnier, L., Lagier M., Shukla S., Manwani K., Panda E. and Schüler, A., 2022. Electrochromic device with hierarchical metal mesh electrodes: transmittance switching in the full spectral range of solar radiation, Submitted to *Solar Energy Materials and Solar Cells*.

Burnier, L., Jamaly N., **Fleury, J.**, Delaporte, H., Durussel S. and Schüler, A., 2022. Energy saving glazing with high MIMO performance, Submitted to *IEEE Transactions on Vehicular Technology*.

Schindelholz R., Notzon D., Kwarikunda N., Chachiga J. Julia O., Ongaro C., Burnier L., **Fleury J.**, Manwani K. and Schüler A., 2022. Design and thermal simulation of solar box cookers for humanitarian aid in Uganda, Submitted to *Solar Energy*.

Patent

Schueler, A., Burnier, L., **Fleury, J.**, & Jamaly, N. (2021). Glazing unit (CH20200000249 (A2)).

Co-supervised Projects

Dolecek, Jelena (2019). 'Enhancing conductivity and light transmittance of Cu thin-layer on dielectric substrate by laser micro patterning'. Semester project, Solar Energy and Building Physics Laboratory, EPFL, Supervisors: Schüler A. and **Fleury J.**

Ongaro, Chiara and Julia, Olivia (2022). 'Solar cookers for the case of Uganda'. Semester project, Solar Energy and Building Physics Laboratory, EPFL, Supervisors: Schüler A. and **Fleury J.**

Schindelholz, Romain (2022). 'Développement d'un four solaire pour l'atténuation de la crise du bois de feu en Ouganda'. Master project, Solar Energy and Building Physics Laboratory, EPFL, Supervisors: Schüler A. and **Fleury J.**

Life's a bit like mountaineering – never look down.
— Edmund Hillary